UNIVERSIDADE DE LISBOA
FACULDADE DE CIÊNCIAS
DEPARTAMENTO DE FÍSICA

Parametric Imaging of FET PET using Nonlinear based Fitting

Inês Isabel Monteiro Costa

Mestrado Integrado em Engenharia Biomédica e Biofísica
Perfil de Sinais e Imagens Médicas

Dissertação orientada por:
Professor Dr. Pedro Miguel Dinis de Almeida
Dr. Christoph Lerche

2016

Acknowledgments

First I acknowledge my external supervisor Dr. Christoph Lerche of the INM-4 at Forschungzentrum Jülich for his teachings and guidance − and unlimited patience for all my questions, and fitting procedure struggles. I also acknowledge my internal supervisor, Dr. Pedro Almeida of the Faculdade de Ciências da Universidade de Lisboa for his supervision, and for helping me getting the opportunity to develop this work.

I would like to thank Dr. Liliana Caldeira of the INM-4 at Forschungzentrum Jülich for welcoming me there for the first time three years ago (when it all started!), and once again this time. Her help was of upmost importance on both occasions, on both academic and personal levels.

I would like to show my gratitude to all the members of the PET Group of INM-4 at Forschungzentrum Jülich. I was incredibly lucky to be working with such a great group of people, and with whom I learned so much. They were the most supportive working group I could have asked for, and kind enough to forgive me every time I swapped having lunch with them for a run around the center.

I would like to thank the extraordinary group of people I met while living in Aachen. They were many, from all around the world, and all of them contributed to make this past year an unforgettable experience. However, special thanks goes to Klim, Ilya, Deep, and Felix, who were the coolest flatmates ever, Borjana, and Yannick. I owe you all a lifetime supply of pastéis de nata.

Finally, I must express my very profound gratitude to my family. They were the ones who always believed. No matter where I am, I will always carry them in my heart; no matter who I become, I know they will always support me. This accomplishment would not have been possible without them. Thank you.

Summary

The importance of radiolabeled amino acids in Positron Emission Tomography (PET) imaging of the brain has been demonstrated by several studies. The most well studied amino acid tracer is ^{11}C-metionine, but because of the short half-life of ^{11}C, ^{18}F-labeled amino acid analogues have been developed for tumour imaging. A number of studies have proven the importance of O-(2-^{18}F-Fluoroethyl)-L-tyrosine (FET) in determining the extent of cerebral gliomas, biopsy guidance, treatment planning, and detecting recurrence of brain tumours. It was also demonstrated that dynamic changes of FET accumulation in gliomas are variable. High-grade gliomas (HGG) are characterized by an early peak, followed by decrease of FET uptake, whereas the uptake in low-grade gliomas (LGG) steadily increases.

Eleven patients (3 female, 8 male, age: 45 ± 15 years) with untreated primary brain tumours and histopathologic confirmation were studied. Six patients had HGG, while the remaining 5 were diagnosed with LGG. PET acquisition was done with the PET Insert of a hybrid Siemens 3T MR-BrainPET system. For tumour volume fitting, a segmentation procedure was applied. After segmentation, the mean time-activity curve (TAC) of the segmented tumour volumes (STVs) was calculated. Linear and nonlinear regression were used to fit to the TAC of each volume. When performing the fits with the linear model, the first 5 minutes of acquisition were discarded. For the nonlinear regression, the fits were applied to the mean TAC from 2 to 60 minutes after injection. Parametric images were calculated based on nonlinear regression fitting of FET data in each voxel. Three different nonlinear models were tested: an exponentially damped linear model, an exponentially damped linear model with an offset, and an exponentially damped linear model with square-root time dependence. The considered nonlinear model parameters were amplitude, A, and κ. The parametric images of manually selected tridimensional volumes containing the tumour were generated. Linear regression based parametric images were also computed for comparison, and the assessed parameters were intercept and slope. Whole-head parametric images were calculated based on nonlinear regression fitting using the exponentially damped linear model with square-root time dependence.

Nonlinear regression models were more accurate at reproducing FET TAC characteristics. The most robust models are the exponentially damped linear models without offset. For mean TAC fitting, a model with square-root time dependence reproduced FET activity curves more accurately, with coefficient of determination (R^2) values between 0.94 and 1.00. The A parameter from the exponentially damped linear model with square-root time dependence was the only one significantly different between HGG and LGG (p-value= 0.04, α=0.05). When generating parametric images based on voxel-wise fit, the nonlinear regression models with 2 parameters performed the best, with R^2 close to 1. Visual distinction between tumour grades was possible by comparing the amplitude images with the images of the summed activity across time. In the amplitude, LGGs take values similar to the ones of the surrounding background, thus disappearing from the image. On the other hand, HGGs amplitude images reproduce tumour uptake. Linear regression model fits returned R^2 values that were close to zero in both mean TAC fitting, and parametric image calculation. Grade distinction was possible based on the slope parameter alone, with LGGs showing higher slope values than the neighbouring tissue, and HGGs showing lower slope values than their surroundings. In general, though nonlinear models reproduce FET time activity curves more accurately, the distinction between low-grade and high-grade tumours based on one parameter only is better achieved by using linear regression model fitting. However, a reliable differentiation seems to be possible with joint analysis of A and κ parametric images.

Keywords: *PET; FET; modelling; nonlinear; voxel-based.*

Resumo

A importância do uso de aminoácidos marcados com isótopos radioativos em estudos de Tomografia de Emissão de Positrões (PET) tem sido amplamente demonstrada. Dentro deste grupo de traçadores, a metionina marcada com ^{11}C tem sido o mais estudado. No entanto, a curta semi-vida do radioisótopo ^{11}C tem levado ao desenvolvimento de marcadores análogos. Os marcadores com o radioisótopo ^{18}F revelam-se os mais promissores para deteção de tumores no cérebro. Mais especificamente, o marcador O-(2-^{18}F-Fluoroetil)-L-tirosina (FET) provou ser de grande importância na determinação da dimensão de tumores cerebrais e dos locais onde realizar a biopsia, no planeamento do tratamento a aplicar, e na deteção de recorrências. Foi também demonstrado que a forma como o FET é metabolizado ao longo do tempo depende do grau do tumor em estudo. Em gliomas de alto grau (HGG), a taxa de captação do FET é caracterizada por um pico inicial, seguido de uma diminuição da captação de FET, enquanto que em gliomas de baixo-grau (LGG) a taxa de captação do marcador tem um aumento contínuo ao longo do tempo.

O presente estudo contou com 11 pacientes (3 mulheres, 8 homens, idade: 45 ± 15 anos) com tumores cerebrais primários não tratados confirmados por histologia. Seis pacientes foram diagnosticados com HGG, enquanto os restantes 5 foram diagnosticados com LGG. Os dados de PET foram adquiridos com o PET Insert do sistema híbrido Siemens 3T MR-BrainPET. As imagens foram segmentadas de forma a extrair apenas o volume correspondente ao tumor. Após a segmentação, calculou-se a média das curvas de tempo-atividade (TAC) dos volumes tumorais segmentados (STVs), e foram usados métodos de regressão linear e não linear para fazer o ajuste à TAC de cada volume. Para calcular os ajustes com o modelo linear, foram descartados os primeiros 5 minutos de aquisição. Os ajustes baseados na regressão não-linear foram aplicados à TAC correspondente à média entre os 2 e os 60 minutos de aquisição após a injeção. As imagens dos parâmetros foram calculadas a partir dos ajustes baseados na regressão não linear e aplicados a cada voxel. Foram testados três modelos não lineares diferentes: um modelo linear amortecido exponencialmente, um modelo linear amortecido exponencialmente e com um offset, e um modelo linear amortecido exponencialmente com o tempo dependente da raiz quadrada. Dos ajustes não lineares, foram extraídos dois parâmetros: a amplitude, *A*, e o parâmetro κ. De seguida, geraram-se as imagens dos parâmetros calculados sobre uma área tridimensional selecionada manualmente e contendo o tumor. Para tal, além dos três modelos não lineares, utilizou-se também o modelo linear, de modo a permitir uma comparação entre os diferentes métodos. No caso dos ajustes lineares, os parâmetros extraídos foram a ordenada na origem e o declive. Calcularam-se também as imagens dos parâmetros da regressão não linear usando o modelo linear amortecido exponencialmente com o tempo dependente da raiz quadrada para a cabeça inteira.

Os modelos não-lineares foram mais precisos na reprodução das curvas de FET. Os modelos mais robustos foram os modelos lineares exponencialmente amortecidos sem offset. Nos ajustes aplicados à TAC média dos STVs, o modelo linear amortecido exponencialmente com o tempo dependente da raiz quadrada provou ser o que reproduz mais precisamente os dados, com valores de R^2 entre 0,94 e 1,00. O parâmetro A do modelo linear amortecido exponencialmente com o tempo dependente da raiz quadrada foi o único que revelou uma diferença significativa entre HGG e LGG (p-value= 0.04, α=0.05). Ao gerar imagens paramétricas com base nos ajustes aplicados a cada voxel, os modelos de regressão não-linear com 2 parâmetros tiveram o melhor desempenho, com valores de R^2 perto de 1. Combinando as imagens do parâmetro amplitude e as imagens da atividade total ao longo do tempo, foi possível distinguir entre graus tumorais. Os LGGs assumem valores de amplitude próximos dos valores do tecido saudável à sua volta, e por isso "desaparecem" da imagem paramétrica da amplitude. No caso dos HGGs, a imagem da amplitude reproduz a atividade no tumor. Os ajustes realizados com base na regressão linear devolveram valores de R^2 próximos de zero, quer no caso dos

STVs, quer no cálculo das imagens paramétricas. A distinção entre HGG e LGG é possível com base nas imagens paramétricas do declive, com os LGGs a assumirem valores de declive superiores aos do tecido saudável adjacente. Com os HGGs, a situação é a oposta: os valores do declive no tumor são inferiores aos do tecido saudável que o rodeia. Em geral, os modelos não lineares reproduzem melhor os dados provenientes de FET PET, mas a distinção entre HGG e LGG baseada num parâmetro apenas é melhor conseguida através de regressão linear. No entanto, a distinção entre HGG e LGG também é possível analisando simultaneamente as imagens dos parâmetros A e κ.

Palavras-chave: *PET; FET; modelação; não-linear; voxel-a-voxel.*

Index

List of figures

List of tables

List of abreviations

BBB	Blood-Brain Barrier
CT	Computed Tomography
FDG	^{18}F-Fluorodeoxyglucose
FDOPA	L-3,4-Dihydroxy-6-^{18}F-fluorophenylalanine
FET	O-(2-^{18}F-Fluoroethyl)- L-tyrosine
FMISO	^{18}F-Fluoromisonidazole
HG(G)	High-grade (Glioma)
LG(G)	Low-grade (Glioma)
MET	^{11}C-Methionine
MRI	Magnetic Resonance Imaging
PET	Positron Emission Tomography
ROC	Receiver Operating Characteristic
ROI	Region of Interest
STV	Segmented Tumour Volume
SUV	Standard Uptake Value
TAC	Time-activity Curve
TBR	Tumour-to-Brain Ratio
TTP	Time-to-Peak
WHO	World Health Organization

1. Introduction

1.1. PET tracers in Brain Imaging

The first step in a Positron Emission Tomography (PET) study is the production of the radiopharmaceutical. Development of specifically targeted radiopharmaceutical enables us to study the biochemistry of the brain due to the very high sensitivity of this imaging method. The ability to study biomolecules at a nanomolar to picomolar concentration *in vivo* allows a systematic study of various physiological processes. These advancements in imaging technology have further enhanced our capability to study the various processes in small brain regions.

Metabolic studies using ^{18}F-fluorodeoxyglucose (FDG), various amino acids such as ^{11}C-methionine (MET) and O-(2-^{18}F-Fluoroethyl)- L-tyrosine (FET), and perfusion studies with ^{15}O-labelled molecules have now been carried out for a number of years. Neurochemical processes in the brain are the primary targets for many new radiopharmaceuticals. There are numerous neurochemical pathways in the brain, and each one comprises a large number of proteins that are involved in health and disease.

Once the radiopharmaceutical is available, it is introduced into the patient's body, usually by injection. The time between the administration of the radiopharmaceutical and the beginning of data acquisition depends on the purpose of the imaging study and the nature of the tracer. Data acquisition takes place with the patient laying still in a bed. The radioactive isotope with which the radiopharmaceutical has been labelled emits gamma rays as a product of radioactive decay. As the gamma rays emanate from the patient, they are detected and recorded by imaging hardware. Positional and directional information about each gamma ray are measured, and the results are tailed into a histogram of discrete position-direction bins. The resulting histogram bins contain measurements of the projections. The projection data is then used to estimate the desired tomographic images. The final step is image analysis.

1.1.1. FDG

The phosphorylation of glucose, an initial and important step in cellular metabolism, is catalyzed by hexokinases (HKs). There are four HKs in mammalian tissue. One of them, the brain HK, is bound to mitochondria, enabling coordination between glucose consumption and oxidation. Tumour cells are known to be highly glycolitic, because of increased expression of glycolitic enzymes and HK activity. The HKs, by converting glucose to glucose-6-phosphate, help to maintain the downhill gradient that results in the transport of glucose into cells through the facilitative glucose transporters [1].

FDG is actively transported across the blood-brain barrier (BBB) into the cell, where it is phosphorylated by the brain HK to FDG-6-phosphate. FDG-6-phosphate cannot be metabolized further in the glycolitic pathway and stays in the cells. Tumour cells do not contain a sufficient amount of glucose-6-phosphatase to reverse the phosphorylation. The elevated rates of glycolysis and glucose transport in many types of tumour cells enhance the uptake of FDG in these cells compared to other normal cells [1].

Imaging of brain tumours with FDG was the first oncologic application of PET [2]. The prognostic value of FDG uptake is well established [3]. However, studies have demonstrated some diagnostic limitations of FDG PET [4]. Because of the high rate of physiologic glucose metabolism in normal brain tissue, the capacity of detecting tumours with only modest increases in glucose metabolism, such as low-grade tumours and in some cases recurrent high-grade tumours, is difficult. FDG uptake in

low-grade tumours is usually similar to that in normal white matter, and uptake in high-grade tumours is similar to that in normal grey matter, thus decreasing the sensitivity of lesion detection. Furthermore, it was demonstrated that FDG uptake in tumours could be increased whereas glucose metabolism could not [5]. Also, FDG uptake can vary greatly. High-grade tumours may have uptake that is only similar or slightly above that in white matter, especially after treatment [6].

Besides tumour imaging, the clinical applications of FDG PET are Alzheimer's disease, dementia, epilepsy, brain trauma, Huntington disease, Parkinson's disease, cerebrovascular disorders, Schizophrenia, and mood disorders. This tracer is also widely used in oncology, and cardiovascular disorders [1].

1.1.2. FET

Amino acid PET tracers and amino acid analogue PET tracers constitute a class of tumour imaging agents. So far, some 20 amino acid transporter systems have been identified [7]. Most of the amino acids are taken by tumour cells through an energy-dependent L-type amino acid transporter system and a sodium-dependent transporter system A [7]. They are retained in tumour cells due to these cells higher metabolic activities, including incorporation into proteins. This makes amino acid PET tracers particularly attractive for imaging brain tumours, since the high uptake in tumour tissue and low uptake in normal brain tissue leads to higher tumour-to-healthy-tissue contrast. The best studied amino acid tracer is ^{11}C-metionine (MET) [8], but because of the short half-life of ^{11}C (20 minutes), ^{18}F-labeled amino acid analogues have been developed for tumour imaging.

FET is a promising tracer for routine clinical practice. An efficient radiosynthesis is available, which allows using the tracer in a satellite concept. Like the other non-natural amino acids, FET is not incorporated into proteins. It is retained inside the tumour cells because of their high cellular metabolism and their high activity of the amino acid transporters. The tracer is metabolic stable *in vivo* and exhibits favourable uptake kinetics for clinical mapping [8]. Figure 1.1 shows the chemical structure of the FET tracer.

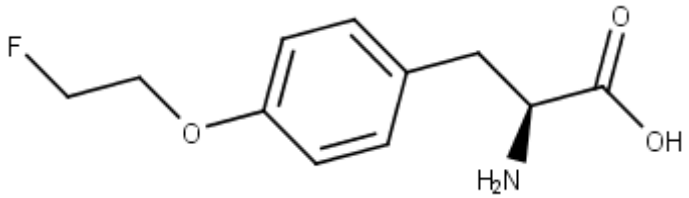

Figure 1.1 - Chemical structure of the FET tracer (adapted from [9]).

In brain tumour imaging, FET PET is very helpful to image the extent of cerebral gliomas, to guide biopsy, to detect tumour recurrences and to differentiate recurrences from radionecrosis. This metabolic information is useful for therapy planning and adds to the results of morphological imaging of CT and MRI. Nevertheless, increased regional uptake of FET in the brain is not absolutely specific for glioma tissue, and some exceptions have been reported [10]. FET PET is not able to differentiate the grade of malignancy of gliomas when using the standard ratio method [11], which is based on a tumour to background ratio in the later uptake phase. However, some studies indicate that differences in uptake kinetics are related to tumour grading [12]. This is an important issue since the decision on therapeutic intervention is crucial in these patients. Concerning extracranial tumours, FET PET is able to image squamous cell carcinomas, but the sensitivity is inferior to that of FDG PET. Even so, it may be a helpful

additional tool in selected cases for the differentiation of tumour tissue and inflammatory tissue. Figure 1.2 shows the differences in delineation of a high-grade glioma using FDG and FET.

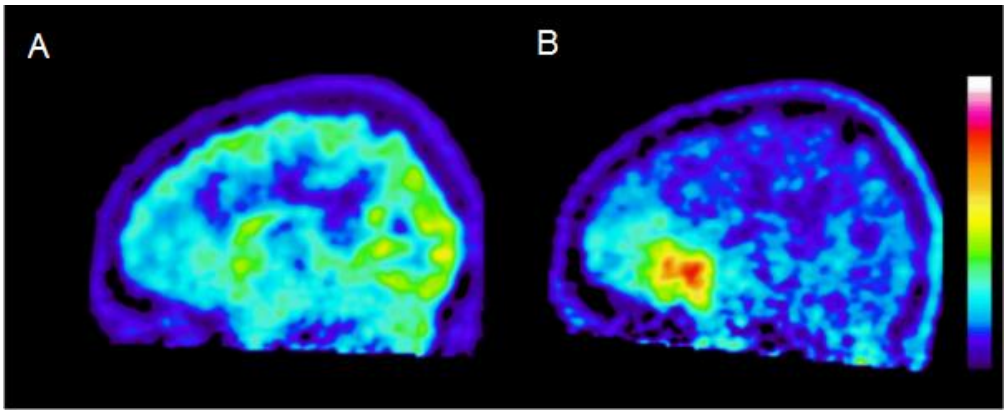

Figure 1.2 - High-grade glioma in the frontal lobe. (A) FDG PET. (B) FET PET. Delineation of the tumour is difficult on FDG images, while FET depicts the solid tumour mass and indicates an optimal biopsy site [13].

1.1.3. Other tracers

Besides FDG and FET, there are a large number of PET tracers available for clinical use. In this section, a quick overview of the more often used tracers is given.

MET has been widely used in detection of brain, head and neck, lung, and breast cancer as well as lymphomas. It can cross the BBB, and it is incorporated mainly into proteins, but also into lipids, RNA and DNA. MET PET imaging is more sensitive to radiotherapy compared to FDG and is useful for monitoring treatment of cancer [14].

One of the characteristics of tumour cells is their unchecked proliferation. It is important to measure the proliferation rate of cancer lesions to help differentiate benign from malignant tumours and to characterize malignant tumours among normal tissues. FDG has been widely used in cancer imaging. However, enhanced uptakes of FDG also occur in inflammatory cells and lesions as well as in necrotic cells. Thymidine (TdR) and its analogues are standard markers for DNA synthesis, and ^{11}C-thymidine has been used in PET to measure tumour growth rate in situ. Because of the short half-life of ^{11}C and extensive metabolism of ^{11}C-TdR in the blood, 3'-Deoxy-3'-^{18}F-fluorothymidine (FLT) was developed as an alternative. This tracer is an analogue of TdR and it is phosphorilated by an enzyme expressed during the DNA synthesis phase of the cell cycle. Most cancer cells have much higher activity of such enzyme than normal cells. Thus, the uptake and accumulation of FLT are used as an index of cellular proliferation, allowing for evaluation of tumour stage and metastases detection [15].

There has been a multitude of efforts to develop methods and imaging techniques for measuring oxygen in tissues. Hypoxia in malignant tumours can affect the outcome of anti-cancer treatments. Malignant tumours are relatively resistant to chemotherapy and irradiative therapy because of their lack of oxygen, which is a potent radiosensitizer. ^{18}F-Fluoromisonidazole (FMISO) was proposed as a tracer for determining tumour hypoxia in vivo. It is used to quantitatively assess tumour hypoxia in lung, brain, and head and neck cancer patients, and also in patients with myocardial ischemia. Because of the slow reaction mechanisms and the absence of the active transport of the tracer molecules, the identification and quantification of hypoxic tumour areas demand long examination protocols [16].

Dopamine, a neurotransmitter, plays an important role in the mediation of movement, cognition and emotion. It is involved in various neuropsychiatric disorders, such as schizophrenia, autism,

attention deficit hyperactivity disorder, and drug abuse. Dopamine is synthetized within nerve cells. L-thyrosine is converted to dihydroxyphenylalanine (L-DOPA) and then to dopamine in a two-step process. The first is a rate limiting step, where L-thyrosine is catalyzed by tyrosine 3-monoxygenase. The second step is catalyzed by aromatic L-amino acid decarboxylase. In parts of the nervous system that release dopamine as a neurotransmiter, no further metabolism occurs and dopamine is stored in vesicles in the presynaptic nerve terminals through the dopamine reuptake transporter [17].

FDOPA is a radiolabeled analogue of L-DOPA used to evaluate the central dopaminergic function of pre-synaptic neurons. FDOPA PET reflects dopamine transport into the neurons, dopamine decarboxylation and dopamine storage capacity. FDOPA is a very important tracer for monitoring Parkinson's disease progression and neuroprotection therapies. In recent studies, FDOPA has also demonstrated its usefulness in imaging brain tumours and neuroendocrine metastatic lesions in bone [17].

Raclopride is a substituted benzamide with high affinity and selectivity for central D2-dopamine receptors. The compound is a potential antipsychotic drug. Raclopride has been labelled with ^{11}C and used in human experiments with PET to quantitatively characterize central dopamine D2-dopamine receptor binding in the basal ganglia. ^{11}C-Raclopride accumulated markedly in the dopamine rich caudate nucleus and putamen, whereas the concentration of radioactivity in any of the extrastriatal regions could not be differentiated reliably [18].

^{11}C-Flumazenil is a carbon labelled benzodiazepine site antagonist with high affinity for $GABA_A$ receptors. It has been used widely in PET for the investigation of these receptors. The GABA receptors comprise several different pharmacological subtypes depending on the type of subunits constituting the receptor complex, and GABA mediates its effects primarily through the $GABA_A$ receptors. ^{11}C-Flumazenil is used to assess neurologic pathologies associated with the impairment of GABA neurotransmission, such as epilepsy [19].

1.2. Tracer kinetic modelling

Single PET images supply spatial information, but they also show accumulated information on kinetics. With the acquisition of dynamic imaging data and the application of kinetic models, many additional quantitative questions can be answered based on the temporal information. However, the main reason for kinetic modelling is that it allows true quantitative imaging instead of just accumulated information. Also, Standard Uptake Value (SUV) reaction rate constants of the underlying chemical processes can be assessed and imaged. There is a range of quantitative PET tracer kinetic modelling techniques that return biologically based parameter estimates. These techniques may be broadly divided into model-driven methods and data-driven methods. The clear distinction is that the data-driven methods require no *a priori* decision about the most appropriate model structure. On the other hand, for the model-driven methods, this information is obtained directly from the kinetic data [20].

1.2.1. Compartmental modelling

In PET, the images are a composite of various superimposed signals, only one of which is of interest. The desired signal may describe, for example, the amount of tracer trapped at the site of metabolism or tracer bound to a particular receptor. In order to isolate the desired component of the signal, a model relating the dynamics of the tracer and all its possible states to the resultant PET image must be used. Each of the states is known as a compartment. For example, in a receptor-imaging study, the set of molecules that are bound to the target receptor can constitute one compartment. Each

compartment is characterized by the concentration of the tracer inside as a function of time. These concentrations are related through sets of ordinary differential equations, which express the balance between the mass entering and exiting each compartment.

Kinetic models for PET typically derive from the one- two-, or three-compartment model in which a directly measured concentration of tracer in the blood as a function of time (time-activity curve, TAC) serves as the model's input function. The coefficients of the differential equations in the model are constants that reflect the kinetic properties of the tracer in the system. By formally comparing the output of the model to the experimentally obtained PET data, it is possible to estimate values for these kinetic parameters, and thus extract information about binding, delivery, or any hypothesized process [20].

The concentration of radioactivity in a given tissue region at a particular time post-injection primarily depends upon two factors. First, and of most interest, is the local tissue physiology, for example, the blood flow or metabolism in that region. Second is the input function, i.e., the time-course of tracer radioactivity concentration in the blood or plasma, which defines the availability of the tracer to the target-region. A model is a mathematical description of the relationship between tissue concentration and these two controlling factors. A full model can predict the TAC concentration in a tissue region from knowledge of the local physiological variables and input function. A simple model might predict only certain aspects of the tissue concentration curve, such as the initial slope, the area under the curve, or the relative activity concentration between the target organ and a reference region.

Compartmental models use a particular structure to describe the behaviour of the tracer and allow for an estimation of either micro or macro system parameters. If the appropriate tracer is selected and suitable imaging conditions are used, the activity values measured in a region of interest (ROI) in the image should be most heavily influenced by the physiological characteristic of interest: blood flow, receptor concentration, etc. A model attempts to accurately describe the relationship between the measurements and the parameters of interest. In other words, an appropriate tracer kinetic model can account for the biological factors that contribute to the tissue radioactivity signal [21].

Once a radioactive tracer has been selected for evaluation, there are a number of steps involved in developing a useful model and a model-based method. Figure 1.3 gives an overview of this process. *A priori* information concerning the expected biochemical behaviour of the tracer is used to specify a complete model. Initial modelling studies will define an identifiable model, i.e., a model with parameters that can be determined from the measurable data. Validation studies are used to refine the model, verify its assumptions, and test the accuracy of its estimates. After optimization procedures, error analysis, and accounting patient logistical considerations, a model-based method can be developed that is both practical and produces reliable, accurate physiological measurements. Well-established compartmental models in PET include those used for quantification of blood flow [22], cerebral metabolic rate for glucose [23] and for neuroreceptor ligand binding [24]. Parameter estimates are obtained from *a priori* specified compartmental structures using one of a variety of least-squares fitting procedures: linear least squares, non-linear least squares [25], generalized linear least squares [26], weighted integration [27] or basis function techniques [28].

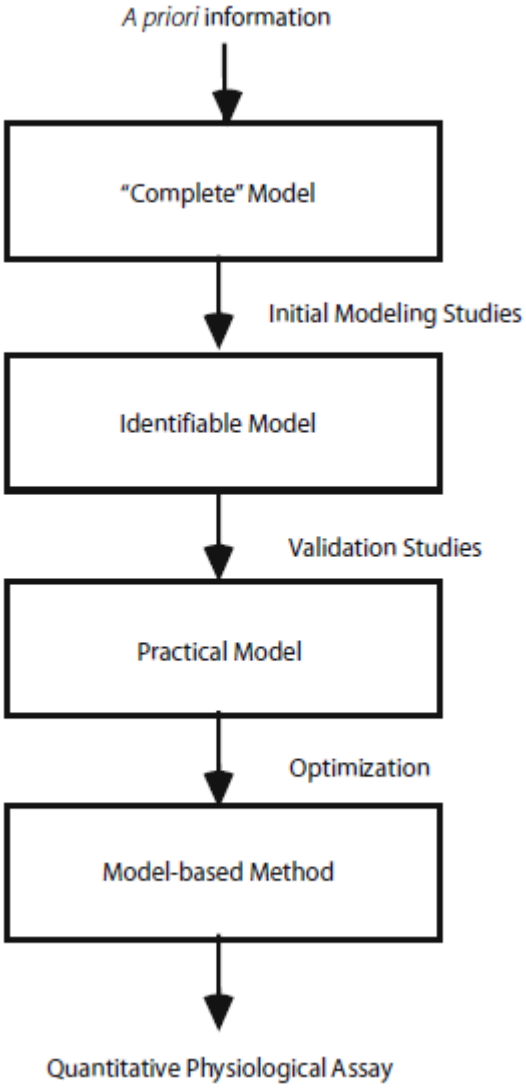

Figure 1.3 - Steps for developing a model [21].

1.2.2. Graphical analysis

Simplifications of compartmental modelling have been proposed. These easier methods offer some advantages over non-linear model optimization, such as avoiding parameter sensitivity to noise, parameter co-variance, local minima in optimization, and dependence on model parameter starting conditions [29]. They derive macro system parameters from a less constrained description of the kinetic processes. Graphical analysis is applied to compounds that can be modelled as having a compartment of irreversible or nearly reversible binding. Irreversible radioligands are the ones which bind permanently, while reversible radioligands remain linked together with a receptor for a while, and then dissociate.

The two most used graphical methods are the Patlak Plot [30] and the Logan Plot [31]. The Patlak approach is a description of the behaviour of the FDG-model when the free FDG in tissue has reached its steady state so that the ratio between radioactivity concentration in tissue and radioactivity concentration in arterial blood becomes time independent. It assumes that all the reversible compartments must be in equilibrium with the plasma. Under this condition, only tracer accumulation

in the irreversible compartments is affecting the apparent distribution volume. When there is no irreversible binding in the tissue, the Patlak plot has slope zero. When the tissue presents irreversible binding, the Patlak plot becomes linear once equilibrium is achieved, and the slope of the linear phase represents the net transfer rate, k_i. This constant represents the amount of accumulated tracer in relation to the amount of tracer available in the plasma [32].

The Logan plot has been developed for the evaluation of investigations with reversible radioligands. Logan *et al*. [31] showed that there is a time *t* after which a plot of $\int_0^t ROI(t')dt'/ROI(t)$ versus $\int_0^t C_p\,(t')dt'/ROI(t)$ (where ROI and C_p are functions of time describing the variation of tissue radioactivity and plasma radioactivity, respectively) is linear with a slope that corresponds to the steady-state space of the ligand plus the plasma volume, V_p. This graphical method provides the ratio B_{max}/K_d (where B_{max} represents ligand binding sites and K_d the equilibrium dissociation constant of the ligand-binding site) from the slope comparison with *in vitro* measures of the same parameter, as well as volume distribution. It also provides an easy, rapid method for comparison of the reproducibility of repeated measures in a single subject, for longitudinal or drug intervention protocols, or for comparing experimental results between subjects. Figure 1.4 shows the input for this method, and its resulting output.

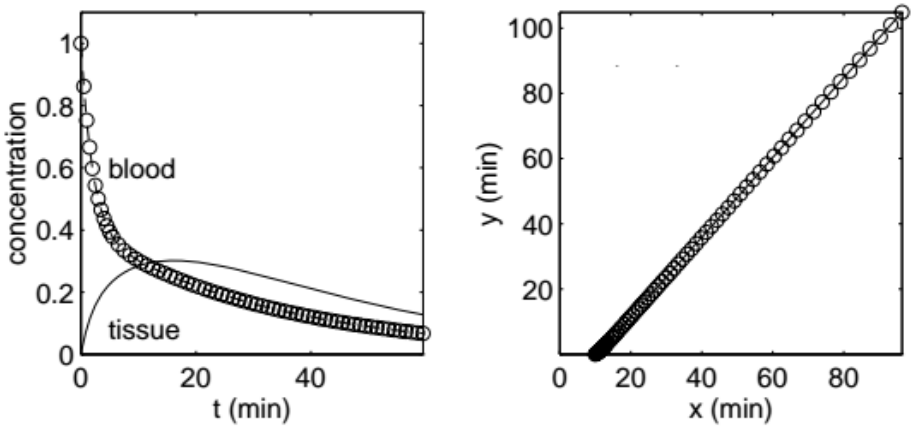

Figure 1.4 - Logan plot. The input is shown on the left, and the output is shown on the right (adapted from [33]).

In this case, a graphical approach can be used to estimate the flux constant describing movement from the blood into the trapped compartment, as previously described for kinetic analysis. These techniques represent a reformulation of the 2-compartment model offering a simple linear regression method to derive metabolic flux of the tracer using a blood clearance curve and a tissue TAC [29].

However, these types of methods require the determination of when the plot becomes linear. Also, a primary assumption for graphical analysis is that loss of tracer does not occur from the retained compartment. When loss occurs, the plot deviates from linearity making selection of the linear components difficult. Graphical analysis methods may also be biased by statistical noise, and they fail to return any information about the underlying compartmental structure. One important limitation is that, in order to acquire the values for C_p, these methods require blood sampling. Ideally, blood sampling should be done from arteries, which is potentially dangerous for the patient and requires skilled professionals. At the beginning, blood samples with temporal intervals of around 5 to 15 seconds are acquired. Activity measurements are performed in all blood samples, and often in the plasma alone. This means the plasma has to be separated from blood metabolites. This accounts for a very sophisticated method, not suited for clinical routine.

1.2.3. Other modelling approaches

Besides graphical analysis, other compartmental modelling alternatives have been developed. Spectral analysis, for example, is a type of data-driven approach that characterizes the system impulse response function (IRF) as a positive sum of exponentials and uses nonnegative least squares to fit a set of these basis functions to the data. The macro system parameters of interest are calculated as functions of the IRF. Spectral analysis also returns information on the number of tissue compartments evident in the data [20].

Another approach is the application of residue analysis to imaging studies. PET tracers are assumed to behave in a linear, time-invariant fashion at the local tissue level, and can be described by an impulse response function. Kinetic analysis of compartmental models rely on this impulse response assumption. Nonparametric evaluation of the residue function has found use in fields outside of PET [34]. Residue analysis allows for rapid quadratic-programming based methods for computation and more accurate representation of data [35].

Lastly, reference tissue compartmental models have been developed. Instead of plasma samplings, these models use the TAC of a reference region with non-existent or very low specific uptake. Reference tissue models are used to estimate binding potential from reversible ligand-receptor PET studies. Their main advantage is that since blood sampling and plasma metabolite analysis are not needed, errors caused by uncertainties in the measured plasma metabolite fractions are avoided [36].

1.3. Parametric Imaging in PET

Parametric imaging consists of estimating model parameters on a voxel-by-voxel level basis to generate images or maps of parameters. This means that instead of just displaying tracer uptake, physiological or even chemical parameters, like binding potential and rate constants, can be estimated and imaged. Parametric imaging reveals the heterogeneity of tumours down to the image sampling distance and avoids the inherent bias of defining tissue ROIs from summed or anatomic images.

Once a tracer has been evaluated, data acquired, and the appropriate model and parameters defined, the next step is to perform parameter estimation. In dynamic PET studies, the changing activity of the injected radiotracer is conventionally measured through multiple consecutive time frames. The image of the radioactivity distribution in each frame is reconstructed independently and the whole set of frames is then used to estimate the distribution of the physiologic parameter of interest by the application of an appropriate model to the TAC either of selected ROIs or of each image element. If this is performed using the TAC of each voxel, parametric images can be obtained. This two-step indirect method for obtaining the kinetic parameters of the model is illustrated in Figure 1.5A. From a statistical point of view, the weighted nonlinear least squares method is very straight-forward to use, and very broadly applied. The process is nonlinear because the kinetic model equations are generally nonlinear with respect to at least one parameter. For PET, the data in each time frame are independent. For Fourier-based algorithms, the weighted least-squares approach is very successful when the tracer kinetics are accurately described by a 1-tissue compartment model [37].

A variety of procedures have been developed to allow the mapping of kinetic parameters on a voxel-level basis. The computational simplicity of the graphical techniques explained above makes them particularly suited to a voxel-based approach.

Nonetheless, there are a number of potential problems that arise in voxel-by-voxel parameter estimation. The high statistical noise of single-voxel data can lead to bias in the parameter estimates from the nonlinear models, particularly when the final parameter of interest is a ratio of kinetic values. Also, since the statistical quality of the data is a function of the actual parameter values, apparent image

artefacts can appear in certain regions of the brain, even those with less biological interest, such as white matter, due to poorer estimation characteristics [37]. As models become more complex, computation speed is also an issue.

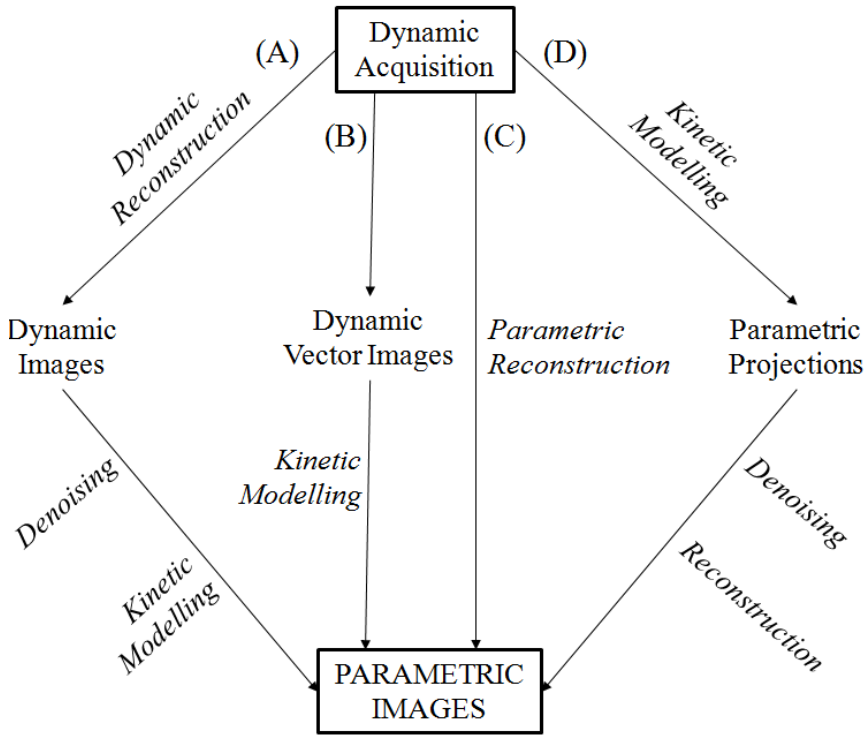

Figure 1.5 - Schematic representation of the methods used for parametric estimation (adapted from [38]).

More common and simpler approaches involve graphical and integration methods. These techniques are usually derived from integration of the model differential equations to produce equations that are linear in the parameters. Some of these approaches achieve a level of model independence by fitting only a portion of the measured data to an equation with less parameters. This requires the definition of the critical starting time period for fitting, which is tracer, subject and sometimes region-dependent. However, it is important to recognize that, for some of these approaches, the estimation process is nonlinear because measured data appear both as dependent and independent variables.

Alternatives to this approach are depicted in Figure 1.5. For example, temporal basis functions can be used to accommodate temporal information in the reconstruction step (Figure 1.5B). The TAC is represented as a sum of temporal functions (B-splines or other sophisticated functions). These methods estimate the weight of each temporal basis component for every voxel and produce activity maps with higher spatial resolution for comparable variance. The kinetic parameters are then estimated from the dynamic images [38].

Direct parametric reconstruction approaches (Figure 1.5C) estimate the kinetic parameters from the emission data. Conceptually, the process is similar to fitting measured data to a model, which is parameterized using kinetic parameters for each voxel or region. The model consists of two components: a kinetic model, which translates the time-varying radioactivity for each voxel or region, and a model for the measurement by the scanner. The fit is determined by minimizing an appropriate objective function related to the discrepancy between the measured data and the output of the model.

Lastly, projection based methods (Figure 1.5D) where the kinetic modelling step is applied directly to the projection data prior to reconstruction can also be used.

1.4.Brain tumour types and grades

Brain tumours are a heterogeneous group of diseases, each with its own biology, prognosis, and treatment. The most common tumour types are metastatic tumours and malignant gliomas. Any tumour that arises from the glial, or supportive tissue, of the brain is called glioma. According to the classification of the World Health Organization (WHO), gliomas are of 3 main types: astrocytomas, oligodendrogliomas, and mixed oligoastrocytomas. These tumours are typically heterogeneous in that different levels of malignant degeneration can occur in different regions within the same tumour. Histological grading is a means of predicting the biological behaviour of a tumour. In the clinical setting, tumour grade is a key factor influencing the choice of therapies, particularly determining the use of adjuvant radiation and specific chemotherapy protocols. The WHO classification of tumours of the nervous system includes a grading scheme that is a malignancy scale, ranging across a wide variety of neoplasms [39].

Analysis of the most malignant region of the tumours establishes grading, which is based on the degree of nuclear atypia, mitosis, microvascular proliferation and necrosis (Figure 1.6). Grade I applies to lesions with low proliferative potential and the possibility of cure following surgical resection alone. Neoplasms designated grade II are generally infiltrative in nature, and despite low-level proliferative activity, often recur. Some type II tumours tend to progress to higher grades of malignancy. The designation WHO grade III is generally reserved for lesions with histological evidence malignancy, including nuclear atypia and brisk mitotic activity. Lastly, the designation WHO grade IV is assigned to cytologically malignant, mitotically active, necrosis-prone neoplasms typically associated with rapid pre-postoperative disease evolution and a fatal outcome [39].

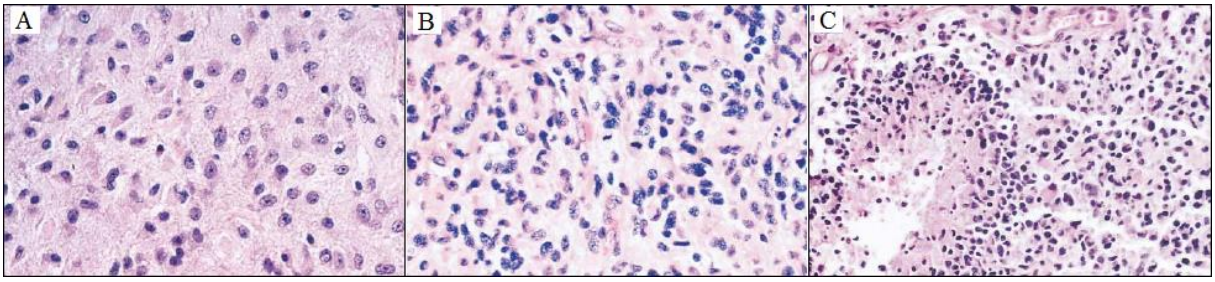

Figure 1.6 - Histologic criteria of the WHO for the classification of gliomas. (A) Fibrillary astrocytoma is characterized by increased cellularity. (B) Anaplastic astrocytoma is characterized by nuclear atypia and mitoses. (C) Glioblastoma multiform is characterized by necrosis with cells arranged around the edge of the necrotic tissue (adapted from [40]).

1.4.1. Low-grade Gliomas

Low-grade gliomas correspond to WHO grades I and II. There are 3 subtypes of low-grade gliomas: pilocytic astrocytoma, astrocytoma and oligodendroglioma [10].

Astrocytomas are tumours found in young adulthood, with a peak incidence in the third or fourth decade of life. They arise from astrocytes, star-shaped glial cells in the brain and spinal cord that, among other functions, provide biochemical support of the endothelial cells that form the BBB. Typically, the first clinical manifestation is a seizure, which may be accompanied or followed by other neurological symptoms or signs. The diagnosis is usually established when neuroimaging is performed to evaluate the seizure. In patients presumed to have low-grade gliomas, MRI is supplemented by PET, since these tumours are characterized by glucose hypometabolism. PET images showing diffuse hypometabolism may support a decision to defer surgery or radiation therapy. If hypermetabolic areas are present,

indicating the presence of a high-grade tumour, biopsy or resection should target those areas in an effort to include the most malignant tissue in the tumour volume [39, 40].

Because most patients with astrocytoma are young and neurologically normal, treatment is particularly challenging. When the lesion is amenable to complete surgical excision, resection is performed. However, the majority of the low-grade tumours are not amenable to resection because they involve too large an area of the brain, or are too close to critical structures.

Most astrocytomas progress to high-grade malignant gliomas, which are often marked by hypermetabolic areas on PET scans. The median survival of patients with low-grade astrocytomas is 5 years, and most patients die from progression of their disease to a high-grade malignant glioma [40].

Oligodendrogliomas and oligoastrocytomas are tumours of oligodendrocytes or their precursors. Oligodendrocytes are a type of neuroglia which function is to provide support and insulation to axons in the central nervous system. The majority of oligodendrogliomas are low-grade and radiographically indistinguishable from astrocytomas, although oligodendrogliomas are more likely to be calcified. These oligodendroglial tumours are prone to spontaneous haemorrhage, as a result of their delicate vasculature. Most patients present a seizure, or progressive hemiparesis, or cognitive impairment.

The issues concerning diagnosis and treatment are identical to those for low-grade astrocytomas. Treatment is deferred until there is clinical or radiologic evidence of progression, unless patients have disabling symptoms or signs at presentation. However, once the decision to initiate treatment is made, the therapy differs from that for astrocytomas.

Eventually, most oligodendrogliomas, like astrocytomas, progress by becoming malignant. Patients with worsening clinical symptoms and the appearance of hypermetabolism on PET scans warrant re-evaluation.

1.4.2. High-grade Gliomas

High-grade gliomas are classified as malignant astrocytomas, anaplastic astrocytoma, and glioblastoma multiforme. These are also the most common glial tumours. Gliomas can occur anywhere in the brain, but usually affect the cerebral hemispheres. The male to female ratio among affected patients is about 3:2. The peak age at onset for anaplastic astrocytomas is in the fourth or fifth decade, whereas glioblastomas usually present in the sixth or seventh decade [40].

The glioblastoma multiform is the most malignant and most common glioma. There are two types of glioblastomas, and they arise through different molecular pathways. Primary glioblastomas arise alone and are associated with a high rate of overexpression or mutation of the epidermal growth factor receptor, p16 deletions, and mutations in the gene for phosphotase and tensin homologues. Secondary glioblastomas arise from a pre-existing low-grade tumours. In a secondary glioblastoma, a low-grade tumour may be immediately adjacent to a highly malignant disease. Error can occur when a small sample is taken for biopsy and the examined tissue does not reflect the biology of the entire tumour, particularly if features indicative of malignancy are missed. All gliomas, particularly the astrocytic neoplasms, are histologically, genetically, and thus therapeutically heterogeneous [40].

Primary glioblastomas tend to occur in older patients (mean age, 55 years), whereas secondary glioblastomas occur in younger adults (45 years old or less). The histologic features of the tumour and the age and performance status of the patient are major prognostic factors on outcome [10,40].

Malignant gliomas are surrounded by edema, and the mass effect can be severe enough to cause herniation. The tumour typically involves white matter and can spread across the corpus callosum and involve both hemispheres. These tumours are widely infiltrative. Tumour cells typically extend microscopically several centimeters away from the obvious area of disease and, in some cases, can extend throughout large portions of the brain. This condition is known as gliomatosis [10,40].

The treatments for anaplastic astrocytoma and glioblastoma multiform are identical. Resection is the initial intervention. Gross total excision is associated with longer survival, and improved neurologic function; therefore, every effort should be made to remove as much tumour as possible. Radiotherapy and additional chemotherapy are also prescribed. However, despite aggressive treatment, most patients die of the disease, with median survival of about 3 years for anaplastic astrocytoma, and one year for glioblastoma.

Oligodendrogliomas can also be classified as high-grade. These anaplastic oligodendrogliomas, like malignant astrocytic tumours, require immediate treatment after diagnosis. Extensive resection should be performed if feasible.

1.5. Imaging of Brain Tumours

As previously stated, the degree of malignancy plays a crucial role in assessing the prognosis of glioma patients and in planning appropriate individual management. Therefore, tissue diagnosis (biopsy) is the current diagnostic gold standard for determining tumour grade, which in turn forms the basis for subsequent treatment decisions. Generally a biopsy procedure is safe, but complications, such as bleeding or infection, may occur. In some cases, the amount of tissue obtained from a needle biopsy may not be sufficient or the procedure is unable to detect some lesions. The biopsy may then have to be repeated or surgical biopsy will be necessary. Hence, non-invasive alternatives for tumour diagnosis are sought after. The value of PET using radiolabeled amino acids or analogues for non-invasive tumour grading remains controversial [41]. The following section provides an overview of the studies performed to determine the diagnostic value of FET in brain tumours, including comparisons with other widely used tracers and imaging techniques.

1.5.1. Comparison between FET PET and FDG PET

The diagnostic value of PET using FDG and FET in patients with brain lesions suspicious of cerebral gliomas was studied [43]. Within a 2-year period, a group of 59 adult patients admitted with suspicion of a cerebral glioma or a recurrence of a previously operated glioma was studied with FET and FDG PET. The patients were examined on the same day prior to a neuronavigated biopsy or open surgery. Preoperative MRI, FET and FDG PET scans were co-registered and evaluated by ROIs using dedicated software. From the initial 59 patients, 52 were analysed. 43 patients had diffuse gliomas, of whom 33 had primary tumours and 10 recurrences. The extent of the tumour could be clearly delineated in each patient. In 33 of 43 patients a local maximum could be identified on FET scans for biopsy guidance. On the other hand, only 15 of the 43 patients had elevated FDG uptake. The definition of tumour extent remained impossible in every case due to high FDG uptake in the grey matter. Thus, FET proved to be clearly superior to FDG PET for biopsy guidance and treatment planning of cerebral gliomas, since FET identified a metabolic hot spot in the tumour area in 76% of the patients (33 out of 43), while FDG showed focally increased uptake in 28 gliomas only (out of 43).

Another study in patients with suspected or known brain tumours was performed by Lau *et al.* [44]. The aim of the study was also to establish the diagnostic value of FET PET when compared with FDG PET. Twenty-five FET PET and FDG PET scans were performed on 21 patients within 24 months. Final malignant pathology included 11 gliomas, 8 of which were low-grade, and three high-grade. FET PET was 100% accurate in the assessment of low-grade gliomas, while FDG PET has a sensitivity of only 13%. Also, FET PET had a 67% sensitivity for high-grade glioma against 33% sensitivity of FGD PET. The evaluated group of patients also comprised two lymphomas, one olfactory

ganglioneuroblastoma, and one anaplastic meningioma. FET PET was 100% accurate in the lymphoma group. Benign pathology included two encephalitis and one cortical dysplasia. Definitive pathology was not available for 3 patients. The accuracy of PET was determined by subsequent surgical histopathology in 12 patients and clinical/imaging course in nine patients. Median follow-up period was 20 months.

The predominant clinical indication for initial PET in this study was suspected recurrent tumour following previous treatment, representing a subgroup of 14 out of 21 patients. Of these, 7 patients had a history of glioma, 5 had cerebral lymphoma. In this category, FET PET had a sensitivity of 89%, specificity of 100% and accuracy of 93%. On the other hand, FDG PET had a sensitivity of 33%, specificity of 80% and accuracy of 50%. No lesion was correctly classified by FDG PET that had not also been correctly diagnosed by FET PET. These results show that FET is superior to FDG as a PET tracer in the assessment of suspicious brain lesions, especially in low-grade glioma.

In the light of studies regarding the diagnostic potential of FET in gliomas, Pauleit *et al.* [45] investigated the usage of FET PET in patients with squamous cell carcinoma (SCC) of the head and neck region by comparing that tracer with FDG PET and CT. Twenty-one patients with suspected head and neck tumours underwent FET PET, FDG PET and CT within one week before operation. After co-registration, the images were evaluated by 3 independent observers and a Receiver Operating Characteristic (ROC) analysis was performed, with the histopathological result used as a reference. The maximum SUVs were also determined. In 18 of 21 patients, histological examination revealed SCC, and in 2 of these patients, a second SCC tumour was found at a different anatomic site. In 3 of 21 patients, inflammatory tissue and no tumour were identified by histology. Eighteen of 20 SCC tumours were positive for FDG and FET uptake. One 3.0 cm tumour was detected neither with FDG PET nor with FET PET. In a different patient, histological examination showed a 0.7 cm tumour in a 4.3 cm inflammatory ulcer. The FDG PET scan overestimated the carcinoma as a 4 cm lesion with increased FDG uptake, while the scan obtained with FET missed this small carcinoma. All carcinomas with increased FET uptake exhibited concordant FDG accumulation, and no additional lesion could be identified with FET PET. Furthermore, the SUVs for SCC were higher in all cases with FDG than with FET. Overall, the sensitivity of FDG PET was 93%, specificity was 79% and accuracy was 83%. FET PET yielded a lower sensitivity of 75%, but a higher specificity (95%), and an accuracy of 90%.

According to these results, because uptake and sensitivity are lower for FET than for FDG, FET does not represent an ideal tracer for the evaluation of primary SCC of the head and neck region. However, the higher specificity makes FET PET an interesting additional tool in the follow-up of patients with SCC. Thus, FET may not replace FDG in the PET diagnostic of head and neck cancer, but may be a helpful additional tool in selected patients by allowing better differentiation of tumour tissue from inflammatory tissue [45].

1.5.2. Comparison between FET PET and MRI

In another study, the diagnostic accuracy of FET PET and MRI was compared in 45 patients, 36 of which with gliomas and neurological diagnosis of tumour recurrence, while the remaining 9 had undergone radioimmunotherapy [46]. FET PET and MRI studies were performed in all patients. Tumour recurrence was documented in 31 of 45 patients. FET PET and MRI revealed a correct diagnosis in 44 and 36 patients respectively, and the difference was statistically relevant ($P<0.01$). Specificity and sensitivity of FET PET were 92.9% and 100% respectively, against 50% and 93.5% of MRI. The results confirmed FET PET as a powerful tool to distinguish between benign side effects of therapy and tumour recurrence in patients with gliomas.

Prognostic factors in adult patients with untreated, nonenhancing, supratentorial low-grade glioma were studied by Floeth *et al.* [47], with special regard to FET PET and MRI. FET PET and MRI

analysis were performed on 33 patients with histologically confirmed low-grade glioma. None of the patients had radiation or chemotherapy. Clinical, histological, therapeutical, FET uptake and MRI morphologic parameters were analysed for their prognostic significance. Baseline FET uptake and a diffuse versus circumscribed tumour pattern on MRI were highly significant predictors of prognosis ($P<0.01$). By the combination of these prognostically significant variables, 3 major prognostic subgroups of low-grade glioma patients could be identified, and the statistical analysis proved that they had significant survival differences. The first of these subgroups was composed of patients with circumscribed low-grade glioma on MRI without FET uptake. Progression occurred in 18% of the cases, and there were no signs of malignant transformation and no death. The second subgroup was patients with circumscribed low-grade glioma with FET uptake. For this subgroup, progression occurred in 46% of the cases, malignant transformation to a high-grade glioma occurred in 15% of the cases, and death rate was of 8%. The last subgroup was patients with diffuse low-grade glioma with FET uptake. Progression occurred in all cases, malignant transformation in 78%, and death in 56%. Given these results, the authors concluded that baseline amino acid uptake on FET PET and a diffuse versus circumscribed tumour pattern on MRI are strong predictors for the outcome of patients with low-grade glioma.

As mentioned in previous sections, brain tumours are histologically heterogeneous. MRI-guided stereostatic biopsy does not always yield a valid diagnosis or tumour grading, because some regions of the nonenhancing tumours may be high-grade. Accurate grading and diagnosis are especially important for directing the therapeutic approach and providing the prognosis in patients with nonresectable tumours. The added value of FET in diagnostic accuracy of MRI for location and extent of cerebral gliomas was investigated in [48]. PET with FET and MRI were performed on 31 patients with suspected cerebral gliomas. PET and MRIs were co-registered and 52 neuronavigated tissue biopsies were taken from lesions with both abnormal MRI signal and increased FET uptake, as well as from areas with abnormal MR signal but normal FET uptake or vice versa. The diagnostic performance for the identification of cellular tumour tissue was analysed for either MRI alone or MRI combined with FET PET using alternative free response receiver operating characteristics curves (ROCs). FET findings were negative in 3 patients with an ischemic infarct and demyelating disease, and these 3 patients were excluded from the study. Tumour was diagnosed in 23 out of the 28 remaining patients, and reactive changes were found in the other 5. The diagnostic performance of MRI alone was compared with that of MRI combined with FET. MRI yielded a sensitivity of 96% for the detection of tumour tissue but a specificity of only 53%; FET PET alone yielded a sensitivity of 93% and a specificity of 81%. Finally, combined use of MRI and FET PET yielded a sensitivity of 93% and a specificity of 94%. Given these results, the authors of the study concluded that combined use of MRI and FET PET significantly improves the accuracy of the distinction of cellular glioma tissue from peritumoural brain tissue. Combined MRI ad FET diagnostics seems to be especially useful in brain lesions without BBB disruption.

The follow-up of glioblastoma patients after radiochemotherapy with conventional MRI can be difficult since reactive alterations to the BBB with contrast enhancement may mimic tumour progression. This phenomenon has been termed pseudo progression (PsP), and is a consequence of subacute treatment-related local tissue reaction, which comprises inflammation, edema, and increased permeability of the BBB [49]. PsP occurs with or without clinical deterioration, though interestingly it seems to be associated with a better outcome, and it is more common between patients that are more responsive to temozolomide treatment [50]. The reliable differentiation of early tumour progression (EP) from PsP is crucial since PsP spontaneously resolves without changing the standard treatment and a correct diagnosis may prevent unnecessary and potentially harmful change in treatment. On the other hand, the reliable detection of tumour progression at an early stage is essential for optimizing the treatment strategy in the individual patient.

The clinical value of FET PET in the differentiation of PsP and early tumour progression (EP) after radiochemotherapy was assessed [51]. A group of 22 glioblastoma patients with new contrast-enhancing lesions or lesions showing increased enhancement (>25%) on standard MRI within the first 12 weeks after completion of radiochemotherapy with concomitant temozolamide were additionally examined with FET PET. Maximum and mean tumour-to-brain ratios (TBR_{max} and TBR_{mean}) were determined, as well as FET uptake kinetics parameters, namely TACs patterns. Classification as PsP or EP was based on the clinical course. PsP was confirmed in 11 out of the 22 patients. In patients with PsP, FET uptake was significantly lower (TBR_{max}=1.9 and TBR_{mean}=1.8, $P<0.001$) than in patients with EP (TBR_{max}=2.8 and TBR_{mean}=2.3, $P<0.001$). ROC analysis showed that the optimal FET TBR_{max} cut-off value for identifying PsP was 2.3 (sensitivity 100%, specificity 91% and accuracy 96%). Thus it is demonstrated that FET uptake TBRs and also tracer kinetics provide valuable clinical information for the differentiation of PsP from EP in glioblastoma patients, making FET PET a promising method for overcoming the limitations of conventional MRI.

1.5.3. FET PET in brain imaging

As mentioned in previous sections, FET PET has not been shown useful in differentiating low from high grade tumours if a single time point scan is performed. However, the kinetic profile in FET in low-grade and high-grade tumours was reported as a useful feature for distinguishing the two types of tumours. The purpose of the preliminary study by Weckesser *et al.* [52] was to evaluate the differential uptake of FET in suspected primary brain tumours. A FET PET study was performed in 44 patients referred for the evaluation of a suspected brain tumour. FET uptake above the cortical level was observed in 35 out of the 44 lesions. All histologically confirmed gliomas and many other lesions showed FET uptake to a variable extent. An analysis of uptake dynamics was done in the patients with increased FET uptake, comprising a group of 22 gliomas, three lymphomas, three non-neoplastic lesions, three lesions with unknown histology and four other primary tumours. Upon classification of tumours into low- and high-grade, a significant difference in maximum FET uptake between the two categories was observed only with the first image frame, with FET_{max}=2.0 in low-grade, and 3.2 in high-grade tumours. Similar results were obtained when the analysis was applied to astrocytic tumours. These preliminary findings were supported by other studies that confirmed difference in uptake kinetics of brain tumours according to tumour grading.

Figure 1.7 is taken from the work by Pöpperl *et al.* [53]. It shows two representative examples of a low-grade and a high-grade tumour, and their kinetics. As shown in the plots, the low-grade glioma TAC is constantly increasing over acquisition time, while the high-grade TAC shows an early peak, followed by a decrease in uptake. Thus, dynamic FET PET can be considered as a useful tool for identifying malignant brain lesions, since it appears that high and low-grade brain tumours exhibit different uptake kinetics of FET.

In a following study by the same authors, the diagnostic value of FET in recurrent gliomas was evaluated [11]. 53 patients with glioma and clinically suspected recurrence underwent FET PET scans 4 to 180 months after different treatment modalities. 43 of those patients initially had high-grade gliomas, while the remaining 10 had low-grade gliomas. For semiquantitative evaluation, maximum SUV and mean SUV within 80% and 70% isocontour thresholds were evaluated and the respective ratios to the background were calculated. PET results were correlated with MRI/CT, clinical follow-up or biopsy findings. The results showed that all 42 patients with confirmed recurrent tumours had focally increased FET uptake, whereas only low, homogeneous FET uptake was seen at the margins of the resection cavity in the 11 patients with no signs of clinical recurrence, thus demonstrating that FET PET reliably distinguishes between post-therapeutic benign lesions and tumour recurrence.

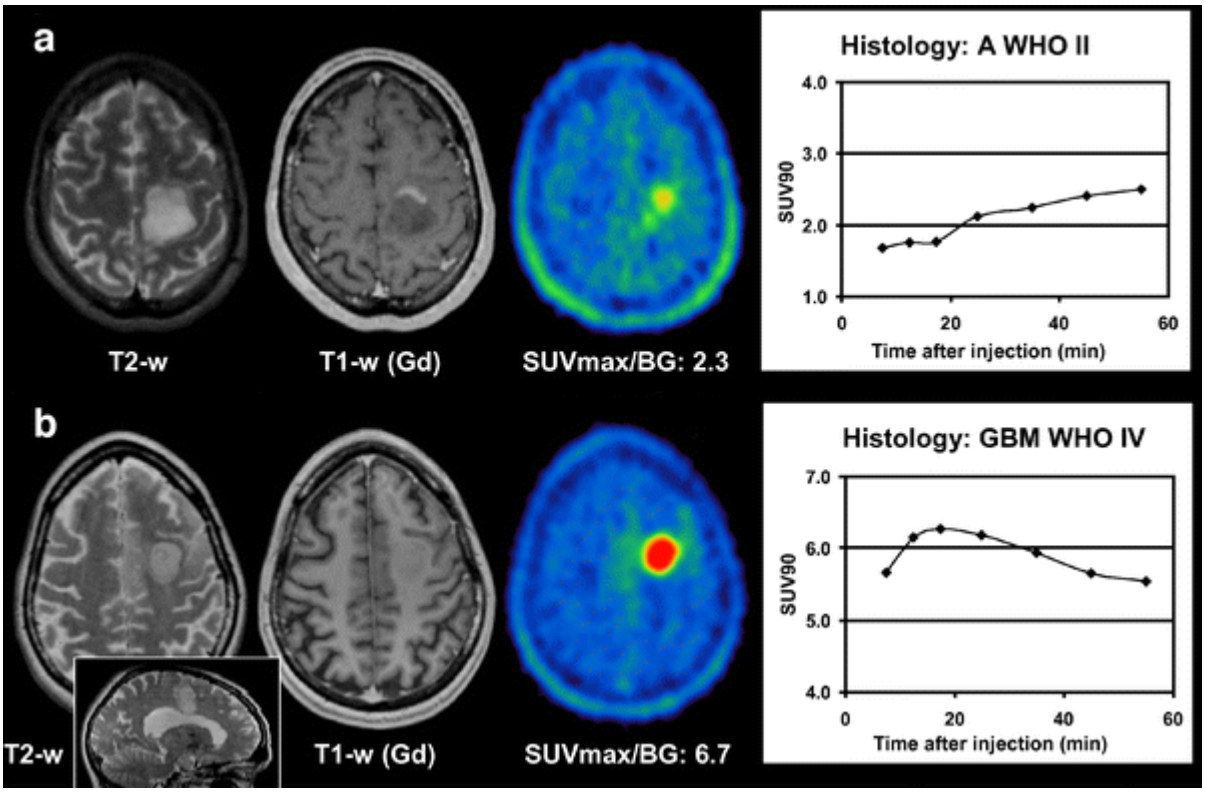

Figure 1.7 - Examples of a) low-grade tumour and b) high-grade tumour. Both studies show circumscribed hypertense lesions in T2-weighted MRI with pathologic contrast enhancement. In the low-grade tumour, some of the regions show contrast enhancement in T1-weighted MRI. MR diagnosis was pseudotumoral multiple sclerosis plaque in b), due to the irradiation of the corpus callosum, shown in the inset sagittal view. Dynamic evaluation shows increasing SUV90 values until the end of acquisition. On the other hand, for the high-grade tumour, dynamic evaluation shows an early peak with decreasing SUV90 values until the end of acquisition (adapted from [53]).

Another study by Pöpperl *et al.* [54] evaluated the potential of dynamic FET PET for non-invasive tumour grading in untreated patients. Dynamic FET PET studies were performed in 54 patients who, based on MRI, were estimated to have low-grade, intermediate or high-grade tumours. For standard evaluation, tumour maximum standardized uptake values (SUV) and the ratio to the background were calculated. For dynamic evaluation, mean SUV values within a 90% isocontour ROI and the ratio to the background were determined for each time frame. Results were correlated with histopathological findings. Histology revealed gliomas in all patients. The results showed a statistically significant difference in FET uptake in low- and high-grade gliomas. High interindividual variability in FET uptake, however, made it impossible to reliably predict tumour grading on an individual level. In contrast, due to their different FET kinetic uptake behaviours, low- and high-grade gliomas could be distinguished with high diagnostic power: analysis of dynamic data showed a sensitivity of 94% and a specificity of 100%. Thus, for non-invasive tumour grading of primary gliomas the standard method should be supplemented by the dynamic approach.

Several quantitative measures of dynamic FET PET imaging of patients with resected glioblastoma were evaluated [55]. Additionally, the prognostic value of these measures was assessed for a small patient population. Dynamic FET PET data of nine patients with histologically confirmed glioblastoma were acquired. The authors also computed maximum and average SUV on the tumour ROI, and the ratios of these SUVs to the background in order to quantify FET uptake and kinetics. Distribution volume ratio (DVR), weighted frame differences and compartment model parameters were used as well. For graphical analysis, Logan plots were chosen. It was found that several measures allowed robust quantification. SUV and distribution volume ratio did not correlate with clinical

outcome, while measures that are based on a background region highly correlated with disease-free survival, but not overall survival. Some advanced measures also showed a prognostic value but no improvement over the simpler methods. The authors concluded that FET PET probably has a prognostic value in patients with resected glioblastoma, but recognise the need of confirming such findings in a larger patient group.

Another study by Galldiks *et al.* [56] aimed to investigate the potential of dynamic FET PET for differentiating local recurrent brain metastasis from radiation necrosis after radiation therapy. The improvement in the treatment of solid tumours has led to an increasing number of patients who experience brain metastasis during the course of the disease. Stereotactic radiosurgery (SRC) and whole-brain radiation therapy (WBRT) are commonly used to treat brain metastases, and a growing percentage of patients live long enough to experience a local relapse of these metastases. Contrast-enhanced MRI is the method of choice for the evaluation of metastatic brain tumours. However, in many patients the differentiation of local recurrent brain metastasis from radiation necrosis after radiotherapy using contrast-enhanced MRI is difficult [57]. PET using FDG has been considered for the evaluation of these tumours, but the high physiologic glucose uptake of metastatic brain lesions limits its use.

In the referred study, 31 patients with single or multiple contrast-enhancing brain lesions on MRI after radiation therapy of brain metastases were investigated with dynamic FET PET. Maximum and mean tumour-to-brain ratios (TBR_{max} and TBR_{mean}) of FET uptake were determined. TACs were generated and time to peak (TTP) was calculated. In addition, TACs of each lesion were assigned to one of the following curve patterns: I) constantly increased FET uptake, II) FET uptake peaking early (TTP$\leq$20 min) followed by a plateau, and III) F-FET uptake peaking early, followed by a constant descent. Figure 1.8 depicts the difference between these patterns by showing TACs of three different patients. Both TBR_{max} and TBR_{mean} were significantly higher in patients with recurring metastasis than in patients with radiation necrosis. The diagnostic accuracy of FET PET for the correct identification of recurrent brain metastasis reached 78% using TBR_{max}, and 92% for curve patterns II and III versus curve pattern I. The highest accuracy (93%) to diagnose local recurrent metastasis was obtained when both a TBR_{mean} greater than 1.9 and curve pattern II or III were present. These finding suggest that the TBR_{mean} and results of kinetic studies in FET PET can differentiate local recurrent brain metastasis from radiation necrosis with a high sensitivity and specificity, thus contributing significantly to the management of patients with brain metastases. Moreover, when the data acquired was compared with the results using ^{11}C-methionine PET the difference between cut-off values can not only be related to methodological differences, but also exist due to the differences in the metabolic properties of the two amino acids. Thus, FET compared with ^{11}C-methionine shows both considerable logistic advantages but also improved accuracy in differentiating local recurrent brain metastasis from radionecrosis.

1.6.Motivation

According to the WHO, the worldwide incidence rate of all malignant and non-malignant brain and other CNS tumours in 2012 was 3.4 cases per 100,000 for a total count of 256,213 incident tumours [58]. MRI is the current gold standard for patients with neurological symptoms providing excellent anatomic detail. However, due to the typical heterogeneity of brain tumours, MRI-guided stereostatic biopsy is sometimes unable to evaluate tumour grading [48]. As mentioned in previous sections, accurate grading is important for directing the therapeutic approach and accessing the prognosis of glioma patients. In the past years, FET PET has become an important tool in brain tumour detection and diagnosis. Since the differences in uptake kinetics between low-grade and high-grade tumours seem to

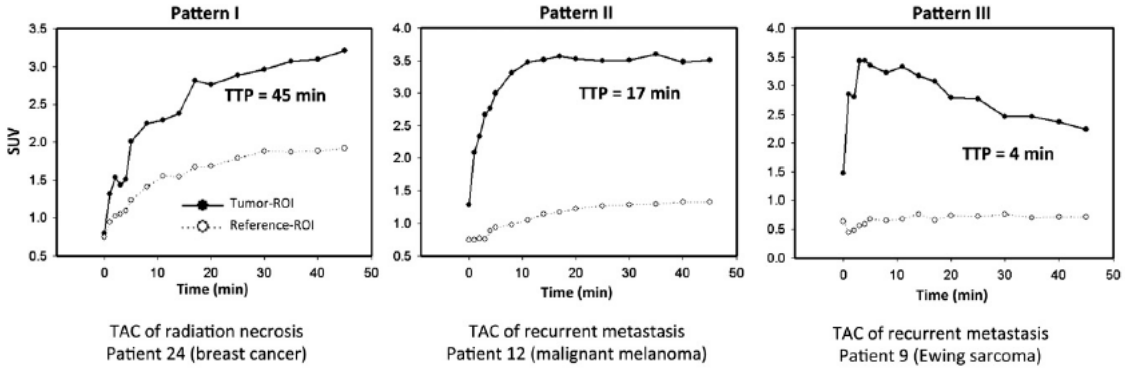

Figure 1.8 - Examples of kinetics of radiation necrosis (pattern I) and recurrent brain metastasis (patterns II and III). Dynamic evaluation of patient 24 shows constantly increasing FET uptake until the end of acquisition. Dynamic evaluation of patient 12 shows early peak of FET uptake, followed by stable uptake until end of acquisition. Dynamic evaluation of patient 9 shows early peak of FET uptake followed by constant decline of uptake until end of acquisition. (adapted from [56]).

be specific for FET [59], FET curve fitting could offer a possibility of developing non-invasive diagnostic alternatives. Hence, the aim of this work was to develop simple method to generate parametric images of FET reflecting tumor grade. Preliminary work on modeling FET curves was already performed [60], and in previous studies parametric images were generated using linear regression methods. Here we aimed for a more accurate curve fitting, so a nonlinear regression method was used to generate the parametric images.

2. Methods

2.1.Patients

Eleven patients (3 female, 8 male, age: 45±15 years) with untreated primary brain tumours and histopathologic confirmation were included in the study. Six patients had high-grade gliomas, while the remaining 5 were diagnosed with low-grade gliomas. The selection of patients in this study was based on the challenge to improve diagnostic information about cerebral lesions in which classification based on kinetic profile was unclear. More detailed information on the patients is given on **Erro! A origem da referência não foi encontrada.**.

Table 2.1 - Individual patient data including age, gender, weight, height, injected activity, and diagnosis after stereotactic byopsy.

Patient	Age (years)	Gender	Weight (kg)	Height (cm)	Injected Activity (MBq)	Diagnosis
HG020	50	M	90	185	264	High-grade
HG021	57	M	83	183	228	High-grade
HG417	63	F	69	165	251	High-grade
HG469	56	M	76	172	233	High-grade
HG512	30	M	110	170	267	High-grade
HG552	67	F	60	160	198	High-grade
LG090	36	M	75	172	278	Low-grade
LG131	30	M	105	180	293	Low-grade
LG247	26	M	78	180	238	Low-grade
LG465	25	F	53	160	182	Low-grade
LG598	57	M	83	174	198	Low-grade

2.2.Data acquisition, reconstruction, and motion correction

PET acquisition was done with the PET Insert of a hybrid Siemens 3T MR-BrainPET system. The human brain PET insert consists of 32 detector cassettes based on 10-µm copper shielded boards arranged in a ring geometry. Each detector cassette houses six PET block detectors aligned in the axial direction of the device with a gap of 2.25 mm between the block, yielding a 32 cm transaxial and 19.1 cm axial field of view (FOV). A block detector consists of 144 LSO crystals with an individual crystal size of 2.5×2.5×20 mm^3. The stacked 12×12 crystal block is read by a 3×3 array of single avalanche photodiodes (APDs) with an active surface of 5×5 mm^2. The average energy resolution of the PET detectors is 17.1±0.7% (full width half maximum, FWHM) [61]. The radiochemical yield of the tracer was about 60-65% at a radiochemical purity>98%. The tracer was administered as isotonic neutral solution.

An additional MR measurement was performed before standard PET protocol. FET was intravenously injected and a list mode acquisition over 60 minutes was performed. List mode data was stored into 16 time frames with 5 × 1 min, 5 × 3 min and 6 × 5 min. After Fourier rebinning, template based MR based Attenuation Correction (MRAC) [62] was performed, followed by random and scattered coincidences and decay correction. The resulting 153 image planes of 256×256 voxels were iteratively reconstructed (OSEM, 2 subsets, 32 iterations) using the ECAT 7.2 software. Later, a 3D-Gaussian filter with FWHM=2.5 was applied. Motion correction of the dynamic frames was performed

with the Fusion tool of the software package PMOD. These data processing steps are schematized in Figure 2.1.

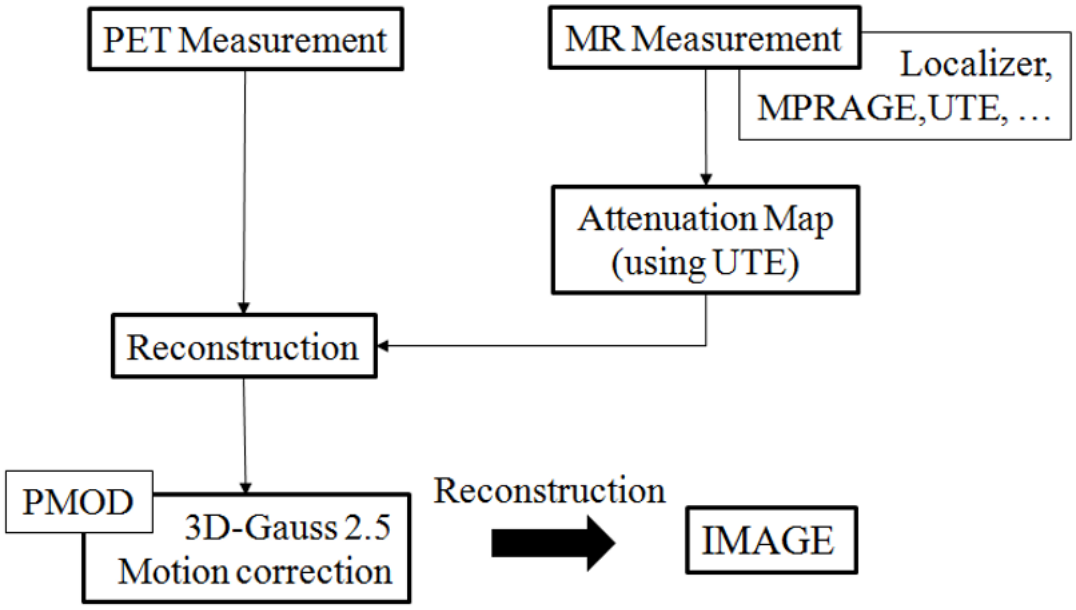

Figure 2.1 - FET PET Workflow.

2.3. Tumour segmentation

The dynamic PET images used in this work were imported to Wolfram Mathematica [64] (see Appendix I), which was the software used to perform the fitting and to generate the parametric images. In order to fit just the tumour volume, excluding as many voxels containing healthy tissue as possible, a segmentation procedure had to be applied (see Appendix II). After being imported, each image was multiplied by a binary mask. The masks were produced by setting all voxel SUVs below a previously calculated threshold to zero and all values above or equal to this threshold to 1. For each dynamic image, a different threshold was estimated according to Equation 2.1.

$$Threshold = 1.6 \times \frac{1}{n_{voxels}} \sum_{i=1}^{n_{voxels}} SUV_i \qquad (\mathbf{2.1})$$

Equation 2.1 was applied to the sum images. Based on a previous biopsy-controlled study [48], tumour borders were defined by a lesion-to-brain ratio greater than the threshold of 1.6, as defined by Equation 2.1. The ratio was then multiplied by the mean SUVs of a manually selected healthy brain region. For all cases, this healthy region was located in the brain hemisphere opposite to the one containing the tumour volume, and included similar ratios of gray matter and white matter, but no cerebrospinal fluid (CSF). It was not required that selected control region was exactly symmetrical to the tumour. Also, because the size of the control region over which the threshold was computed has no impact on the estimated threshold, some control regions were larger than others. Table 2.2 resumes the estimated thresholds for each image.

Table 2.2 - Estimated segmentation thresholds**.**

Patient	Estimated Threshold
HG020	3.69
HG021	3.12
HG417	4.03
HG469	4.96
HG512	2.67
HG552	7.21
LG090	4.68
LG131	4.81
LG247	3.65
LG465	2.68
LG598	2.48

After segmenting the tumour, all tumour voxels were masked. The fitting procedures described in Section 2.6 were applied to the masked data. From now on, this data will be referred to as Segmented Tumour Volume (STV).

2.4. Linear model

Linear regression is an approach for modelling the relationship between a scalar dependent variable, and one or more explanatory variables. A simple regression equation has on the right hand side an intercept and an explanatory variable with a slope coefficient. Because of its simplicity and robustness, linear regression is used extensively in practical applications. Models which depend linearly on their unknown parameters are easier to fit than models which are non-linearly related to their parameters. Linear regression models are often fitted using the least squares approach [65]. There is an explicit solution to the least square fit approach, which makes it possible to compute a formula for the intercept and the slope independent of the data. As a result, no iterative procedure is required, unlike gradient ascend methods, where projections may fall very far from the real solution.

In this work, linear regression with straight line equation model (Equation 2.2) was used for fitting:

$$C_{FET}(t) = mt + y \qquad (\mathbf{2.2})$$

$C_{FET}(t)$ denotes the concentration of the tracer in the tissue at a given time after injection, t. The two parameters assessed by this model are the slope, m, and the intercept, y.

2.5. Empirical nonlinear models

The basic idea of nonlinear regression is the same as that of linear regression. Nonlinear regression is characterized by the fact that the prediction equation depends nonlinearly on one or more unknown parameters [66]. While linear regression is often used for building a purely empirical model, nonlinear regression usually arises when there are physical reasons for believing that the relationship

between the response and the predictors follows a particular functional form. As mentioned in previous sections, in the case of FET PET TAC, the response is clearly not linear. Nonlinear regression models are expected to be better suited for data fitting when linear dependence is not expected.

In this work, three exponentially damped linear models were selected for analysis. The first model is described by Equation 2.3. It consists of a simple 2-parameter linear model multiplied by an exponential factor:

$$C_{FET}(t) = At\, e^{-\kappa t} \qquad (\mathbf{2.3})$$

where $C_{FET}(t)$ denotes the concentration of the tracer in the tissue at a given time after injection, t; A expresses the amplitude of the uptake in the region or voxel where the fit is being applied, and κ describes the shape of the curve. The linear part of the model, t, assures that the model starts at 0 for $t = 0$, as it is expected for the tracer. At time 0, no tracer can be trapped inside the cells. The exponential part limits the linear rise of t for small κ (for $\kappa = 0$ we would have just a linear model), or converts into falling TAC after some time (for large κ). The latter effect always happens, except for $\kappa = 0$. In case of very small κ, the curve eventually falls after some time. In Figure 2.2, the model was plotted with the same A value ($A = 16$), but different κ values. When the model is plotted with a low κ value, the resulting curve resembles the TAC from a high-grade glioma, whereas a higher κ seems to reproduce a curve shape similar to the TAC of a low-grade glioma.

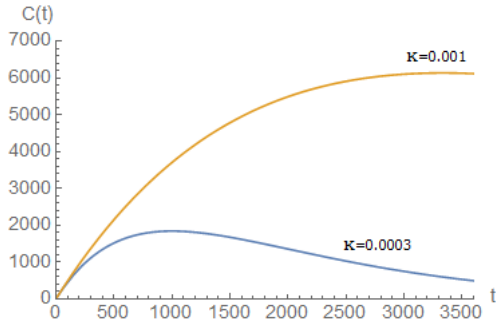

Figure 2.2 - Exponentially damped linear model with low κ value (blue line) and high κ value (orange line).

A second model, derived from the first one, was also studied. This new model adds a third parameter to the previous one. This new parameter is meant to describe an offset seen in the measured TACs. It was introduced as an approach to use all data frames, instead of dropping the first 2. The 3-parameter model is described by Equation 2.4,

$$C_{FET}(t) = Ate^{-\kappa t} + c \qquad (\mathbf{2.4})$$

Like in the previous model, here $C_{FET}(t)$ denotes the concentration of the tracer in the tissue at a given time t after injection, $t = 0$. Parameter A expresses the amplitude of the uptake in the region or voxel where the fit is being applied, and κ describes the shape of the curve. The extra parameter c determines the offset of the curve. Figure 2.3 shows the 3-parameter model plotted with the same conditions as in Figure 2.2, but with the added c parameter set to 500.

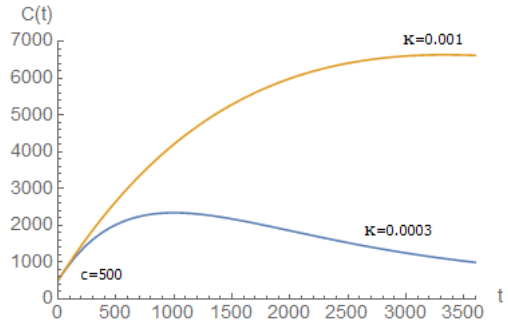

Figure 2.3 - Exponentially damped linear model with an offset plotted with and low κ value (blue line), and high κ value (orange line), for an offset c=500.

A third model was included in the nonlinear regression model fits. As the previous ones, this new model is an exponential damped linear model, but with a square-root time dependence, as described by Equation 2.5.

$$C_{FET}(t) = A\sqrt{t}\,e^{-\kappa\sqrt{t}} \qquad (\mathbf{2.5})$$

As before, $C_{FET}(t)$ denotes the concentration of the tracer in the tissue at a given time t after injection, $t = 0$, A expresses the amplitude of the uptake in the region or voxel where the fit is being applied, and κ describes the shape of the curve. The difference here is in the added time dependence. Figure 2.4 shows how this model behaves when different parameters are used.

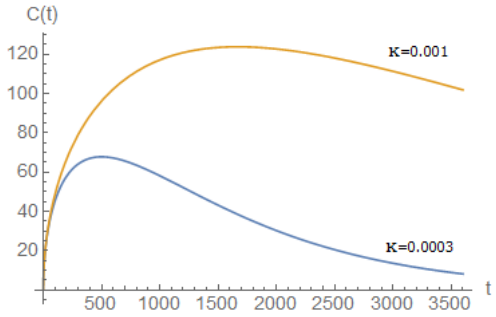

Figure 2.4 - Exponentially damped model with square-root time dependence: model behaviour with low κ value (blue line), and high κ value (orange line).

From the 3 nonlinear regression models, only the exponentially damped model with square-root time dependence is presented for the STV fits. The remaining two models were also tested, but the third model yielded the best results in all 11 cases. The linear regression model was also fitted to all STVs for comparison (see Appendix II).

2.6. Fitting of Tumour TAC

After segmentation, the mean TAC of the STVs was calculated. Linear and nonlinear regression were used to fit the TAC of each volume. In both cases, the first minutes of acquisition were left out of the analysis. When performing the fitting with the linear model, the first 5 minutes of acquisition were

discarded, i.e., the linear regression was fitted to the time-activity data from 5 to 60 minutes after injection of FET. For the nonlinear regression, the fitting was applied to the time-activity data from 2 to 60 minutes after injection. The reason behind it is that in the minutes immediately after injection, the tracer is still being transported to the brain. Figure 2.5 shows the first five frames of one of the dynamic PET scans used in this work. In the first frame, the tumour is almost not visible. Instead, the tracer seems to be concentrated in a small area in the posterior part of the brain. That signal is coming from the blood vessels, where the tracer is still highly concentrated, and being carried to the brain. As time goes by, and the tracer leaves the blood stream, the signal from the artery and veins becomes weaker, whereas the tumour uptake starts to increase. Here, the fit models that were looked for were designed to model the uptake in the tissue, but not the decrease of concentration in blood. The latter is not possible with only few parameters. Obviously, the tumour is vascularized, and therefore also shows activity contained in the blood pool, which is very elevated at the start of the measurement, but cannot be modelled with simple models.

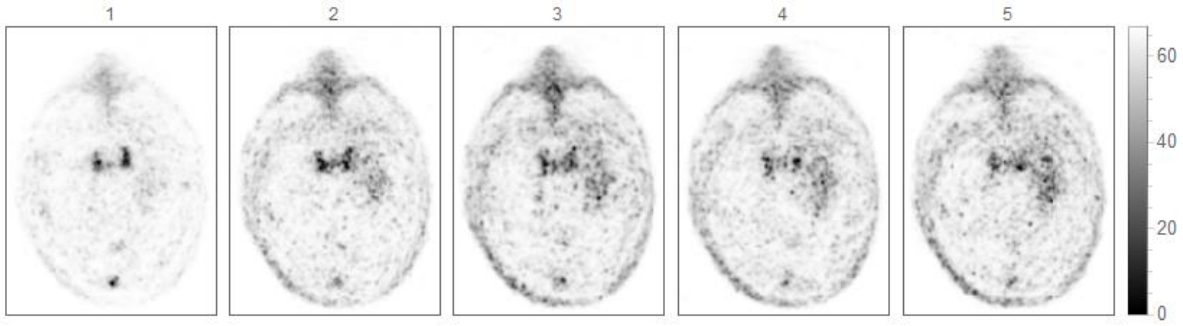

Figure 2.5 - First 5 frames of a dynamic FET PET scan (one minute each).

The difference between the data that is dropped when performing linear regression versus the data that is left out the nonlinear regression fit arises from the typical shape of the TACs, and how well the models are expected to reproduce its behaviour. Typically, tumour TACs are not linear. As explained in previous sections, in the case of the high-grade glioma, FET uptake is expected to decrease after an early peak. A linear model would fail to reproduce such a curve, with the fit becoming less accurate as more data before peak is included. The option of leaving out the first five minutes of acquisition comes from previous works on FET kinetics analysis using linear regression [60]. As the nonlinear regression was expected to better reproduce the TAC shape, including the data before peak, only the first 2 minutes of acquisition were discarded, where it was supposed that most of the tracer is still dissolved in the blood.

After fitting the STV, the mean values of the parameters for the low-grade glioma and high-grade glioma groups were calculated. To better evaluate the differences between the two groups, a 2-sided Mann-Whitney U test was performed ($\alpha = 0.05$).

2.7.Parametric images

Parametric images of A and κ were calculated based on nonlinear regression fitting of FET data in each voxel. First, only the parametric images of a manually selected tridimensional area containing the tumour were generated. The three nonlinear models described in the previous section were tested. For the exponentially damped linear model with offset, parametric images of the offset parameter c were not produced. For comparison, parametric images of slope and intercept parameters from the linear regression model were also calculated. However, because of the long computation times (about 3 to 4

hours per image volume), only whole-head parametric images based on the exponentially damped linear model with square-root time dependence were generated. The fitting was performed on a multicore machine, using 10 cores in parallel. This model was selected after analysing the first set of parametric images, where it proved to be the most capable of reproducing FET kinetics. Images of the coefficient of determination (R^2) were generated for all cases in order to assess the quality of fit. The source code used for these calculations is presented in Appendix III.

3. Results

3.1.Fits applied to segmented tumour volume

The results from tumour segmentation and from the fits applied to the STV are shown here. Figure 3.1 shows the mask for high-grade glioma HG020 created to select the tumour region where uptake was averaged over time, and fitting with linear regression and nonlinear regression models was applied.

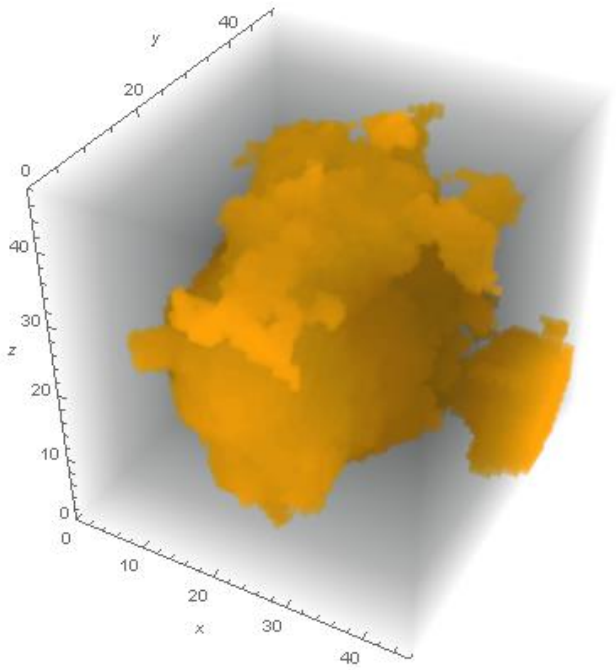

Figure 3.1 - 3D mask used for HG020 segmentation.

The results of the fitting procedure are shown below, in Figure 3.2. The blue dots correspond to the averaged SUVs of the voxels within the segmented tumour volume, and the red line is the fitted model. The fitting with linear regression model returned a slope of $m = 0.0007 \pm 0.0001$, and an intercept value of $y = 5.0 \pm 0.2$. On the other hand, parameters extracted from the nonlinear regression model fit were $A = 0.359 \pm 0.006$, and $\kappa = 0.0202 \pm 0.0004$. The values of R^2 were calculated to assess quality of fit. The linear model fit yielded an R^2 value of 0.78, while for the nonlinear model, $R^2 = 0.99$.

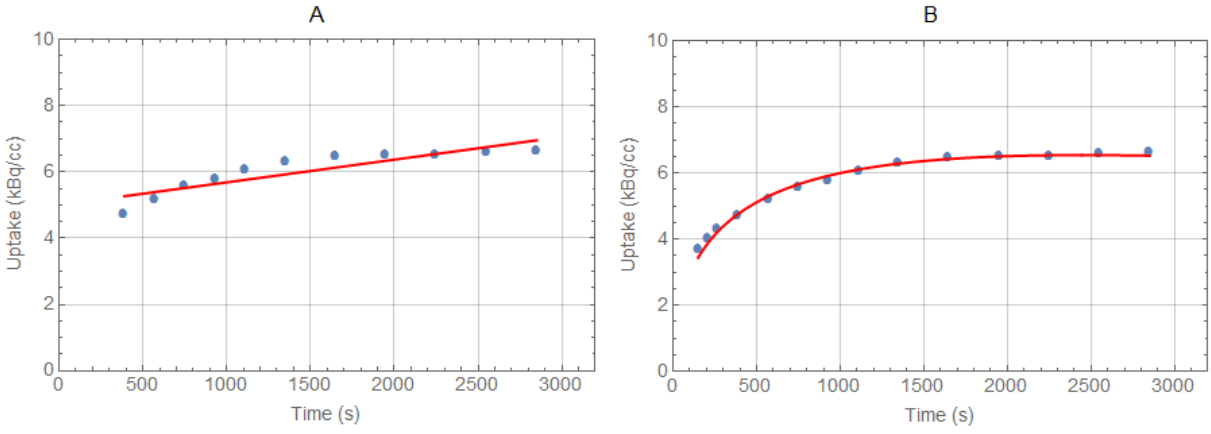

Figure 3.2 - Fits applied to mean TAC of STV for HG020**.** A) Linear model; B) Exponentially damped linear model with square root time dependence.

In Figure 3.3, the mask used for the segmentation of tumour HG021 is depicted. Figure 3.4 presents the results of the linear and nonlinear model fits. The intercept value returned from the linear fit was $y = 5.22 \pm 0.08$, with a slope of $m = -0.00034 \pm 0.00005$. With the nonlinear regression model fit, the returned parameters were $A = 0.52 \pm 0.02$, and $\kappa = 0.037 \pm 0.001$. R^2 value for the linear fit was of 0.86, and for the nonlinear fit $R^2 = 0.99$.

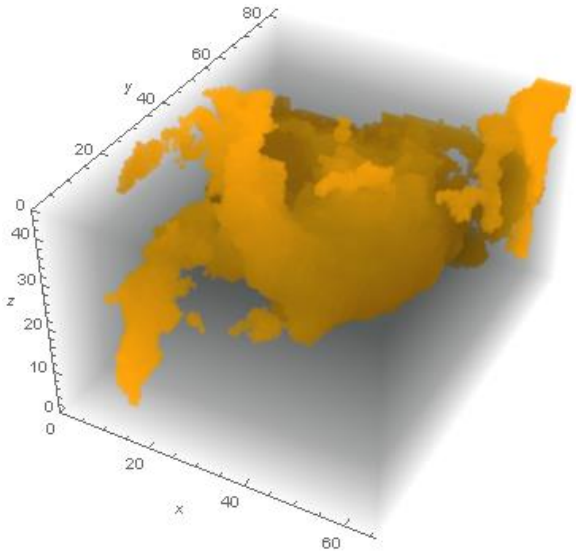

Figure 3.3 - 3D mask used for HG021 segmentation.

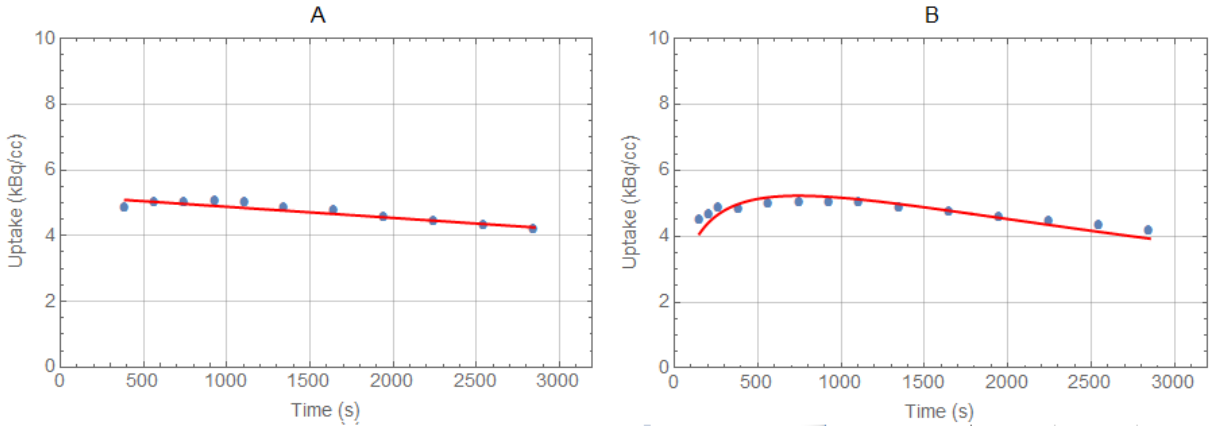

Figure 3.4 - Fits applied to mean TAC of STV for HG021. A) Linear model; B) Exponentially damped linear model with square root time dependence.

Figure 3.5 shows the mask used for the segmentation of tumour LG090. The linear regression model fit returned intercept and slope values of $y = 6.05832 \pm 0.00009$, and $m = 0.2157 \pm 0.0001$, while with the nonlinear regression model fit, the estimated parameters were $A = 0.46 \pm 0.02$ and $\kappa = 0.026 \pm 0.001$. The R^2 values associated with the fits were $R^2 = 0.05$ and $R^2 = 0.99$, respectively. The fits, as well as the TAC are shown in Figure 3.6. The fluctuation seen in the TAC is due to the low count of tumour voxels.

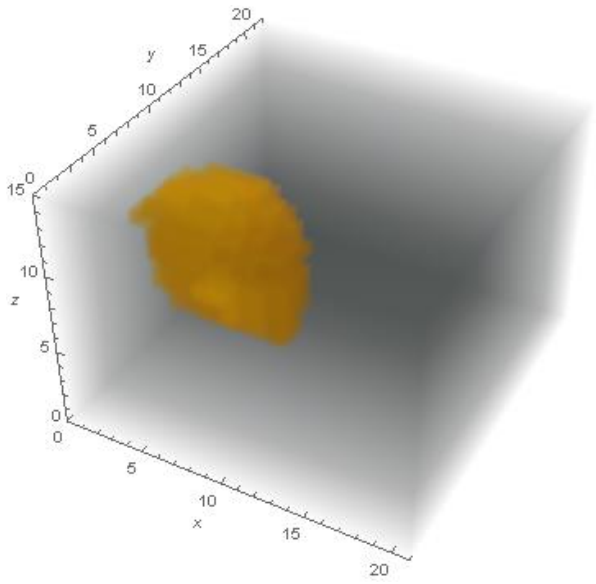

Figure 3.5 - 3D mask used for LG090 segmentation.

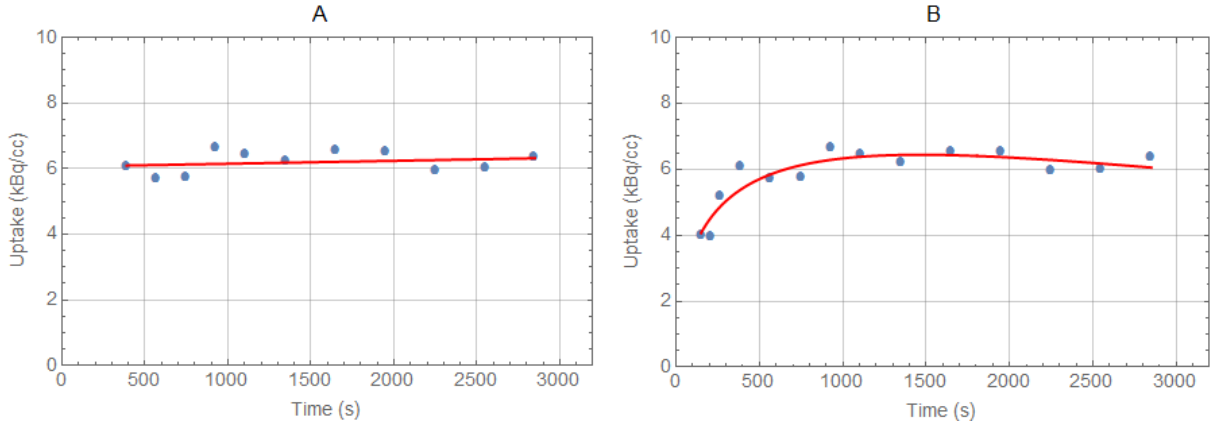

Figure 3.6 - Fits applied to mean TAC of STV for LG090. A) Linear model; B) Exponentially damped linear model with square root time dependence.

Figure 3.7 shows the mask obtained for image LG131 segmentation. Unlike the previous masks, this one does not present a single, unified tumour mass. On the contrary, judging by the appearance of this mask, the tumour seems to be scattered, and mixed with healthy tissue.

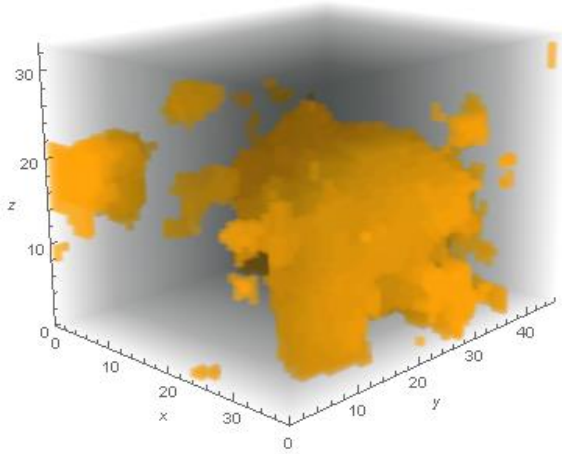

Figure 3.7 - 3D mask used for LG131 segmentation.

The results of the fits performed on the segmented tumour from LG131 are shown in Figure 3.8. Intercept and slope values obtained from the linear regression model fit were $y = 5.2 \pm 0.3$, and $m = 0.0012 \pm 0.0002$, with $R^2 = 0.88$. The amplitude and curve shape parameters returned from the nonlinear regression model fit were $A = 0.340 \pm 0.005$, and $\kappa = 0.0150 \pm 0.0004$, with $R^2 = 0.99$.

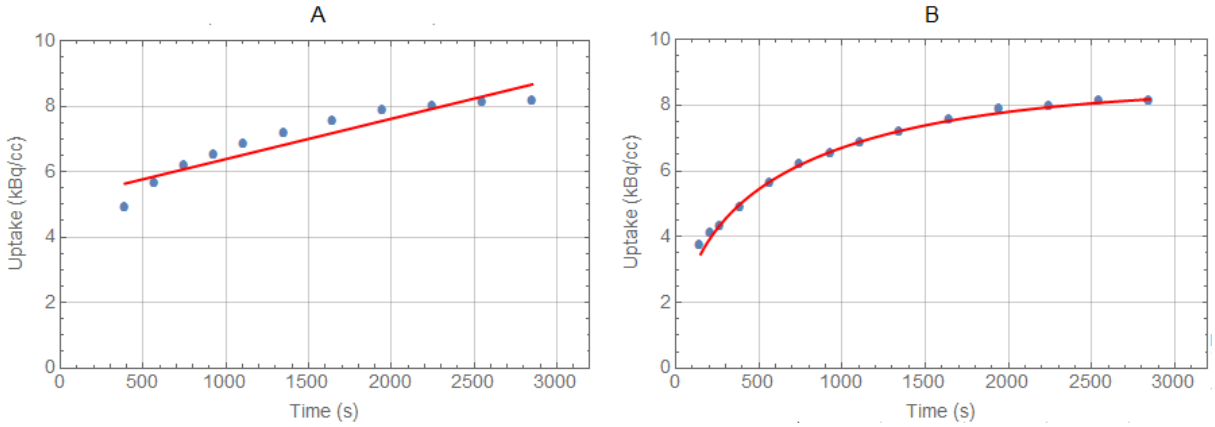

Figure 3.8 - Fits applied to mean TAC of STV for LG131. A) Linear model; B) Exponentially damped linear model with square root time dependence.

The mask estimated for image LG247 is presented in Figure 3.9. This mask is smaller than the others, which resulted in a noisy average TAC, as seen in Figure 3.10. The linear regression model fit was applied to the tumour, returning the intercept and slope parameters of $y = 2.6 \pm 0.3$ and $m = 0.0012 \pm 0.0002$, with a calculated R^2 of 0.82. The parameter values determined for the nonlinear regression model fit were $A = 0.21 \pm 0.03$, and $\kappa = 0.014 \pm 0.004$. Estimated R^2 value was 0.98. Both fits are presented in Figure 3.10 (red line). Like in the case of LG090, the low count of tumour voxels caused TAC fluctuations.

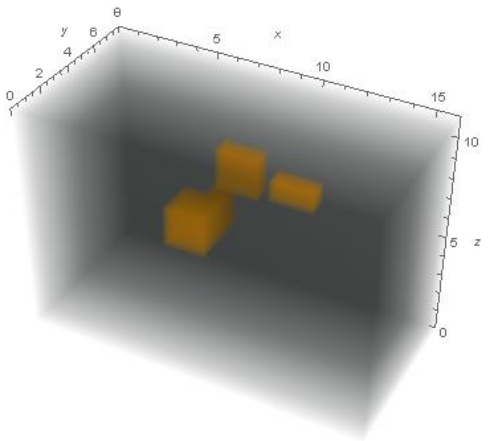

Figure 3.9 - 3D mask used for LG247 segmentation.

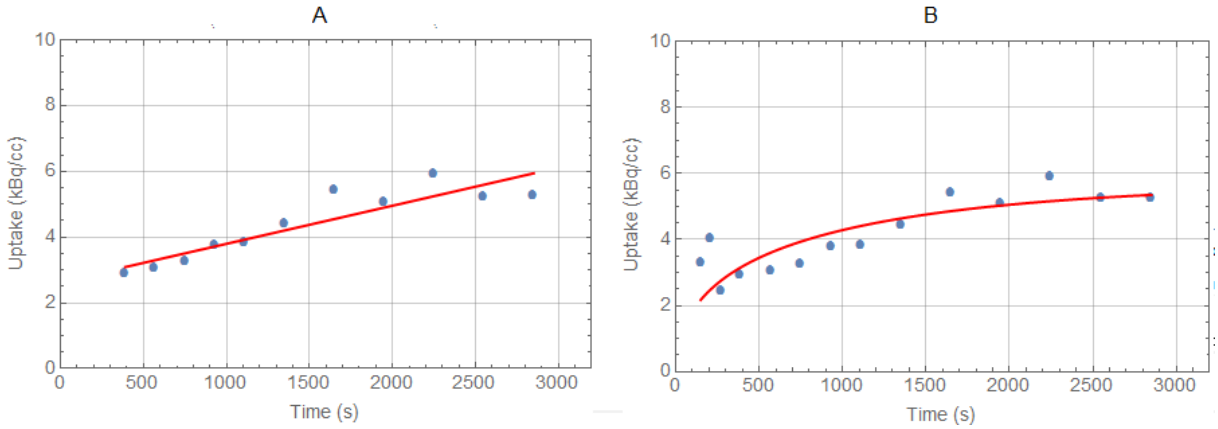

Figure 3.10 - Fits applied to mean TAC of STV for LG247. A) Linear model; B) Exponentially damped linear model with square root time dependence.

Figure 3.11 shows the mask for high-grade glioma HG417 created to select the tumour region. The fitting with linear regression model returned an intercept value of $y = 5.5 \pm 0.2$, and a slope of $m = 0.0005 \pm 0.0001$. On the other hand, with the nonlinear regression model fit, the retrieved values for amplitude and curve shape were $A = 0.405 \pm 0.006$, and $\kappa = 0.0226 \pm 0.0004$. The linear model fit yielded an R^2 value of 0.57, while for the nonlinear model, $R^2 = 0.99$. These results are depicted in Figure 3.12.

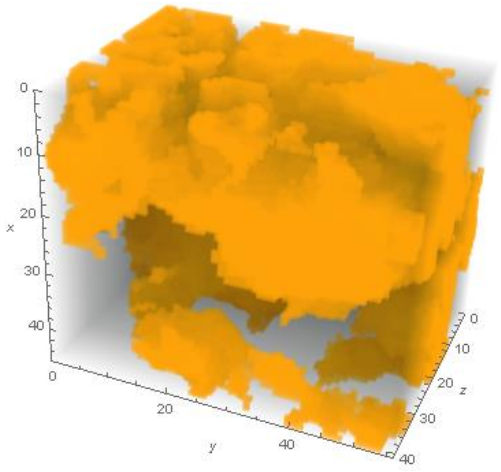

Figure 3.11 - 3D mask used for HG417 segmentation.

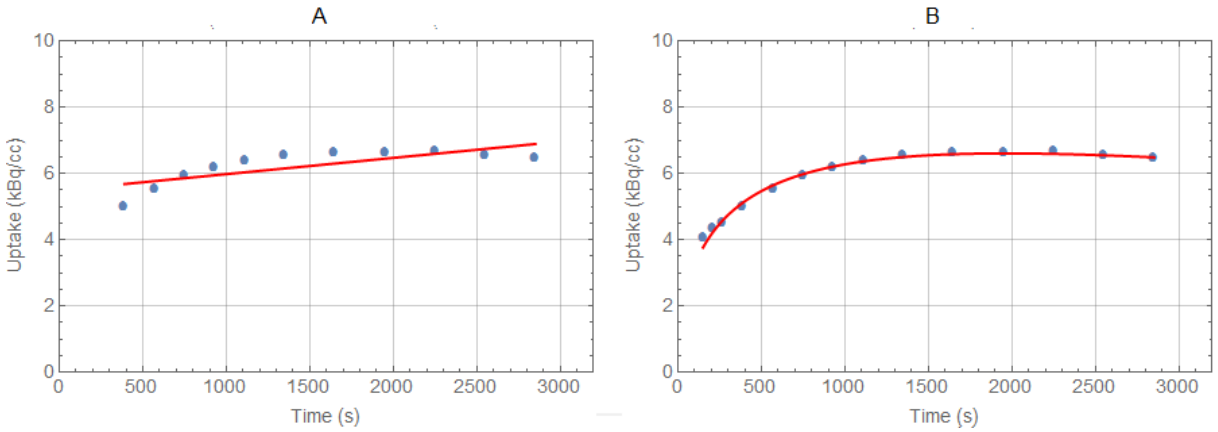

Figure 3.12 - Fits applied to mean TAC of STV for HG417. A) Linear model; B) Exponentially damped linear model with square root time dependence.

The mask used for tumour segmentation in image LG465 is shown below, in Figure 3.13.

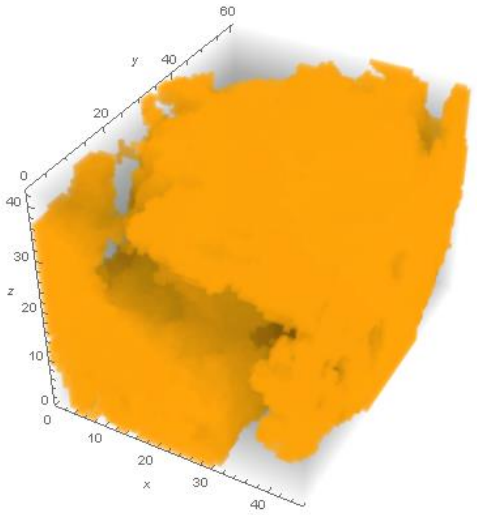

Figure 3.13 - 3D mask used for LG465 segmentation.

The fits applied to the averaged SUVs of the tumour volume are depicted in Figure 3.14. The linear regression model fit was performed with an estimated R^2 value of 0.92. The intercept and slope parameters were $y = 3.7 \pm 0.1$, and $m = 0.00076 \pm 0.00007$. For the nonlinear regression model fit, the calculated parameters were $A = 0.27 \pm 0.01$, and $\kappa = 0.018 \pm 0.001$. The R^2 value of the fit was 0.99.

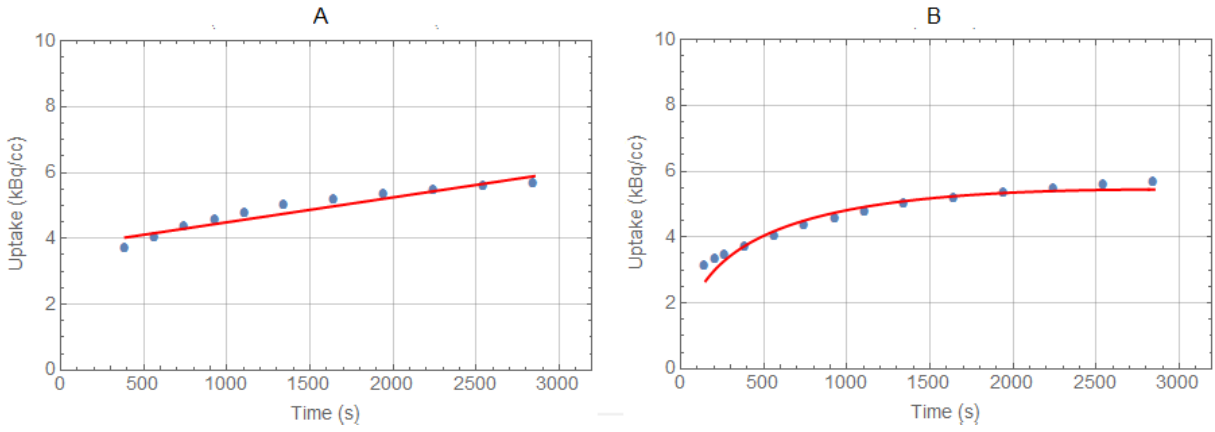

Figure 3.14 - Fits applied to mean TAC of STV for LG465. A) Linear model; B) Exponentially damped linear model with square root time dependence.

Figure 3.15 and Figure 3.16 show the results of the segmentation procedure applied to HG469, and the fits performed in the segmented tumour volume. An intercept value of $y = 6.3 \pm 0.2$, and a slope of $m = 0.0007 \pm 0.0001$ were calculated for the fitting using the linear regression model. The nonlinear regression model fit returned the parameter values of $A = 0.47 \pm 0.01$, and $\kappa = 0.0219 \pm 0.0006$. The estimated R^2 values were $R^2 = 0.77$ for the first fit, and $R^2 = 0.99$ for the second.

Figure 3.17 shows the mask generated for image HG512. Because the tumour volume is so close to the bone, and the segmentation procedure was based on a simple selection of voxel values based on a threshold, the resulting mask ended up containing not only the tumour region, but also bone. For that reason, a small area within the tumour was manually selected. The same fitting procedures were applied to this smaller area.

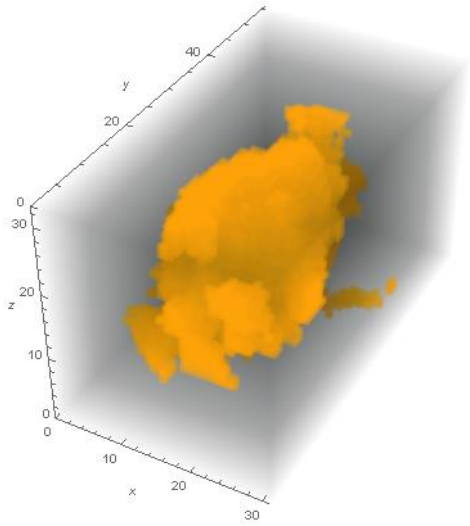

Figure 3.15 - 3D mask used for HG469 segmentation.

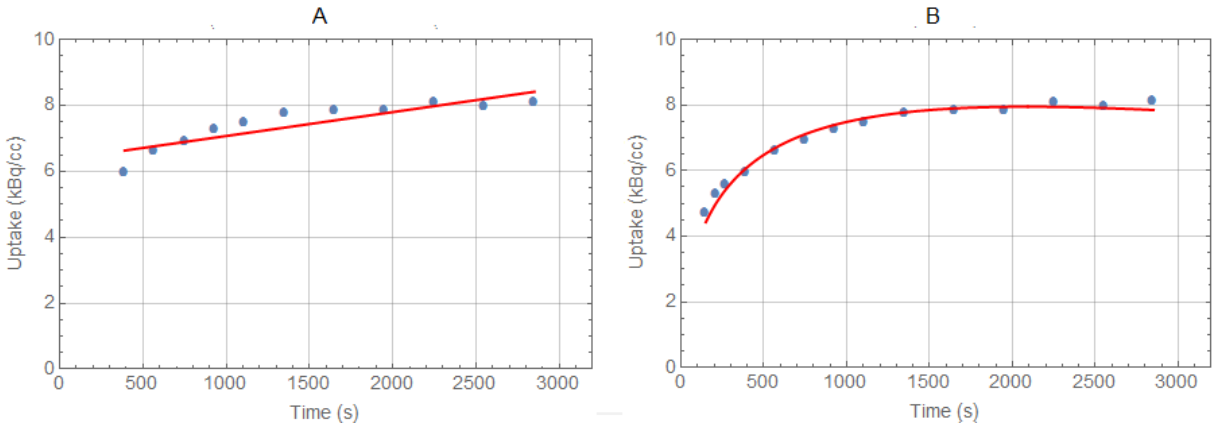

Figure 3.16 - Fits applied to mean TAC of STV for HG469. A) Linear model; B) Exponentially damped linear model with square root time dependence.

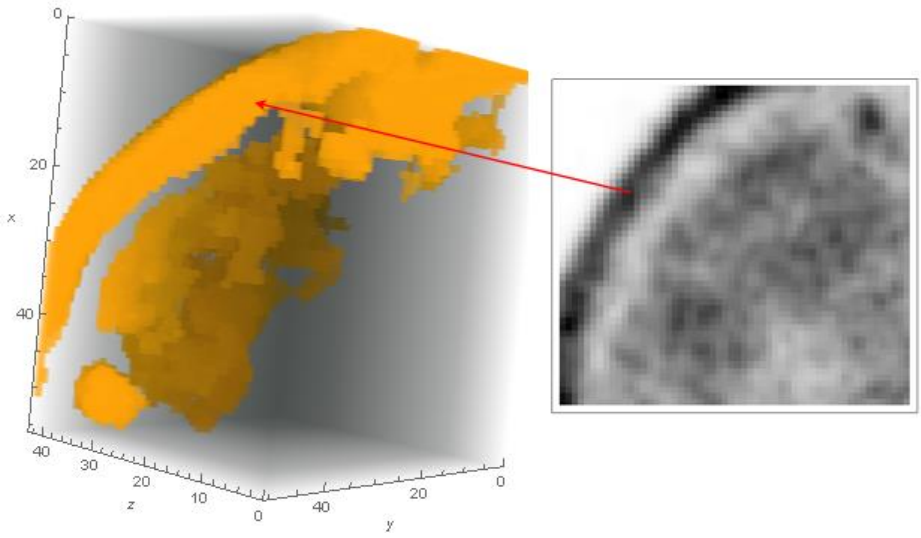

Figure 3.17 - 3D mask used for HG512 segmentation.

The results of the fits are presented in Figure 3.18. The intercept value returned by the linear regression model fit was $y = 2.4 \pm 0.1$, and the slope value was $m = 0.00068 \pm 0.00006$. For the nonlinear regression method, the calculated parameters were $A = 0.168 \pm 0.006$, and $\kappa = 0.0149 \pm 0.0009$. The R^2 values of the fits were $R^2 = 0.94$, and $R^2 = 0.99$, respectively.

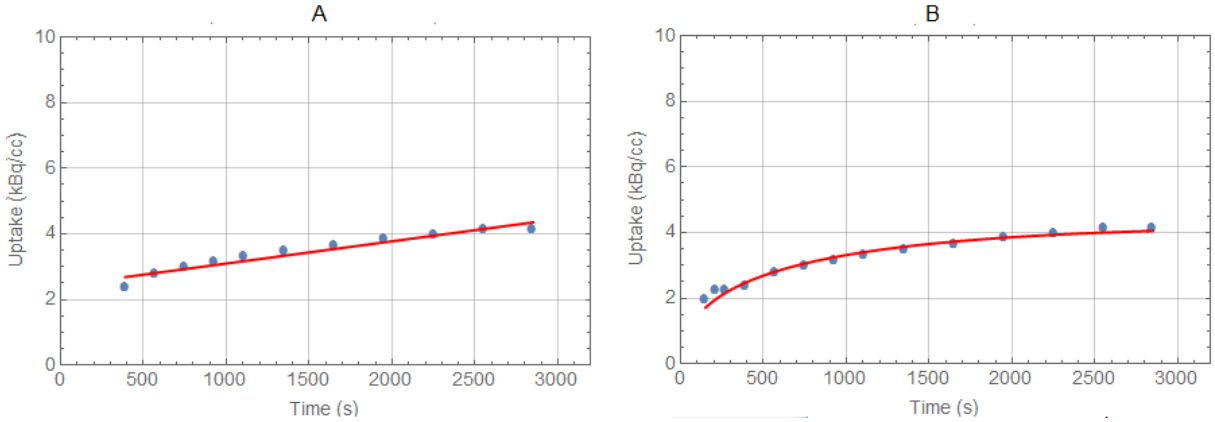

Figure 3.18 - Fits applied to mean TAC of STV for HG512. A) Linear model; B) Exponentially damped linear model with square root time dependence.

The mask generated for HG552 tumour segmentation is shown in Figure 3.19. The results of the fits performed on the segmented tumour from LG131 are shown in Figure 3.20. Intercept and slope values obtained from the linear regression model fit were $y = 11.3 \pm 0.3$, and $m = -0.0006 \pm 0.0002$, with $R^2 = 0.53$. The amplitude and curve shape parameters returned from the nonlinear regression model fit were $A = 0.976 \pm 0.009$, and $\kappa = 0.0325 \pm 0.0003$, with $R^2 = 0.99$.

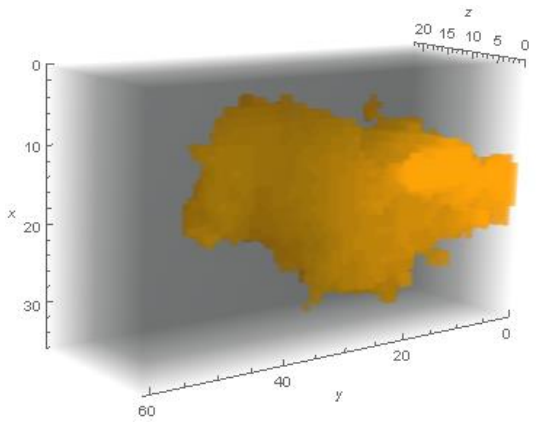

Figure 3.19 - 3D mask used for HG552 segmentation.

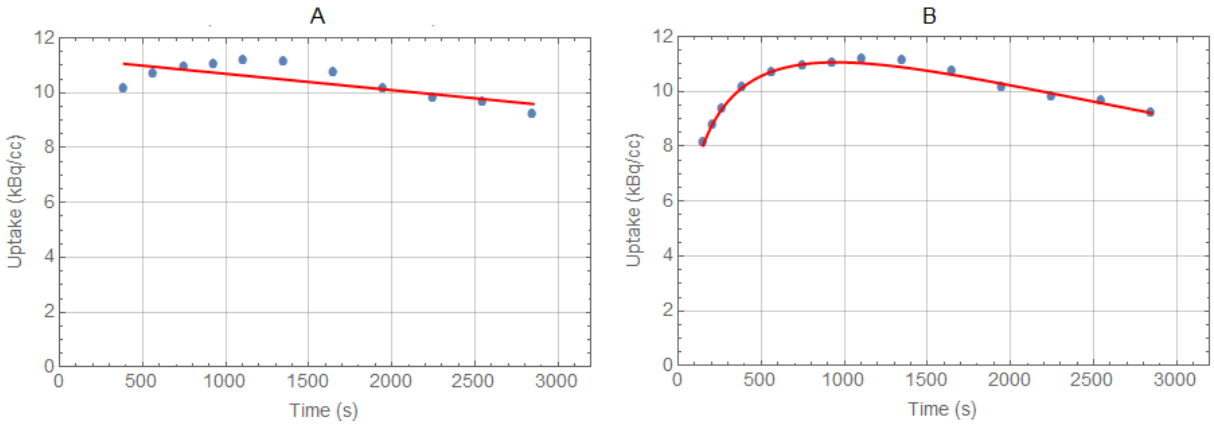

Figure 3.20 - Fits applied to mean TAC of STV for HG552. A) Linear model; B) Exponentially damped linear model with square root time dependence.

Lastly, Figure 3.21 shows the mask applied to the image HG598. The fits to the STV are presented in Figure 3.22. The intercept and slope parameters determined for the linear regression model fit were $y = 2.76 \pm 0.07$, and $m = 0.00024 \pm 0.00004$, respectively. For the nonlinear fit, the calculated parameters were $A = 0.23 \pm 0.01$, and $\kappa = 0.025 \pm 0.001$. The estimated R^2 values were $R^2 = 0.77$, and $R^2 = 0.99$ for the linear and nonlinear regression fits, respectively.

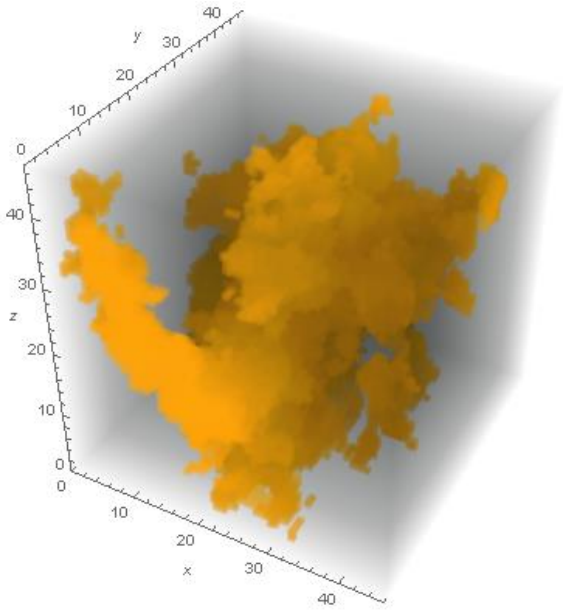

Figure 3.21 - 3D mask used for HG598 segmentation.

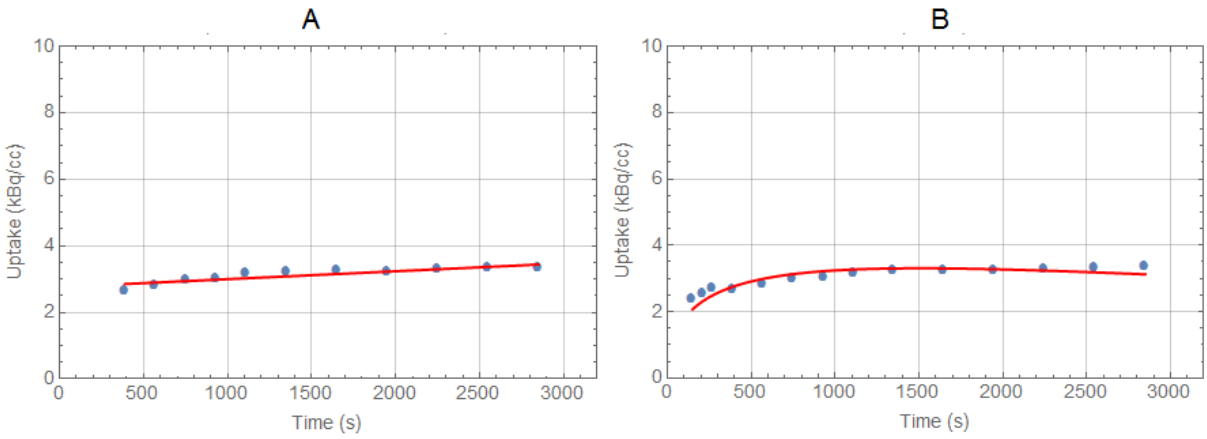

Figure 3.22 - Fits applied to mean TAC of STV for HG598. A) Linear model; B) Exponentially damped linear model with square root time dependence.

Table 3.1 presents a summary of the parameters calculated from the STVs fittings, as well as the dimensions of the masks used for tumour segmentation, i.e., the dimensions of the volumes where voxel SUVs were averaged.

Table 3.1 - Summary of the estimated parameters from linear and nonlinear regression model fit to the STVs.

Patient	Mask dimension (voxels)	LINEAR REGRESSION MODEL			NONLINEAR REGRESSION MODEL		
		Intercept	Slope	R^2	A	κ	R^2
HG020	112,608	5.0±0.2	0.0007±0.0001	0.78	0.359±0.006	0.0202±0.0004	1
HG021	251,988	5.22±0.08	-0.00034±0.00005	0.86	0.52±0.02	0.037±0.001	1
HG417	105,616	5.5±0.2	0.0005±0.0001	0.57	0.405±0.006	0.0226±0.0004	1
HG469	57,288	6.3±0.2	0.0007±0.0001	0.77	0.47±0.01	0.0219±0.0006	1
HG512	21,006	2.4±0.1	0.00068±0.00006	0.94	0.168±0.006	0.0149±0.0009	0.94
HG552	48,312	11.3±0.3	-0.0006±0.0002	0.53	0.976±0.009	0.0325±0.0003	1
LG090	6,930	6.05832±0.00009	0.2157±0.0001	0.05	0.46±0.02	0.0260±0.001	1
LG131	57,684	5.2±0.3	0.0012±0.0002	0.88	0.340±0.005	0.0150±0.0004	1
LG247	1,408	2.6±0.3	0.0012±0.0002	0.82	0.21±0.03	0.0140±0.004	0.98
LG465	120,658	3.7±0.1	0.00076±0.00007	0.92	0.27±0.01	0.0180±0.001	1
LG598	101,614	2.76±0.07	0.00024±0.00004	0.77	0.23±0.01	0.0250±0.001	0.99

A Comparison between the nonlinear models used to calculate the parametric images of HG021 and LG131 when applied to the mean SUVs of the respective STVs across time is presented on Figure 3.23.

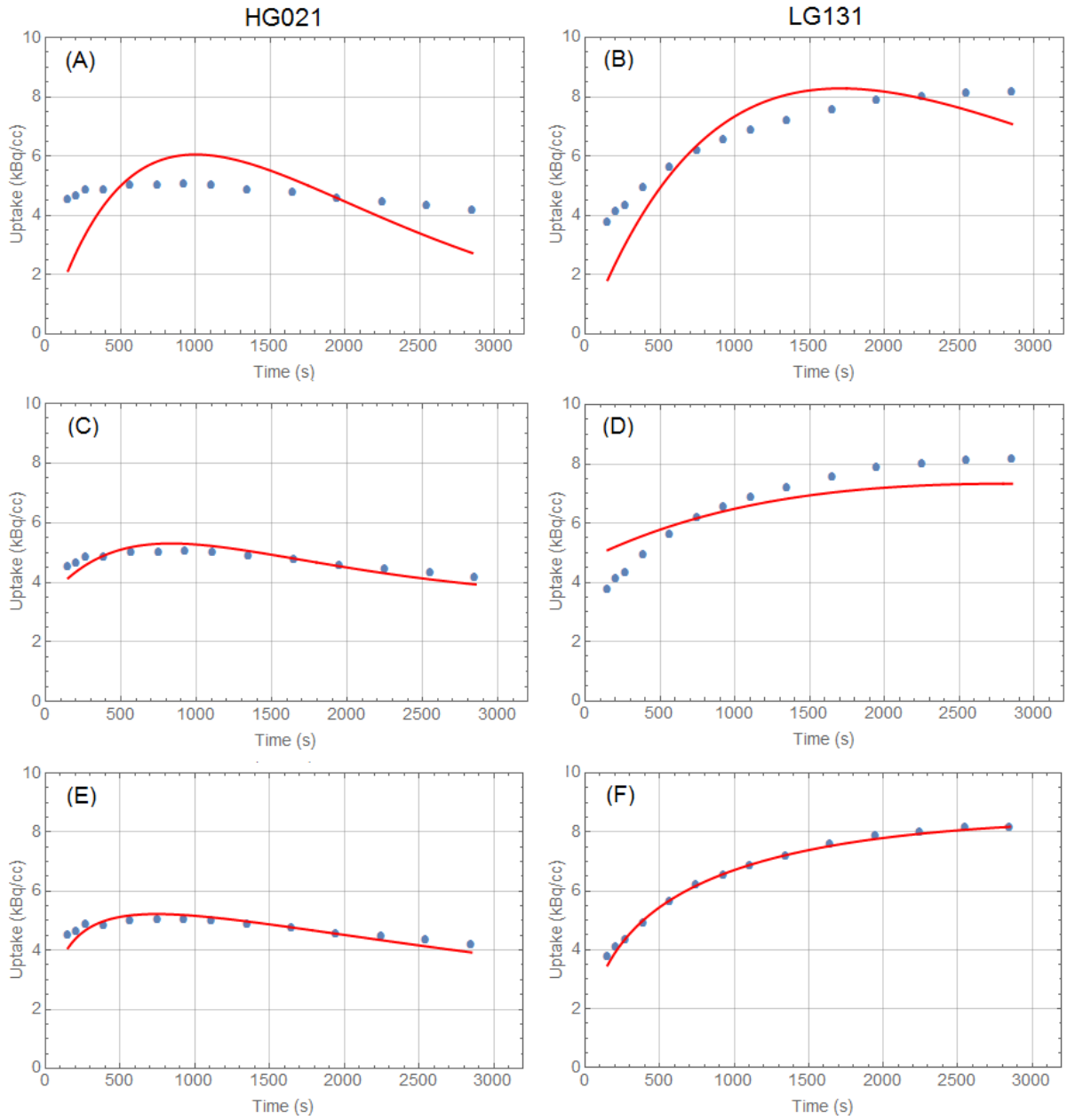

Figure 3.23 - Comparison between the nonlinear models used to calculate the parametric images of HG021 and LG131 when applied to the mean SUVs of the respective STVs across time. The first row shows the results from the nonlinear regression fit with the simple exponentially damped linear model (A and B). The second row shows the results obtained with the exponentially damped model with an offset (C and D), and the last row shows the results from the exponentially damped linear model with square-root time dependence fit (E and F).

Table 3.2, Table 3.3, Table 3.4, and Table 3.5 show the mean values of the estimated parameters from linear and nonlinear regression model fit to the STVs. The nonlinear parameters considered in Tables 3.4 and 3.5 are from fits performed with the exponentially damped linear model with square-root time dependence.

Table 3.2 - Mean values of the intercept parameter from linear regression model fit to the STVs.

Intercept					
All HGG		Except HG512		All LGG	
Tumor	Control	Tumor	Control	Tumor	Control
5.95±2.93	2.54±1.02	6.66±2.64	2.75±0.98	4.06±1.52	2.3±0.52

Table 3.3 - Mean values of the slope parameter from linear regression model fit to the STVs.

Slope					
All HGG		Except HG512		All LGG	
Tumor	Control	Tumor	Control	Tumor	Control
0.0201±0.0006	0.0002±0.0001	0.0002±0.0006	0.0002±0.0001	0.04±0.09	0.0002±0.0003

Table 3.4 - Mean values of the amplitude (A) parameter from nonlinear regression model fit to the STVs with the exponentially damped linear model with square-root time dependence.

A					
All HGG		Except HG512		All LGG	
Tumor	Control	Tumor	Control	Tumor	Control
0.40±0.27	0.21±0.08	0.55±0.25	0.23±0.08	0.3±0.1	0.2±0.05

Table 3.5 - Mean values of the κ parameter from nonlinear regression model fit to the STVs with the exponentially damped linear model with square-root time dependence.

κ					
All HGG		Except HG512		All LGG	
Tumor	Control	Tumor	Control	Tumor	Control
0.023±0.008	0.024±0.003	0.027±0.007	0.025±0.003	0.020±0.006	0.026±0.105

After performing a 2-sided Mann-Whitney U test to the data on Table 3.1, at a level of significance $\alpha = 0.05$, only the A parameter was shown to be significantly different between high-grade and low-grade (p-value= 0.04).

3.2.Tumour region parametric images

Parametric images based on linear and nonlinear regression fitting of FET data in each voxel were generated for the eleven patients. Here, only two cases are presented for simplicity: one from a low-grade glioma (LG131), and another from an high-grade glioma (HG021). The results are presented in the following sections.

3.2.1. Linear model

Parametric images of intercept y, and slope m were calculated based on linear regression fitting of data in each voxel. Figure 3.24 shows the parametric images of a slice of a manually selected tridimensional area containing the tumour. On the left column, images of the summed SUV values along time are shown. On the very right, images of distribution of R^2 are shown. Blank areas in the middle of the parametric images indicate that the values were out of the plot range. This can either mean that the values are very large, or that the fit failed to converge.

3.2.2. Nonlinear models

Parametric images of parameters A and κ were calculated based on nonlinear regression fitting of data in each voxel. Figure 3.25, Figure 3.26, and Figure 3.27 show the parametric images of a slice from a manually selected tri-dimensional area containing the tumour. On the left column, images of the summed SUV values along time are shown. On the very right, images of the distribution of R^2 are shown. Blank areas in the middle of the parametric images indicate that the values were out of the plot range. This can either mean that the values are very large, or that the fit failed to converge. In Figure 3.25, the results from the exponentially damped linear model are depicted. Figure 3.26 presents the parametric images generated with the exponentially damped linear model with an offset, and Figure 3.27 shows the images obtained from nonlinear regression fit with the exponentially damped linear model with square-root time dependence.

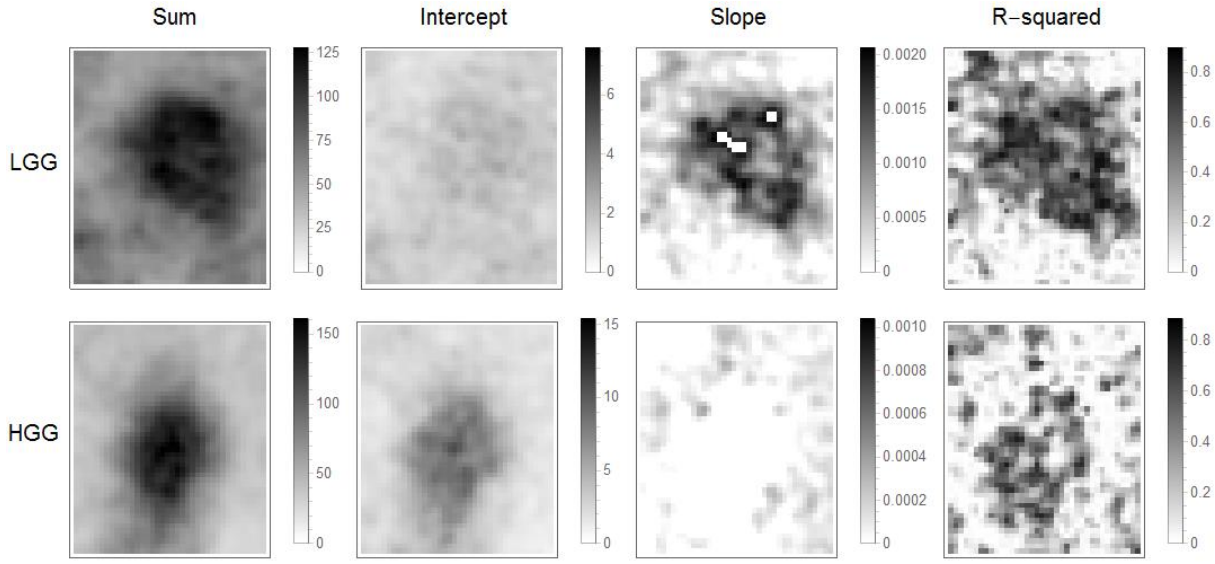

Figure 3.24 - Parametric images of slope and intercept from linear regression fitting of data in each voxel.

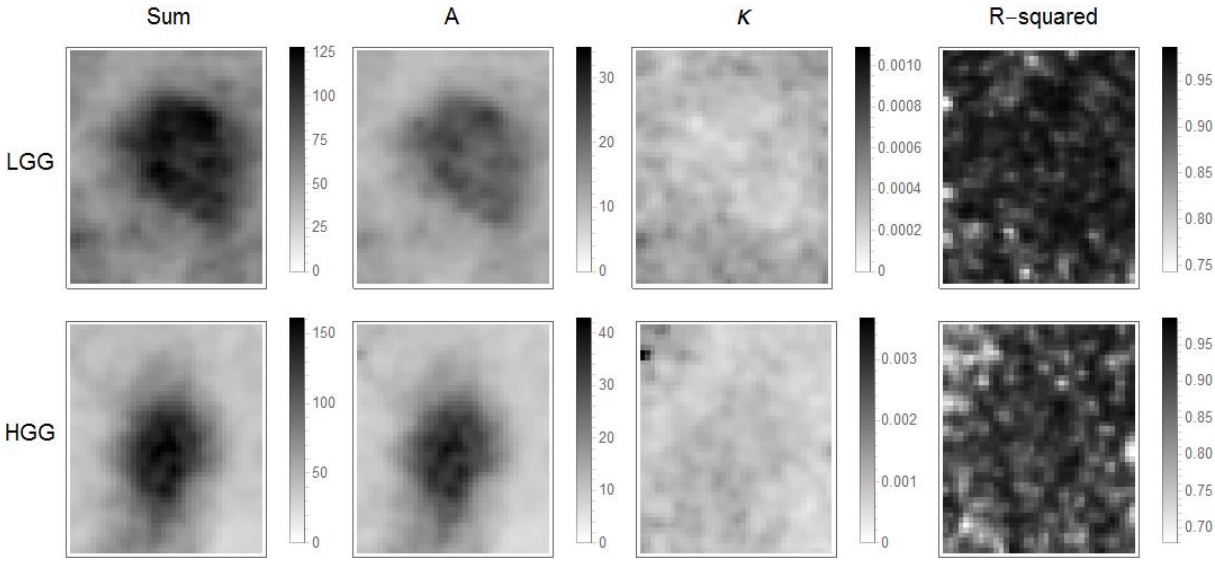

Figure 3.25 - Parametric images of A and κ obtained from nonlinear regression fitting of data in each voxel (exponentially damped linear model).

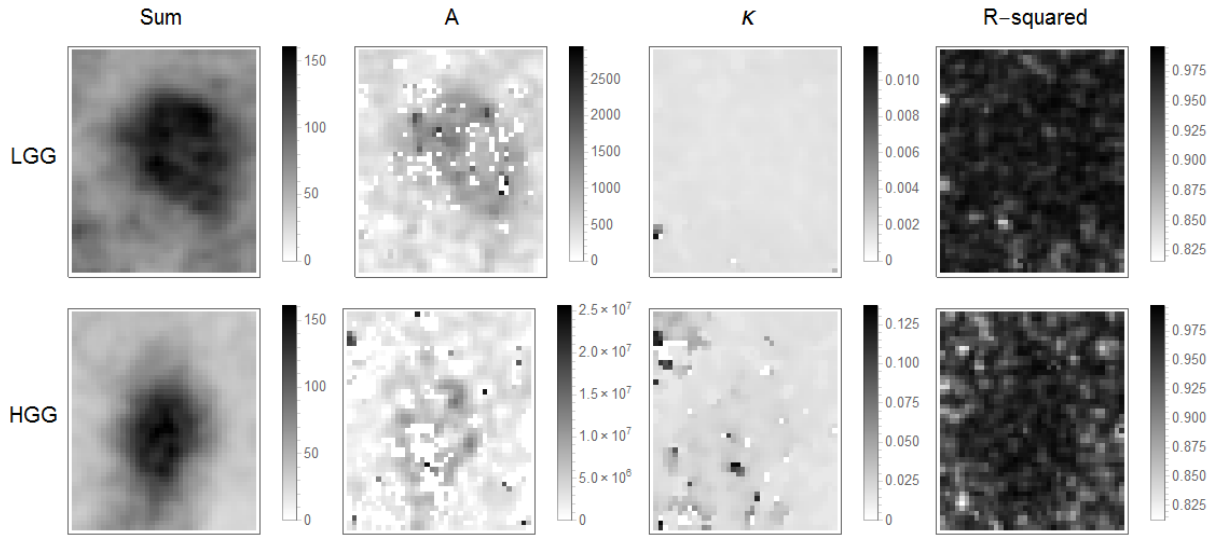

Figure 3.26 - Parametric images of *A* and κ obtained from nonlinear regression fitting of data in each voxel (exponentially damped linear model with offset).

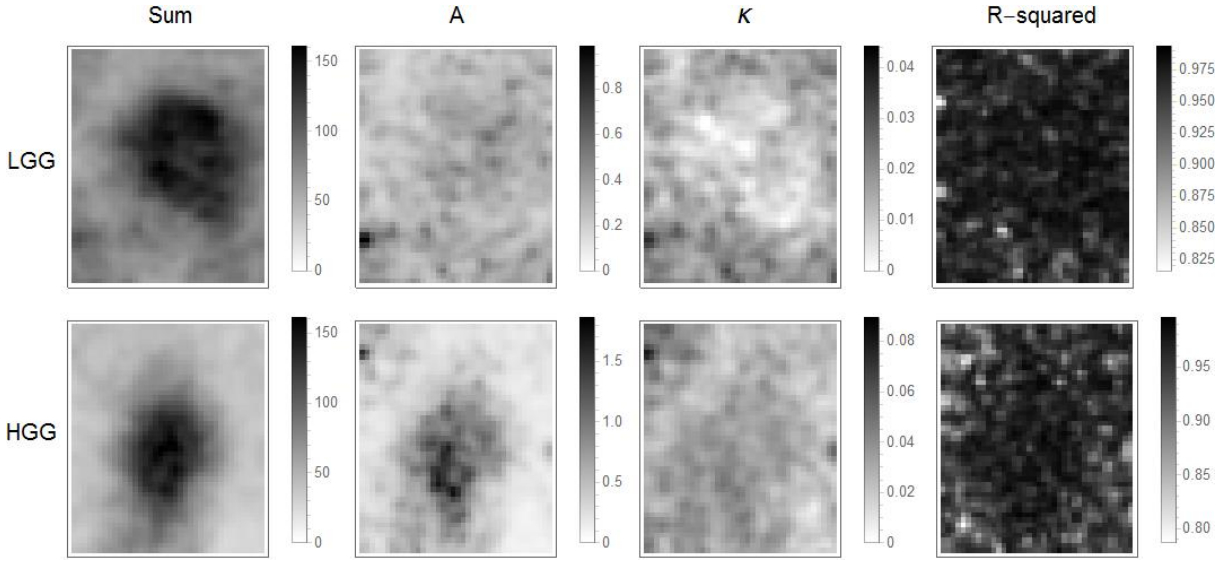

Figure 3.27 - Parametric images of *A* and κ obtained from nonlinear regression fitting of data in each voxel (exponentially damped model with square-root time dependence).

In order to better illustrate the different model behaviours on STV fitting and on voxel-wise fitting, Figure 3.28 shows the results from the fits with the nonlinear models, and respective parametric images, on patient LG131.

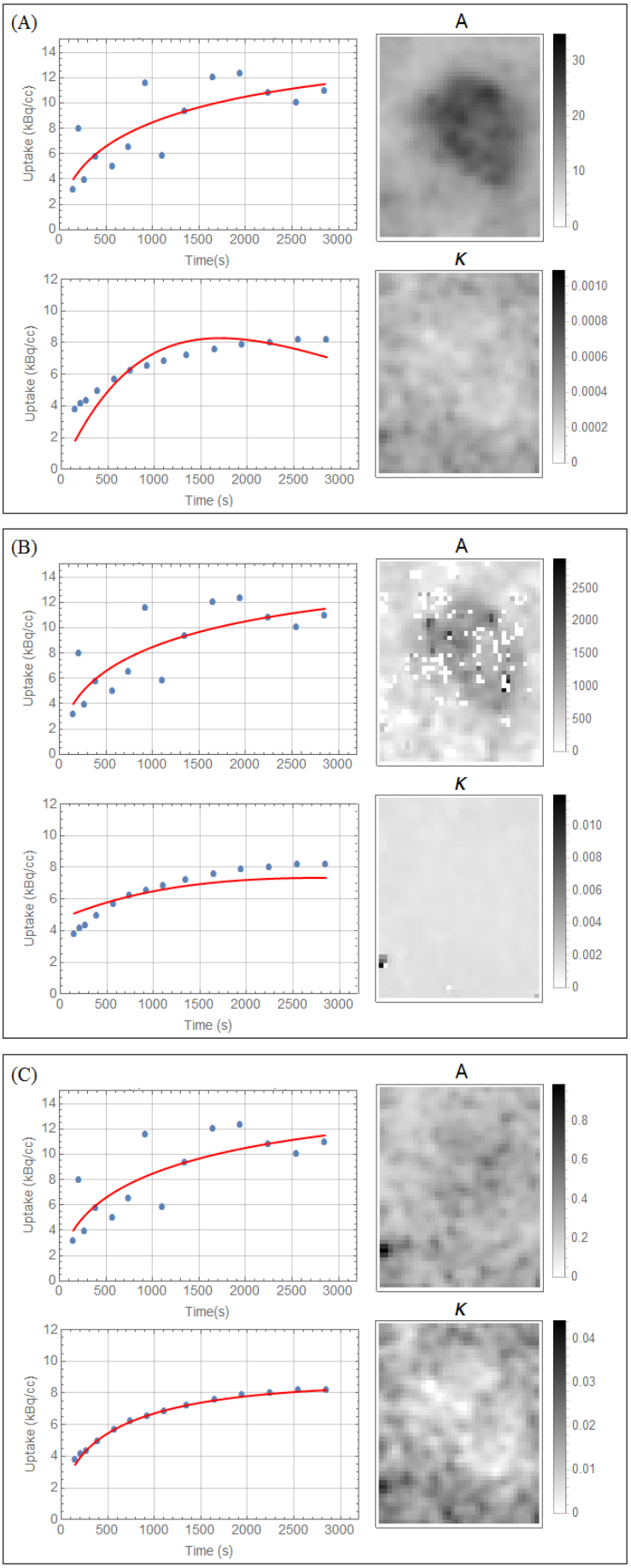

Figure 3.28 - Fit results of the three nonlinear models on a single voxel inside the tumour region (top plot, on the left) and on the STV (bottom plot, on the left) of patient LG131, and respective parametric images (on the right). (A) shows the results from the nonlinear regression fit with the simple exponentially damped linear model. (B) shows the results obtained with the exponentially damped model with an offset, and (C) shows the results from the exponentially damped linear model with square-root time dependence fit.

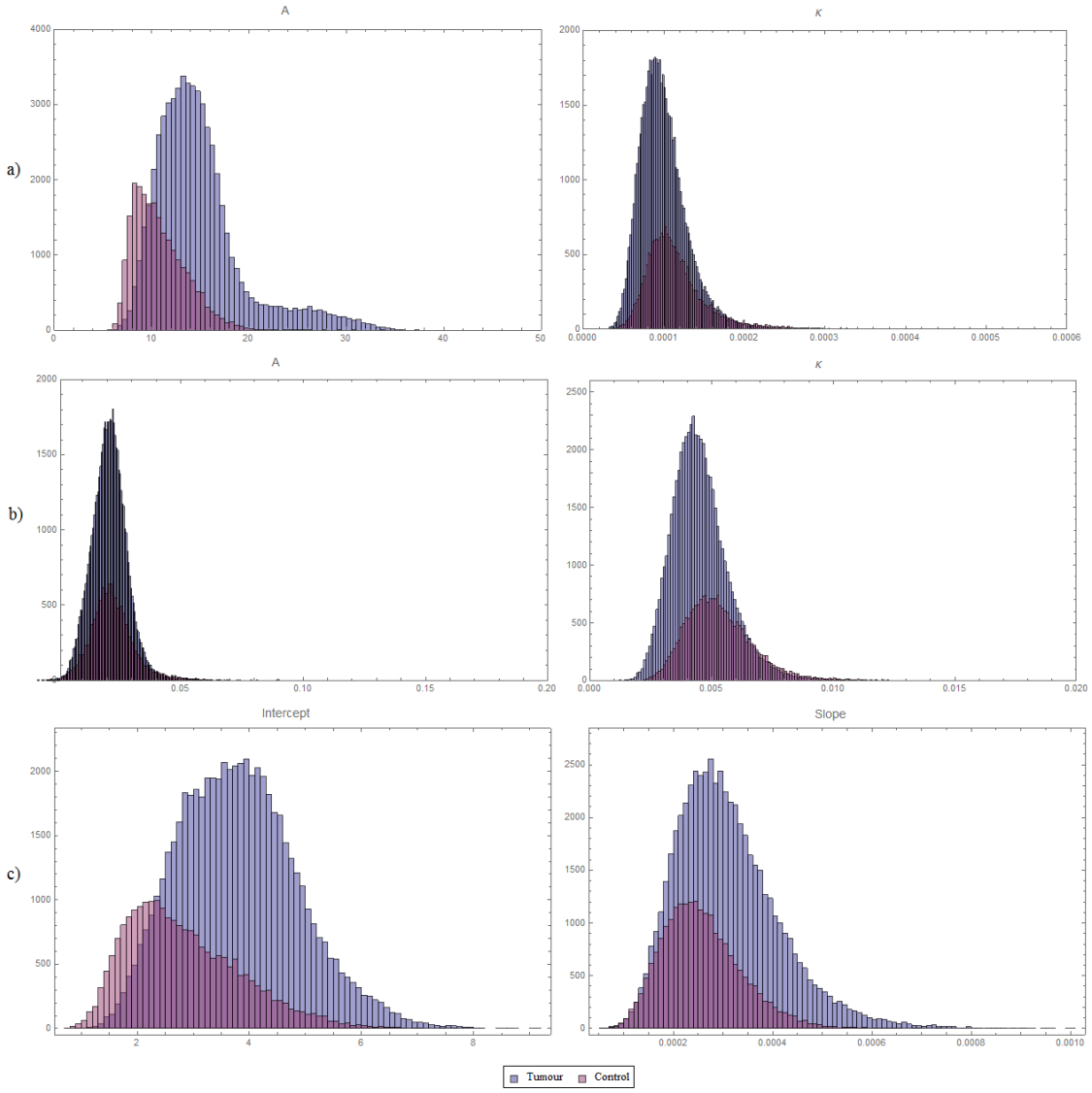

Figure 3.29 - Parameter distribution obtained from fitting of LG131 tumour and control data in each voxel: a) exponentially damped linear model; b) exponentially damped linear model with square-root time dependence; c) linear model.

Voxel-wise fit was also performed in control regions. The histograms on Figure 3.29 show the distribution of the different parameters in both tumour and control area of LG131. The histograms are from two of the nonlinear regression based fits, and for the linear regression based fit. The histograms on the first row (Figure 3.29a) correspond to the results from the exponentially damped linear model; the second row (Figure 3.29b) depicts the results from the square-root time dependence model, and the last row (Figure 3.29c) shows parameter distribution for the linear regression voxel-wise fit. Histograms for relative error distribution were also calculated, and are shown in Figure 3.30.

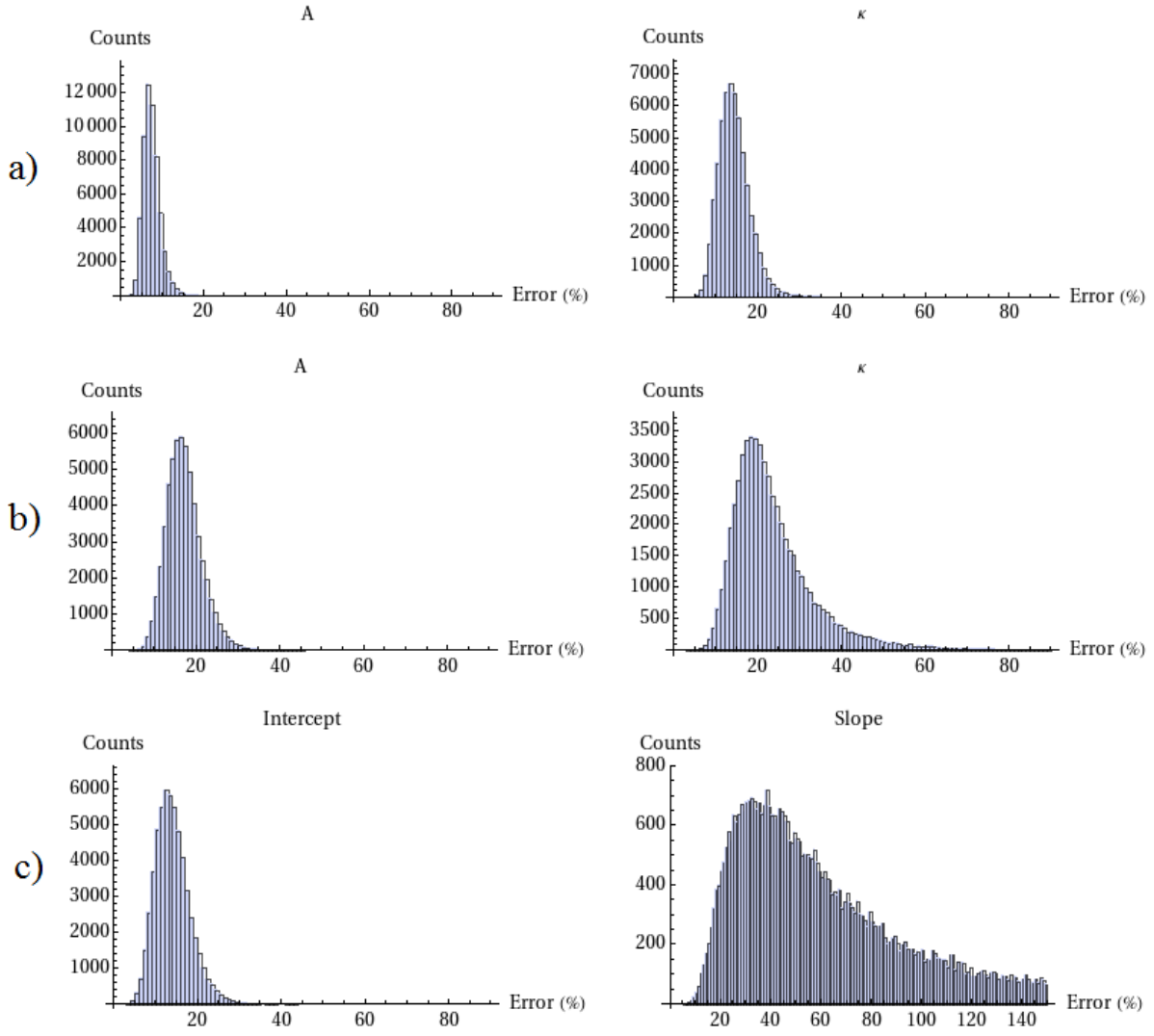

Figure 3.30 - Parameter error histograms obtained from fitting of LG131 data in each voxel: a) exponentially damped linear model; b) exponentially damped linear model with time dependence; c) linear model.

The histograms on Figure 3.31 show the distribution of the different parameters in both tumour and control area of HG021. The histograms are from two of the nonlinear regression based fits, and for the linear regression based fit. The histograms on the first row (Figure 3.31a) correspond to the results from the exponentially damped linear model; the second row (Figure 3.31b) depicts the results from the square-root time dependence model, and the last row (Figure 3.31c) shows parameter distribution for the linear regression voxel-wise fit. Histograms for error distribution were also calculated, and are shown in Figure 3.32. For comparision with the other nonlinear models, Figure 3.33 presents the histograms for error distribution with the exponentially damped linear model with an offset for LG131.

Identical analysis was performed for the remaining image volumes, but due to the similarities between the results, only these two cases are presented.

Mean and standard deviation of the R^2 values obtained from nonlinear and linear regression voxel-wise fitting of all data volumes are presented in Table 3.6.

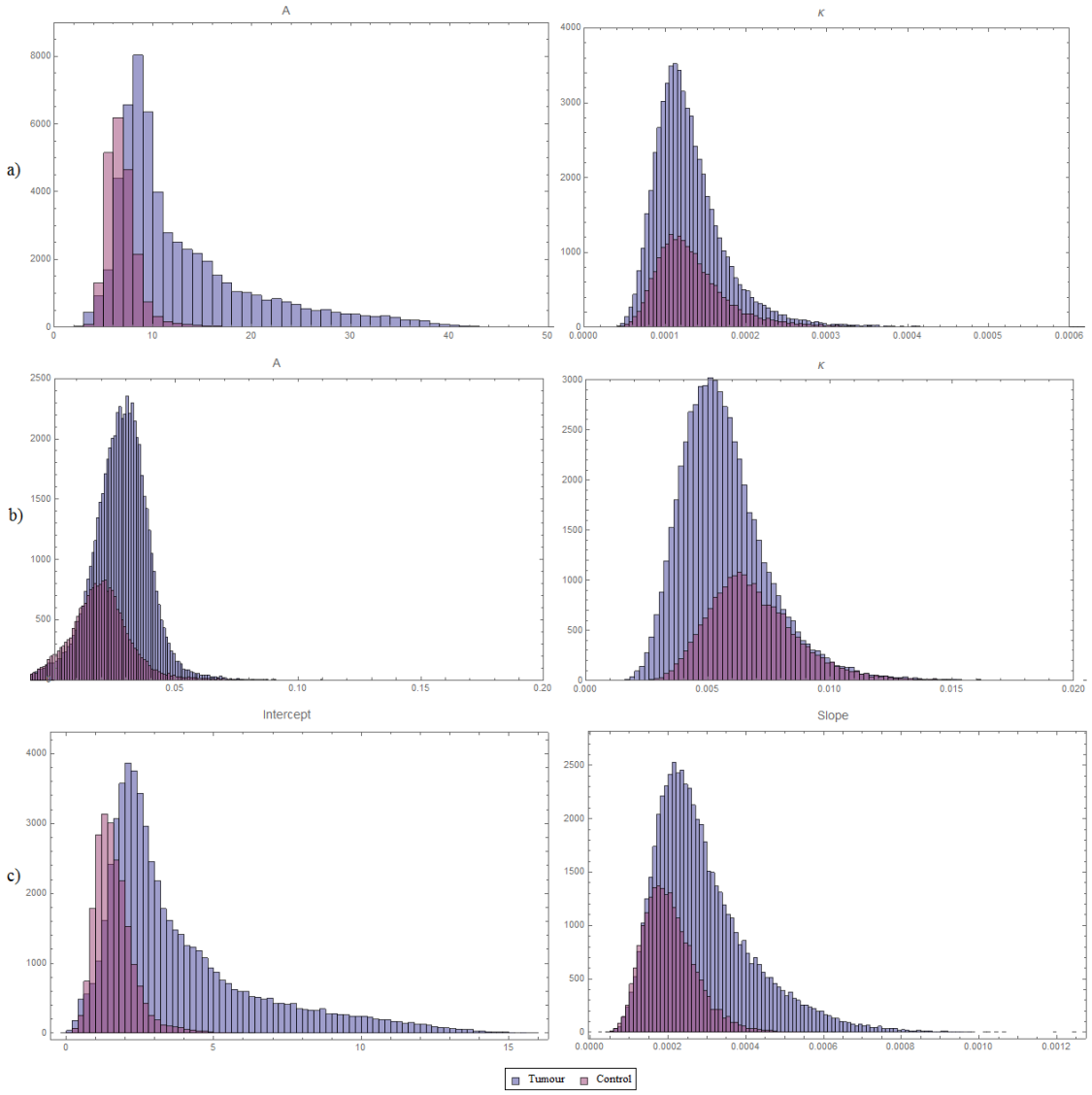

Figure 3.31 - Parameter distribution obtained from fitting of HG021 tumour and control data in each voxel: a) exponentially damped linear model; b) exponentially damped linear model with time dependence; c) linear model.

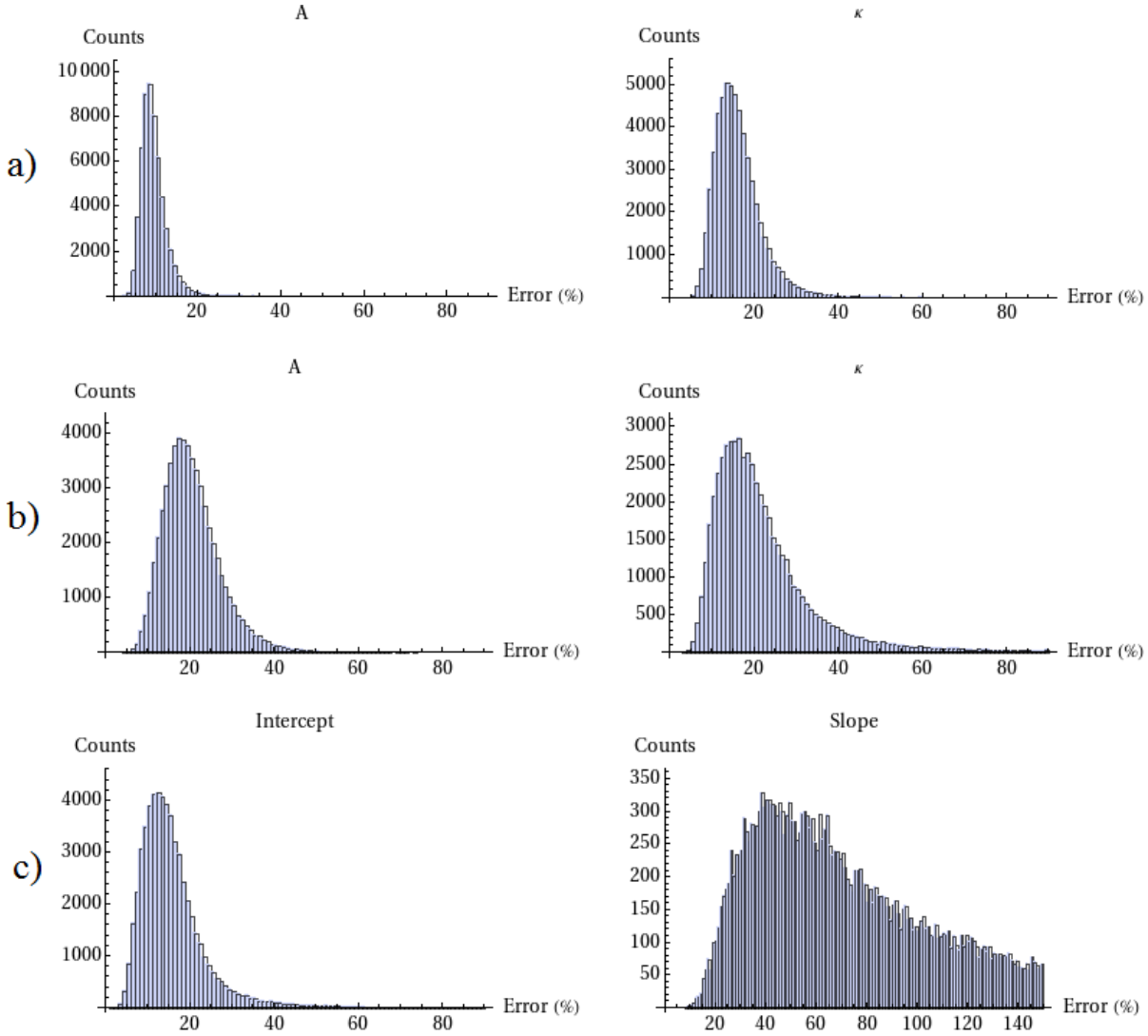

Figure 3.32 - Parameter error histograms obtained from fitting of HG021 data in each voxel: a) exponentially damped linear model; b) exponentially damped linear model with time dependence; c) linear model.

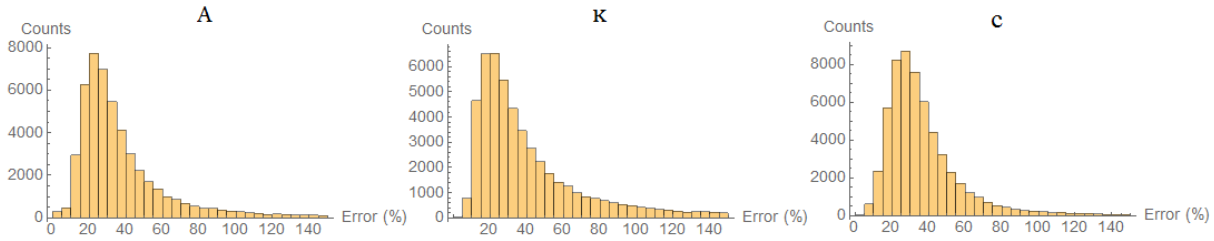

Figure 3.33 - Parameter error histograms obtained from fitting of LG131 data in each voxel with the exponentially damped linear model with an offset.

Table 3.6 - Mean R^2 from the voxel-wise fit with the linear and the non-linear models.

	Linear model	Exponentially damped linear model	Square-root time-dependence model
HG020	0.26±0.22	0.92±0.05	0.95±0.03
HG021	0.19±0.20	0.91±0.05	0.94±0.03
HG417	0.23±0.21	0.92±0.05	0.94±0.03
HG469	0.18±0.18	0.84±0.10	0.88±0.09
HG512	0.20±0.19	0.85±0.10	0.89±0.09
HG552	0.13±0.15	0.81±0.11	0.85±0.09
LG090	0.17±0.14	0.91±0.04	0.95±0.02
LG131	0.26±0.23	0.94±0.03	0.96±0.02
LG247	0.43±0.23	0.91±0.05	0.93±0.03
LG465	0.33±0.23	0.90±0.06	0.93±0.04
LG598	0.16±0.17	0.82±0.09	0.86±0.07

3.3. Whole-head parametric images

Whole-head parametric images of amplitude, A, and curve shape, κ were calculated based voxel-wise fitting of a exponentially damped linear model with square-root time dependence. The results for two patients (LG131 and HG021) are presented in Figure 3.34. Only one representative slice (z axis) of the fitted head volume is shown. The top row corresponds to the graphic representation of the summed uptake values in the head region over time. The bottom row shows the distribution of the R^2 values.

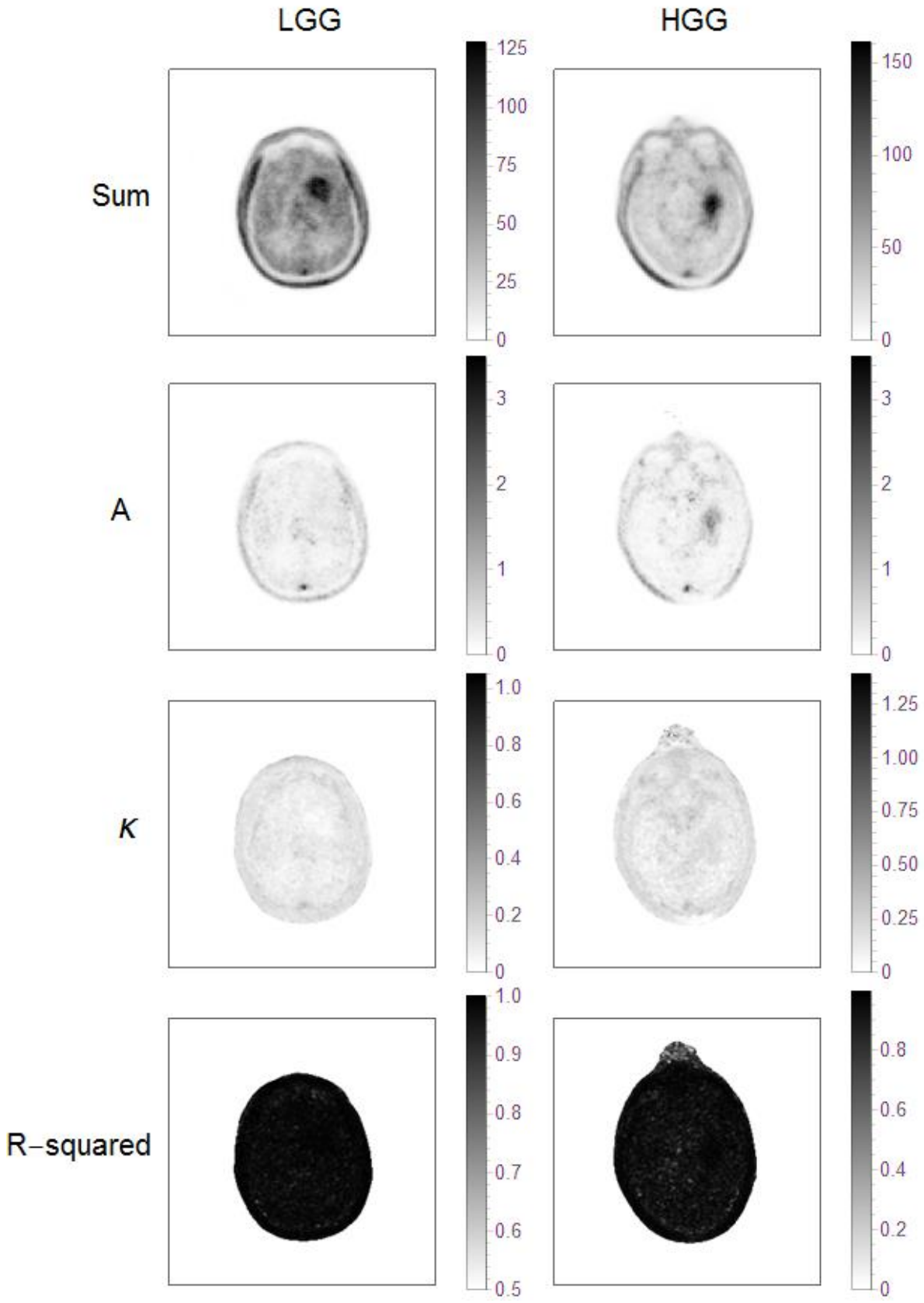

Figure 3.34 - Whole-head parametric images of A and κ obtained from nonlinear regression with exponentially damped linear model with square-root time dependence fitting of data in each voxel.

4. Discussion

The goal of this project was to develop a robust method to generate parametric images of FET reflecting tumour grade. Preliminary work on modelling FET curves was already performed, and in previous studies parametric images were generated using linear regression methods [61]. Even though linear regression methods are simple and robust, they present some relevant limitations. They either are applied after uptake peak, excluding the data prior to that time point, or are too simplistic, being unable to model nonlinear dependencies on individual parameters. Here, a more accurate curve fitting was looked for. Using nonlinear regression methods to fit FET data curves allowed for discarding less data, since only the first two minutes of acquisition were rejected. The amount of unused data in this case was considerably less than in traditional linear regression model fit scenarios, which would include discarding the data prior to peak, or after it. It was observed that the TTP for FET in brain tumours depends upon their property of being high-grade or low-grade. Thus, TTP method is already suboptimal, because the decision of discarding the data is prior to knowing the type of tumour being studied. In a study by Herzog *et al.* [60], in which this work was based on, only the first five minutes of acquisition remained unused. Taking advantage from the fact that a nonlinear model would, by definition, better fit to the typical shape of PET TACs, we tried to incorporate even more data into the analysis. The importance of using more of the initial data is well illustrated by case LG090. As seen in Figure 3.6, the shape of the TAC changes as more or less of the initial data is excluded from the fitting. Because the first 5 frames are discarded when applying the linear fitting, the resulting TAC shows no characteristic tumour uptake shape. On the other hand, when only 2 frames are excluded, the initial uptake rise can be seen in the averaged TAC. The inclusion of more data is also beneficial because when looking into the SUVs of the STV averaged over time, the curve is less noisy, allowing for a better fit. The same applies to the calculation of the parametric images.

4.1. Fits applied to segmented tumour volume

When fits were applied to a single TAC, obtained by building the mean over all voxels TACs inside the segmented tumour volume, 3-dimensional masks were created to select the tumour data. A threshold method was used. Because of its simplicity, it is possible that the calculated masks either included healthy tissue, or excluded some tumour regions. The dimension of the masks could also have played a role on the performance of the fit, since smaller regions lead to noisier TACs. In the previous section, Table 3.1 shows the summary of the parameters calculated from the STVs fittings, as well as the dimensions of the volumes where voxel SUVs were averaged. The STVs of LG247 and LG090 were the smallest, and the TACs of these two cases were the noisiest. In the case of LG090, the linear regression fit returned an extremely low R^2 value (R^2 =0.05), while the corresponding nonlinear fit returned a R^2 value of 0.99. Even though a R^2 close to zero is associated with horizontal curves, the model performed poorly when fitting the data in this case because the TAC was too noisy, and noise increases uncertainty in parameters. Table 3.1 also shows that R^2 values for the linear fit are in general much worse than for nonlinear regression (R^2 values closer to 1 indicate that the fit works better).

An example of failed segmentation is patient HG512. As presented in the previous section, the generated mask contained both tumour and bone. As a result, the fit was applied only to the data from a small area inside the segmented volume. A look at Figure 3.18 shows that the nonlinear model was able to reproduce the data. However, the retrieved parameters were lower than the ones from the other high-grade gliomas, both for linear and nonlinear fit. This difference may come from the faulty segmentation.

To solve this problem, a more complex segmentation procedure would have to be developed. There are tools that allow for a more precise segmentation, but their use would have increased the complexity of the workflow. Since the segmentation implemented with Mathematica was working well for the other image volumes and robust segmentation was not within the scope of this work, no other solution was sought after.

The selection of patients in this study was based on the challenge to improve diagnostic information about cerebral lesions in which classification based on kinetic profile was unclear. That means that the cohort was chosen to have a large variety of curves/cases and especially unclear cases were chosen in order to be sure that the model works also for these cases. As so, despite the potential lack of accuracy of the segmentation procedure, in some cases the TACs do not look as expected for clear differentiation between low-grade and high-grade. However, after fitting the data curves, some tendencies in the estimated parameters showed clues regarding tumour grading. Table 4.2 presents the mean values for the estimated fit parameters. Visual inspection of these values, together with Table 4.1, reveals that the intercept, slope, *A*, and κ parameters for the high-grade gliomas were in general higher than the one for the low-grade gliomas. If HG512 is left out of the calculations, then the difference is even bigger.

Regarding the linear regression model fits, the difference in slope values was not as expressive as the one reported by Herzog *et al.* [60]. In that study, linear regression model fits applied to high-grade gliomas returned negative slope values, whereas the computed slope parameter values for low-grade gliomas were positive. Those results are in line with the typical kinetic profile expected from high-grade and low-grade tumours. In the first case, since tracer uptake decreases after an early peak, the linear fit is expected to consist of a negative slope curve. The opposite is expected from low-grade glioma fitting, because here the uptake increases steadily along time. However, in this work, only two out of the 6 fitted high-grade STVs had negative slope values. This result is related to the criteria for patient selection. Except for HG021 and HG552, none of the other high-grade tumours had a clear kinetic profile. Nonetheless, slope values of the fitted high-grade gliomas were still lower than the ones for low-grade gliomas.

Intercept values were also higher in fitted high-grade gliomas. The fact that high-grade gliomas revealed increased uptake goes in line with previous study findings [51, 52].

The exponentially damped linear model with square-root time dependence used for the nonlinear regression fits also allowed for a distinction between tumour grading. The amplitude parameter calculated for the high-grade gliomas was higher than the one returned by fitting the low-grade gliomas. As so, the nonlinear regression model successfully reflected differences in the uptake of between tumour grades.

The κ parameter was also higher for high-grade gliomas, thus reflecting differences in curve shape between high-grade and low-grade glioma. As discussed in section 2, plotting the nonlinear model used for the fits with higher κ values mimics the expected kinetic profile (i.e., TAC) of FET data on a low-grade glioma. But in Figure 2.2, Figure 2.3, and Figure 2.4, the models are plotted with a fixed amplitude value. Here, however, the amplitude parameter also changes, and it is higher in high-grade gliomas. This hints at a dependence between the two parameters. Previous works with linear regression models relied on a difference in slope signal to distinguish between tumour grades. We hoped nonlinear based fitting would allow for better tumour grading based on only one parameter, namely the κ parameter. To access the ability of each parameter to distinguish between high-grade and low-grade, a 2-sided Mann-Whitney U test was performed. The goal was to compare the mean values of each parameter, and see in which case there was a significant difference between tumour grades. At a level of significance $\alpha = 0.05$, only the A parameter was shown to be significantly different between high-grade and low-grade (p-value= 0.04). Additionally, by looking to the R^2 values disclosed in Table 3.6, it is shown that the nonlinear model reproduces the data better.

Out of the three studied nonlinear models, only the model with square-root time dependence was presented as the nonlinear alternative in the previous STV fitting. Looking to Figure 3.25 for voxel wise fits, the performance of the simple exponentially damped linear model seemed to be as good, with overall convergence, and high R^2 values. However, it was found that when fitting the average STV TACs, the model fails to correctly reproduce the data. Figure 3.23 shows the comparison between the nonlinear models used to calculate the parametric images of HG021 and LG131 when applied to the mean TACs of the respective STVs across time. It is clear that, even though parametric images looked promising, the model does not fit correctly to the data. The offset model also failed to fit the data from the STV while giving reasonable fit results for voxel wise fitting, as seen in Figure 3.24, and for that reason it was also excluded. In order to better illustrate the difference in quality of fit between the three nonlinear models, Figure 3.28 shows the results from the fits with the nonlinear models, and respective parametric images, on patient LG131. Looking to the fit applied to a single voxel within the tumour region does not allow for distinction between model performance. The data is too noisy for allowing precise reproduction of single-voxel data with either of the models. However, the differences can be observed once the noise decreases, which is what happens when the mean TAC over the STV area is computed. Overall, the model with square-root time dependence performed the best.

4.1. Voxel-wise fit and parametric images

In contrast to previous dynamic evaluations of FET PET that were based on the interpretation of the uptake curve in a predefined region within the tumour volume, parametric images provide the option to display variable grades of malignancy within the tumour volume.

Two out of three tested nonlinear models showed promising results regarding the distinction between tumour grades. For the simple exponentially damped linear model, while the amplitude (A parameter) images accurately reproduce the sum images, the parametric images of the κ parameter allow the distinction between the two tumours. In the image of HG021, a darker central area is surrounded by a lighter one. On the other hand, in the case of the LG131, the central area is lighter than the surroundings. This means that in the high-grade glioma, κ parameter has higher values than the background/healthy tissue, whereas in the low-grade glioma, the values of the κ parameter are lower than the ones calculated for the surrounding healthy tissue.

The exponentially damped linear model with square-root time dependence also allowed for differentiation between low-grade and high-grade. As with the first model, the κ parameter images were different in both cases with higher-than-background values for the high-grade glioma and lower-than-background values for the low-grade glioma, but the difference is not as visually evident as in the previous case. However, the amplitude images calculated based on the square-root model also allowed for tumour grading. While for the high-grade tumour the parametric image of A replicated the sum image of the corresponding tumour, for the low-grade glioma the tumour area approaches values very similar to surrounding healthy tissue.

The exponentially damped model with an offset performed the worst out of the tested models. The offset parameter was originally added as an attempt two include more information into the fitting, and better reproduce the data. However, the extra parameter mostly added instability to the fit, thus leading to worst results, especially when calculating the parametric images. Although the R^2 values were very close to 1, it is clear that this model fails to reproduce the data. Furthermore, it was impossible to generate a parametric image of κ for the low-grade tumour using this model due to the high number of outliers, and the relative errors associated to the computed parameters were higher than for the other models, as illustrated by Figure 3.33.

The linear model has problems in reproducing the data, as seen in Figure 3.24. The parametric images of the slope parameter show extensive white areas corresponding to outliers. The values for the R^2 were closer to zero, especially in the areas corresponding to healthy tissue, as shown in Table 3.1. Also, the errors associated with the slope parameter calculation were the highest. This performance was expected and it was one of the reasons for this work. It was thought that models that were more capable of reproducing kinetic data would also allow for better distinction between high-grade and low-grade tumours. However, if we try to visually distinguish between high-grade and low-grade based solely on one parameter, the linear model performs better. Regardless of the outliers, tumour grade distinction is possible when looking to the parametric images of the slope parameter (Figure 3.24), with low-grade gliomas taking higher slope values than the surrounding healthy tissue, and high-grade gliomas taking slope values that are lower than the ones calculated for the neighbouring tissue. Tables 3.3 and 3.4 show difference between high-grade and low-grade in the parameters resulting from linear regression fit, but the differences were not significant ($p\text{-value}_{intercept}= 0.09$; $p\text{-value}_{slope}=0.06$).

This results that, after all, a nonlinear regression approach to FET data fitting does not necessarily yield the best results when it comes to tumour grading. The data may be better reproduced in cases where the kinetic profile is not clear, but when it comes to tumour grading based on parametric imaging, linear regression models perform better based on one parameter only. A visual distinction is possible with nonlinear regression based parametric images, but only when comparing the amplitude images with the sum images, or when using amplitude and κ parameters together.

4.2. Whole-head parametric images

Whole-head parametric images were successfully generated using the exponentially damped linear model with square-root time dependence. As with the parametric images confined to the tumour region, here the amplitude images also allow for differentiation between low-grade and high-grade. The values of the A parameter in the low-grade tumour are similar to the ones calculated for the surrounding healthy tissue. On the contrary, amplitude values in the high-grade tumour are higher than amplitude values of the background. Using both sum images and amplitude parameter images, it is then possible to distinguish the tumours according to their grade. This result is also reproduced by the linear regression. The difference between the parametric images of κ for each tumour is not very evident. When looking into the small-region parametric images, κ parameter allows for tumour grading. However, that difference does not show as well in the whole-head images. For the low-grade tumour, it is possible to see a small brighter area in the right brain hemisphere; for the high-grade tumour, a slightly darker area shows in the parametric images. However, these areas are difficult to spot. Comparing the sum images with the amplitude and the κ images allows for an easier, more accurate distinction between high-grade and low-grade. The R^2 values estimated for the voxel-wise fit were overall very close to 1 for both image data.

5. Conclusion

Nonlinear regression models are better at reproducing FET TAC characteristics. The more robust models are the ones with only 2 parameters. Their simplicity allows for better, more robust fits. For mean TAC fitting, a model with square-root time dependence reproduced FET data more accurately than a simple exponentially damped linear model. Furthermore, the A parameter extracted from the fitting with the square-root time dependence model was the only parameter showing a significant difference between high-grade and low-grade tumours.

When generating parametric images based on voxel-wise fit, the nonlinear regression models with 2 parameters performed the best, with less voxel fit values falling out of plot range, and less convergence issues. R^2 values for the nonlinear regression model based fits were close to 1 in both mean TAC fitting, and parametric image calculation. In the case of the parametric images generated with the exponentially damped with square-root time dependence model, visual distinction between tumour grade was possible, but not based on one single parameter. Using the parametric images of the amplitude parameter, *A*, in combination with the images of the κ parameter and the images of the summed uptake across time, it was found that the low-grade tumours take *A* values close to the ones from the surrounding healthy tissue, thus "disappearing" from the image. On the other hand, the amplitude image of the high-grade tumours reflect tumour uptake. Visual distinction using the parametric images of κ was possible in cases were the kinetic profile was clearer and/or in combination with the A image.

On the other hand, linear regression model fits returned R^2 values that were close to zero in both mean TAC fitting and parametric image calculation. However, when parametric images were calculated, it was shown that, although the linear model fails to accurately reproduce FET kinetic data, it allows for a better distinction between high-grade and low-grade gliomas based on one parameter only. Even though the parametric images show some outliers, for low-grade tumours, the slope images show that the tumour region takes higher slope values than the surrounding healthy tissue. The opposite is seen in the slope images of high-grade gliomas.

In general, it is possible to say that, nonlinear models reproduce FET TAC better. Therefore, prediction of low-grade or high-grade on STVs is better with nonlinear models. However, the distinction between high-grade and low-grade tumours based on one parameter (i.e, based on only slope or κ parametric images) is better achieved by using linear regression model fitting. Prediction of high-grade or low-grade gliomas on joint inspection of A and κ, or intercept and slope has still to be studied. Future work on nonlinear model fitting should focus on better understanding why the square-root time dependence allows for such accurate reproduction of FET TAC. The dependence between the A and κ parameters and especially a joint interpretation of both parameter images should also be studied for differentiation of high-grade and low-grade tumours.

References

[1] Leung K. "[^{18}F]Fluoro-2-deoxy-2-o-glucose". Moleccular Imaging and Contrast Agent Database (MICAD) [Internet]. Bethesda (MD): National Center for Biotechnology Information (US); 2004-2013.

[2] Patronas NJ, Di Chiro G,Brooks RA, et al. "Work in progress: [^{18}F fluoro-deoxyglucose and positron emission tomography in the evaluation of radiation necrosis of the brain". *Radiology*. 1982;144:885-889.

[3] De Witte O, Levivier M, Violon P, et al. "Prognostic value of positron emission tomography with [^{18}F]fluoro-2-D-glucose in the low-grade glioma". *J Neurosurg*. 1996;39:470-477.

[4] Olivero WC, Dulebohn SC, Lister JR. "The use of PET in evaluating patients with primary brain tumours: is it useful?" *J Neurol Neurosurg Psychiatry*. 1995;58:250-252.

[5] Krohn KA, Mankoff DA, Muzi M, et al. "True tracers: comparing FDG with glucose and FLT with thymidine". *Nucl Med Biol*. 2004;32:663-671.

[6] Wong TZ, van der Westhuizen GJ, Coleman RE. "Positron emission tomography imaging of brain tumours". *Neuroimaging Clin N Am*. 2002;12:615-626.

[7] Leung K. "O-(2-[18F]Fluoroethyl)-L-tyrosine". Moleccular Imaging and Contrast Agent Database (MICAD) [Internet]. Bethesda (MD): National Center for Biotechnology Information (US); 2004-2013.

[8] Wester HJ, Herz M, Weber W, et al. "Synthesis and Radiopharmacology of *O*-(2-[^{18}F]fluorethyl)-L-tyrosine for Tumour Imaging". *J Nucl Med*. 1999;40:205-212.

[9] By Gladissk (Own work) [GFDL (http://www.gnu.org/copyleft/fdl.html) or CC BY-SA 3.0 (http://creativecommons.org/licenses/by-sa/3.0)], via Wikimedia Commons.

[10] Chen W. "Clinical Applications of PET in Brian Tumours". *J Nucl Med*. 2007;48:1468-1481.

[11] Pöpperl G, Gotz C, Rachinger W, et al. "Value of *O*-(2-[^{18}F]fluorethyl)-L-tyrosine PET for the diagnosis of recurrent glioma". *Eur J Nucl Med Mol Imaging*. 2004;31:1464-1470.

[12] Heiss P, Mayer S, Herz M, et al. "Investigation of transport mechanism and uptake kinetics of O-(2-[18F]fluoroethyl)-L-tyrosine in vitro and in vivo". *J Nuc Med*. 1999;40:1367-1373.

[13] Terakawa Y Tsuyuguchi N, Iwai Y, et al. "Diagnostic accuracy of ^{11}C-methionine PET for differentiation of recurrent brain tumours from radiation necrosis after radiotherapy". *J Nucl Med*. 2008;49:694-699.

[14] Leung K. "L-[methyl-^{11}C]Methionine". Moleccular Imaging and Contrast Agent Database (MICAD) [Internet]. Bethesda (MD): National Center for Biotechnology Information (US); 2004-2013.

[15] Leung K. "3'-Deoxy-3'-[^{18}F]fluorothymidine". Moleccular Imaging and Contrast Agent Database (MICAD) [Internet]. Bethesda (MD): National Center for Biotechnology Information (US); 2004-2013.

[16] The MICAD Research Team. "[^{18}F]Fluoromisonidazole". Moleccular Imaging and Contrast Agent Database (MICAD) [Internet]. Bethesda (MD): National Center for Biotechnology Information (US); 2004-2013.

[17] Leung K. "L-3,4-Dihydroxy-6-[^{18}F]fluorophenylalanine". Moleccular Imaging and Contrast Agent Database (MICAD) [Internet]. Bethesda (MD): National Center for Biotechnology Information (US); 2004-2013.

[18] Farde L, Pauli S, Hall H, et al. "Steroselective binding of ^{11}C-raclopride in living human brain: a search for extrastriatal central D2-dopamine receptors by PET". *Psycopharmacology*. 1988; 94:471-478.

[19] Chopra A. "Ethyl 8-fluoro-5-[^{11}C]methyl-6-oxo-4H-imidazol[1,5-a][1,4]benzodiazepine-3-carboxylate". Moleccular Imaging and Contrast Agent Database (MICAD) [Internet]. Bethesda (MD): National Center for Biotechnology Information (US); 2004-2013.

[20] Morris ED, Christopher JE, Schmidt, KC et al. "Kinetic Modelling in Positron Emission Tomography". In: *Emission Tomography: The Fundamentals of PET and SPECT* (Wernick MN, Aarsvold JN, eds). Elsevier Academic Press 2004; pp. 499-540.

[21] Carson RE. "Tracer Kinetic Modelling in PET". In: *Positron Emission Tomography: Basic Science and Clinical Practice* (Valk PE, Bailey DL, Townsend DW, Maisley MN, eds). Springer-Verlag London LTD 2003; pp. 147-179.

[22] Ketty SS. "The theory and application of the exchange of inert gases at the lungs and tissues". *Pharmacol Rev*. 1951;3:1-41.

[23] Sokoloff L, Reivich M, Kennedy C et al. "The ^{14}C-deoxyglucose method for the measurement of local cerebral glucose utilisation: theory, procedure and normal values in the conscious and anesthetized albino rat". *J Neurochem*. 1977;28:897-916.

[24] Mintun MA, Raichle ME, Kilbourn MR et al. "A quantitative model for the in vivo assessment of drug binding sites with positron emission tomography". *Ann Neurol*. 1984;15:217-227.
[25] Carson RE. "Parameter estimation in positron emission tomography". In: *Positron emission tomography and autoradiography: principles and applications for the brain and heart* (Phelps M, Mazziotta J, Shelbert H, eds). Raven Press New York 1986; pp. 347-390.
[26] Feng D, Huang SC, Wang Z et al. "An unbiased parametric imaging algorithm for uniformity sampled biomedical system parameter estimation". *IEEE Trans Med Imag*. 1996;15:512-518.
[27] Carson RE, Huang SC, Green ME. "Weighted integration method for local cerebral blood flow measurements with positron emission tomography". *J Cereb Blood Flow Metab*. 1986;6:245-258.
[28] Gunn RN, Lammertsma AA, Hume SP et al. "Parametric Imaging of ligand-receptor binding in PET using a simplified reference region model. *Neuroimage*. 1997;6:279-287.
[29] Muzi M, O'Sullivan F, Mankoff D, et al. "QIN: Quantitative Assessment of Dynamic PET Imaging Data in Cancer Imaging". *Magn Reson Imaging*. 2012; 30(9): 1203-1215.
[30] Patlak CS, Blasberg RG, Fenstermacher JD. "Graphical Evaluation of Blood-to-Brain Transfer Constants from Multiple-Time Uptake Data". *J Cereb Blood Flow Metab*. 1983;3:1-7.
[31] Logan J, Fowler JS, Volkom ND et al. "Graphical Analysis of Reversible Radioligand Binding from Time-Activity Measurements Applied to [N-^{11}C-methyl]-(--)-Cocaine PET Studies in Human Subjects". *J Cereb Blood Flow Metab*. 1990;10:740-747.
[32] By Vesa Oikonen [TPC - Multiple Time Graphical Analysis (MTGA) (http://www.turkupetcentre.net/petanalysis/model_mtga.html) or CC BY-SA 3.0 (http://creativecommons.org/licenses/by-sa/3.0)], via Wikimedia Commons.
[33] Van den Hoff, J. "Linearisations". In: *PET Pharmacokinetic course manual* (Maguire RE, Leenders KL, eds). Kobe, Japan 2007; pp. 43-52.
[34] Ostergaard L. "Principles of cerebral perfusion imaging by bolus tracking. *J Magn Reson Imaging*. 2005;22:710-717.
[35] Hawe D, Hérnandez F, O'Suilleabháin L, et al. "Kinetic Analysis of Dynamic Positron Emission Tomography Data using Open-Source Image Processing and Statistical Inference Tools". *Wiley Interdisciplinary Reviews: Computational Statistics*. 2012.
[36] By Vesa Oikonen [TPC - Reference input compartmental models (http://www.turkupetcentre.net/ /petanalysis/model_compartmental_ref.html) or CC BY-SA 3.0 (http://creativecommons.org/licenses/by-sa/3.0)], via Wikimedia Commons.
[37] Carson R. "Tracer Kinetic Parametric Imaging in PET". *Biomedical Imaging: Nano to Macro*, 2004. IEEE International Symposium on Biomedical Imaging.
[38] Tsoumpas C, Turkheimer F, Thielimans K. "A survey of approaches for direct parametric image reconstruction in emission tomography". Med Phys. 2008; 35:3963-3971.
[39] Louis D N, Perry A, Reifenberger G, et al. "The 2016 World Health Organization Classification of Tumours of the Central Nervous System: a summary". *Acta Neuropathol*. 2016; 131:803-820.
[40] DeAngelis L. "Brain Tumours". *The New England Journal of Medicine*. 2001; 344:114-123.
[41] Fougère C, Suchorska B, Bartensteain P, et al. "Molecular imaging of gliomas with PET: Opportunities and limitations". Neuro-Oncology. 2011; 13 (8): 806-820.
[42] De Witte O, Levivier M, Violon P, et al. "Prognostic value of positron emission tomography with [^{18}F]fluoro-2-D-glucose in the low-grade glioma". *J Neuro-surg*. 1996;39:470–477.
[43] Pauleit D, Stoffels G, Bachofner A, et al. "Comparision of ^{18}F-FET and ^{18}F-FDG PET in brain tumours". *Nucl Med Bio*. 2009;36:779-787.
[44] Lau E, Drummond KJ, Ware RE, et al. "Comparative PET study using ^{18}F-FET and ^{18}F-FDG for the avaluation of patients with suspected brain tumour". *J Clinic Neuroscience*. 2010;17:43-49.
[45] Pauleit D, Zimmermann A, Stoffels G, et al. "18F-FET PET Compared with ^{18}F-FDG PET and CT in Patients with Head and Neck Cancer". *J Nucl Med*. 2006; 47:256-261.
[46] Rachinger W, Goetz C, Pöpperl G, et al. "Positron emission tomography with *O*-(2-[^{18}F]fluorethyl)-L-tyrosine versus magnetic resonance imaging in the diagnosis of recurrent gliomas". *Neurosurgery*. 2005;57:505-511.
[47] Floeth FW, Pauleit D, Sabel M, et al. "Prognostic value of *O*-(2-[^{18}F]fluorethyl)-L-tyrosine PET and MRI in Low-Grade Glioma" *J Nucl Med*. 2007;48:519-527.

[48] Pauleit D, Floeth F, Hamacher K, et al. "*O*-(2-[^{18}F]fluorethyl)-L-tyrosine PET combined with MRI improves the diagnostic assessment of cerebral gliomas". *Brain*. 2005;128:678-687.
[49] Brandsma D, van der Bent MJ. "Pseudoprogression and pseudoresponse in the treatment of gliomas". *Curr Opin Neurol*. 2009;22:633-638.
[50] Hegi ME, Diserens AC, Gorlia T, et al. " MGMT gene silencing and benefit from temozolamide in glioblastoma". *N Engl J Med*. 2005; 352:997-1003.
[51] Galldiks N, Dunkl V, Stoffels G, et al. "Diagnosis of pseudoprogression in patients with glioblastoma using O-(2-[^{18}F]fluorethyl)-L-tyrosine PET". *Eur J Nucl Med Mol Imaging*. 2015;42:685-695.
[52] Weckesser M, Langen KJ, Rickert CH, et al. "*O*-(2-[^{18}F]fluorethyl)-L-tyrosine PET in the clinical evaluation of primary brain tumours". *Eur J Nucl Med Mol Imaging*. 2005;32:422-429.
[53] Pöpperl G, Gotz C, Rachinger W, et al. "Value of *O*-(2-[^{18}F]fluorethyl)-L-tyrosine PET for the diagnosis of recurrent glioma". *Eur J Nucl Med Mol Imaging*. 2004;31:1464-1470.
[54] Pöpperl G, Kreth F, Mehrkens J, et al. "FET PET for the evaluation of untreated gliomas: correlation of FET uptake and uptake kinetics with tumour grading". *Eur J Nuc Med Mol Imaging*. 2007; 34:1933-1942.
[55] Thiele F, Ehmer J, Piroth MD, et al. "The quantification of dynamic FET PET imaging and correlation with the clinical outcome in patients with glioblastoma". *Phys Med Biol*. 2009;5525-5539.
[56] Galldikis N, Stoffels G, Filss C, et al. "Role of *O*-(2-[^{18}F]fluoroethyl)-L-tyrosine PET for differentiation of Local Recurrent Brain Metastasis from Radiation Necrosis". *J Nucl Med*. 2012;53:1367-1374.
[57] Dooms GC, Hecht S, Brandt-Zawadski M, et al. "Brain radiation lesions: MR imaging". *Radiology*. 1986;158:149-155.
[58] Ferlay J, Soerjomataram I, Ervik M, et al. "GLOBOCAN 2012 v1.0, Cancer Incidence and Mortality Worldwide: IARC CancerBase No. 11" [Internet]. Lyon, France: International Agency for Research on Cancer; 2013. Available from: http://globocan.iarc.fr, accessed on 8/11/2016.
[59] Moulin-Romsée G, D'Hondt E, de Groot T, et al. "Non-invasive grading of brain tumours using dynamic amino acid PET imaging: does it work for ^{11}C-methionine?". *Eur J Nucl Med Mol Imaging*. 2007;34(12):2082-2087.
[60] Herzog H, Meyer P, Stoffels G, et al. "Simplified analysis of FET-kinetics in brain tumours by voxel-by-voxel linear regression". *J Nucl Med*. 2008; 49, supplement 1: 78.
[61] Kolb A, Werhl H, Hofmann M, et al. "Technical performance evaluation of a human brain PET/MRI system". *Eur Radiol*. 2012; 22: 1776-1788.
[62] Rota Kops E, Herzog H. "Template based attenuation correction for PET in MR-PET scanners" *in* Nuclear Science Symposium Conference Record, 2008.
[63] Wolfram Research, Inc., Mathematica, Version 7.0, Champaign, IL (2008).
[64] Wolfram Research, Inc., Mathematica, Version 10.2, Champaign, IL (2015).
[65] Freedman D. "Statistical Models: Theory and Practice". *Cambrigde University Press*. 2009. p 26.
[66] Smyth G. "Nonlinear regression". In: *Encyclopedia of Environmetrics* (El-Shaarawi AH, Piegorsch WW, eds). Chichester, United Kingdom 2002; p. 2.

Appendix I - Mathematica Package for Reading ECAT7 files

In this appendix, the source code used to write the Mathematica package that allowed for image data import is shown. In this work, two Mathematica versions were used: 7 and 10. The present package was written with version 7, and it works in newer Mathematica versions. The data used in this work was in ECAT7 data format. This format is native to several generations of PET scanners manufactured by Siemens. The ECAT7 format can contain PET raw data, dynamic and parametric images, and polar maps.

```
(*::Package::*)
(*--------------------Mathematica Package for Reading ECAT7 files-----------------*)
(*                              Author: Ines Costa                                 *)
(*                            Last edited: 07-04-2016                              *)
(*-------------------------------------------------------------------------------*)
BeginPackage["ReadECAT7`"]

Options[loadImg]={Silent->True};
loadMainHeader::usage="loadMainHeader[file,format] reads the main header";
loadImg::usage="loadImg[file,opts] prints the main header, directory information,
subheaders, and loads image data";

Begin["Private`"]
(*---------------------------------IMPLEMENTATION--------------------------------*)
(*-------------------------------------------------------------------------------*)
(*FORMATS & LABELS*)
(*-------------------------------------------------------------------------------*)
(*Main header*)
mainHeaderFormat={
Table["Character8",{14}],(* unsigned char magic_number[14] *)
Table["Character8",{32}], (* original_file _name[32] *)
Table["Integer16",{3}], (* sw_version,system_type,file_type*)
Table["Character8",{10}], (* serial_number[10] *)
Table["Integer32",{1}], (* scan_start _time *)
Table["Character8",{8}], (* isotope_name[8] *)
Table["Real32",{1}],(* isotope_halflife *)
Table["Character8",{32}], (* radiopharmaceutical[32] *)
Table["Real32",{4}], (*gantry_tilt,gantry_rotation,bed_elevation,gintrinsic_tilt*)
Table["Integer16",{2}], (*wobble_speed,transm_source _type*)
Table["Real32",{2}],(* distance_scanned,transaxial_fov*)
Table["Integer16",{3}], (*angular_compression,coin_samp _mode,axial_samp _mode*)
Table["Real32",{1}],(* ecat_calibration _factor *)
Table["Integer16",{3}],                    (*calibration_units,calibration_units
_label,compression_code*)
Table["Character8",{12}], (* study_type[12] *)
Table["Character8",{16}], (* patient_id[16] *)
Table["Character8",{32}], (* patient_name[32] *)
Table["Character8",{1}], (* patient_sex *)
Table["Character8",{1}], (* patient_dexterity *)
Table["Real32",{3}], (*patient_age,patient_height,patient_weight*)
Table["Integer32",{1}], (* patient_birth _date *)
Table["Character8",{32}], (* physician_name[32] *)
Table["Character8",{32}],(* operator_name[32] *)
Table["Character8",{32}],(* study_description[32] *)
Table["Integer16",{2}],(*acquisition_type,patient_orientation*)
Table["Character8",{20}],(* facility_name[20] *)
Table["Integer16",{4}],(*num.com/_planes,num_frames,num_gates,num_bed _pos*)
Table["Real32",{1}],(* init_bed _position *)
```

```
Table["Real32",{15}],(* bed_position[15] *)
Table["Real32",{1}],(* plane_separation *)
Table["Integer16",{3}],(* lwr_sctr _thres,lwr_true _thres,upr_true _thres*)
Table["Character8",{10}],(* user_process _code[10] *)
Table["Integer16",{1}],(* acquisition_mode *)
Table["Real32",{2}],(*bin_size,branching_fraction *)
Table["Integer32",{1}],(* dose_start _time *)
Table["Real32",{2}],(* dosage,well_counter _corr _factor *)
Table["Character8",{32}],(* data_units[32] *)
Table["Integer16",{1}],(* septa_state *)
Table["Integer16",{6}](* fill_cti[6] *)
};

(*Main header labels*)
mainHeaderLabels={
"Magic number:",
"Original file name:",
{"Software version, system type, file type:"},
"Serial number:",
"Scan start time:",
"Isotope name:",
"Isotope halflife:",
"Radiopharmaceutical:",
{"Gantry tilt, gantry rotation, bed elevation, intrinsic tilt:"},
{"Wobble speed, transmission source type:"},
{"Distance scanned, transaxial FOV:"},
{"Angular compression, coincidence sample mode, axial sample mode:"},
"Calibration factor:",
{"Calibration units, calibration units label, compression code:"},
"Study type:",
"Patient ID:",
"\tName:",
"\tSex:",
"\tDexterity:",
{"\tAge, height, weight:"},
"\tBirth date:",
"Physician name:",
"Operator name:",
"Study description:",
{"Acquisition type, patient orientation:"},
"Facility name:",
{"Number of planes, number of frames, number of gates, number of bed positions:"},
"Initial bed position:",
"Bed offsets:",
"Plane Separation:",
{"Lower scatter threshold, lower trues threshold, upper trues threshold:"},
"User process code:",
"Acquisition mode:",
{"Bin size, branching fraction:"},
"Dose start time:",
{"Dosage, well counter factor:"},
"Data units:",
"Septa state:",
"Fill cti:"
};

(*Sub header*)
subHeaderFormat={
Table["Integer16",{1}],(* data_type*)
```

```
Table["Integer16",{4}], (*num_dimensions,x_dimension,y_dimension,z_dimensio *)
Table["Real32",{5}],(* x_offset,y_offset,z_offset,recon_zoom,scale_factor *)
Table["Integer16",{2}], (* image_min,image_max *)
Table["Real32",{3}],(* x_pixel _size,y_pixel _size,z_pixel _size *)
Table["Integer32",{2}], (* frame_duration,frame_start _time *)
Table["Integer16",{1}], (* filter_code *)
Table["Real32",{7}],(*                  x_resolution,y_resolution,z_resolution,num_r
_elements,num_angles,z_rotation _angle,decay_corr _fctr *)
Table["Integer16",{4}], (*processing_code,gate_duration,r_wave _offset,num_accepted
_beats*)
Table["Real32",{3}],     (*filter_cutoff     _frequency,filter_resolution,filter_ramp
_slope*)
Table["Integer16",{1}],(*filter_order*)
Table["Real32",{2}], (*filter_scatter _fraction,filter_scatter _slope*)
Table["Character8",{1}], (*annotation*)
Table["Real32",{11}],(*mt_ 1_ 1,mt_ 1_ 2,mt_ 1_ 3,mt_ 2_ 1,mt_ 2_ 2,mt_ 2_ 3,mt_ 3_
1,mt_ 3_ 2,mt_ 3_ 3,rfilter_cutoff,rfilter_resolution*)
Table["Integer16",{2}],(*rfilrer_code,rfilter_order*)
Table["Real32",{3}],(*mt_ 1_ 4,mt_ 2_ 4,mt_ 3_ 4*)
Table["Integer16",{5}](*scatter_type,recon_type,recon_views,fill_cti,fill_user*)
};

(*Sub header labels*)
subHeaderLabels={
"Data type:",
{"Number of dimensions, x-dimension, y-dimension, z-dimension:"},
{"x-offset, y-offset, z-offset, recon_zoom, scale_factor:"},
{"image_min, image_max"},
{"x_pixel_size, y_pixel_size, z_pixel_size:"},
{"frame_duration, frame_start_time:"},
"filter_code",
{"x_resolution,    y_resolution,    z_resolution,    num_r_elements,    num_angles,
z_rotation_angle, decay_corr_fctr:"},
{"processing_code, gate_duration, r_wave_offset, num_accepted_beats:"},
{"filter_cutoff_frequency, filter_resolution, filter_ramp_slope:"},
"filter_order:",
{"filter_scatter_fraction, filter_scatter_slope:"},
"annotation:",
{"mt_1_1,  mt_1_2,  mt_1_3,  mt_2_1,  mt_2_2,  mt_2_3,  mt_3_1,  mt_3_2,  mt_3_3,
rfilter_cutoff, rfilter_resolution"},
{"rfilrer_code, rfilter_order"},
{"mt_1_4, mt_2_4, mt_3_4"},
{"scatter_type, recon_type, recon_views, fill_cti, fill_user"}
};
(*-------------------------------------------------------------------------------*)
(*FUNCTIONS*)
(*-------------------------------------------------------------------------------*)
procHeaderEntry[entry_,format_]:=Block[{res,len=Length@entry},      (*joins      the
information coded as Character*)
If[len>1,
If[format[[1]]=="Character8",res=StringJoin@entry,res=entry],
res=entry];
res
]
(*-------------------------------------------------------------------------------*)
(*Function that reads the main header information*)
loadMainHeader[filename_]:=Block[{header,rawheader=BinaryRead[filename,#,
ByteOrdering->-$ByteOrdering]&/@mainHeaderFormat},
Close[filename];
```

```
header=MapThread[procHeaderEntry,{rawheader,mainHeaderFormat}];
header
]
(*------------------------------------------------------------------------------*)
(*helper function for subheader reading and image loading*)
Options[helperfunc]={Silent->True};
helperfunc[streampos_,filename_,OptionsPattern[]]:=Block[{rawsubheader,datatype,ida
ta,sdata,pdata,imagedimensions,frametimes,filedescriptor,subheader},
filedescriptor=OpenRead[filename,BinaryFormat->True];
SetStreamPosition[filedescriptor,streampos];
rawsubheader=BinaryRead[filedescriptor,#,                    ByteOrdering->-
$ByteOrdering]&/@subHeaderFormat;
subheader=MapThread[procHeaderEntry,{rawsubheader,subHeaderFormat}];
frametimes=subheader[[6]];
imagedimensions=subheader[[2,2;;4]];
If[OptionValue[Silent]!=True,
Print[Transpose@{subHeaderLabels[[1;;6]],subheader[[1;;6]]}//TableForm];
Print["------------------------------------------------------------------------
-------------------------------------------------------"];
];
Which[subheader[[1,1]]==5,datatype="Real32",subheader[[1,1]]==6,datatype="Integer16
"];
SetStreamPosition[filedescriptor,streampos+512];
idata=BinaryReadList[filedescriptor,datatype,Times@@imagedimensions, ByteOrdering->-
$ByteOrdering];
sdata=idata*subheader[[3,5]];
pdata=Partition[Partition[sdata,subheader[[2,2]]],subheader[[2,3]]];(*Partitioned
data*)
Close[filedescriptor];
Return[{frametimes,imagedimensions,pdata}];
]
(*------------------------------------------------------------------------------*)
(*Function to read the subheaders and load the data*)
loadImg[filename_,OptionsPattern[]]:=
Block[{nFrames,rawdata,records,data,pdata,rawheader,mainheader,times,positions},
rawheader=BinaryRead[filename,#, ByteOrdering->-$ByteOrdering]&/@mainHeaderFormat;
mainheader=MapThread[procHeaderEntry,{rawheader,mainHeaderFormat}];
If[OptionValue[Silent]!=True,
Print["------------------------------------------------------------------------
-------------------------------------------------------"];
Print["MAIN HEADER"];
Print["------------------------------------------------------------------------
-------------------------------------------------------"];
Print[Transpose@{mainHeaderLabels,mainheader}//TableForm];
];
(*Directory reading:*)
nFrames=BinaryRead[filename,{"Integer32","Integer32","Integer32","Integer32"},
ByteOrdering->-$ByteOrdering];
rawdata=BinaryRead[filename,Table[Table["Integer32",{4}],{31}],      ByteOrdering->-
$ByteOrdering];
records=rawdata[[1;;nFrames[[4]],{2,3}]]-1; (*selecting the list of first and last
records*)
If[OptionValue[Silent]!=True,
Print["------------------------------------------------------------------------
-------------------------------------------------------"];
Print["DIRECTORY"];
Print["------------------------------------------------------------------------
-------------------------------------------------------"];
Print["Number of Matrices:",nFrames[[4]]];
```

```
Print["------------------------------------------------------------------------------
-------------------------------------------------------"];
Print["First // Last records"];
Print[TableForm[records]//OutputForm];
Print["------------------------------------------------------------------------------
-------------------------------------------------------"];
Print["SUBHEADERS"];
Print["------------------------------------------------------------------------------
-------------------------------------------------------"];
];
positions=Table[records[[i,1]]*512,{i,nFrames[[4]]}];
If[OptionValue[Silent]==True,
data=helperfunc[#,filename,Silent->True]&/@positions;,
data=helperfunc[#,filename,Silent->False]&/@positions;
];
If[OptionValue[Silent]!=True,
Print["Image loaded."];
];
Close[filename];
Return[{data[[All,{1,2}]],data[[All,3]]}];
]
End[] (* End of Private content*)
EndPackage[]
```

The image volume is loaded to Mathematica by calling the `loadImg` function. Selecting `True` as an option in `Silent` will not print out the header and subheaders information. Both image data and time frame information, namely frame duration and frame start time, are loaded altogether. Time data is in milliseconds. The following code is an example of how the images are loaded into Mathematica for computation:

```
ecat7LG131=loadImg["filename.v",Silent->True];
timeLG131=(ecat7LG131[[1,All,1,2]]+ecat7LG131[[1,All,1,1]]/2)/1000;
imageLG131=ecat7LG131[[2]];
```

Appendix II - Source code for segmentation and STV fitting

The program used in the tumour segmentation procedure and the functions for STV fitting are presented below. To create the mask, the sum of the image along time frames must be calculated. Then, to facilitate computation, a cubic image volume containing the tumour is manually selected. The mask is extracted from this selected volume. Here, the procedure for one dataset is shown. It is important to note that this program was written with Mathematica 10, and some functions that are not available in older Mathematica versions were used.

```
fr=Array[#&,16];

timageLG131=Total[#,{1}]/Length[#]&@imageLG131; (*sum image*)

maxszone=Max@Flatten@timageLG131[[52;;84,95;;140,123;;160]];
mask=Binarize[Image3D[timageLG131[[52;;84,95;;140,123;;160]]],4.8];
mcomp=MorphologicalComponents/@mask;

(*temporary mask*)
tmask=ImageData[Sign/@mcomp];
(*final mask*)
tmask131=ImageData@Image3D[GeodesicOpening[tmask,5]];

(*average uptake in tumour area*)
meanLG131=Mean[DeleteCases[Flatten[imageLG131[[#,52;;84,95;;140,123;;160]]*tmask131
],N[0]]]&/@fr
```

The function below performs the nonlinear regression fit using the exponentially damped linear model with square-root time dependence. The first 2 minutes of acquisition, which correspond to the first 2 time frames, are discarded. The gradient descent optimization algorithm included in Mathematica `NonlinearModelFit` function is used to estimate the parameters.

```
fitsqdropup[data_,tf_]:=
   Block[{result,ag=N@Mean@data,fd=Drop[{tf,data}^T,2],model},
       model=NonlinearModelFit[fd,A Sqrt[t] Exp[-K Sqrt[t]],{{A,ag},{K,0.0006}},t,
              VarianceEstimatorFunction->Automatic,Method->"Gradient"];

       result={{A, K}/.model["BestFitParameters"],model["ParameterErrors"],
              model["RSquared"]};

   Print@Show[ListPlot[fd,PlotRange->{{0,3200},{0,12}},
       PlotLabel->{{"A","K"}/.model["BestFitParameters"]},PlotMarkers->{?},
       PlotRange->Automatic,AxesLabel->{"Time (s)","Uptake (kBq/cc)"},
       Frame->True,FrameLabel->{"Time (s)","Uptake (kBq/cc)"},
       GridLines->Automatic,LabelStyle->Directive[14]],
       Plot[model["BestFit"],{t,tf[[3]],tf[[-1]]},PlotPoints->500,PlotRange->All,
       PlotStyle->{Thick,Red},Frame->True,ImageSize->400]];
result]

(*comand to perform the fit:*)
fit131=fitsqdropup[meanLG131,timeLG131];
```

The function below performs the linear regression fit. The first 5 minutes of acquisition, which correspond to the first 5 time frames, are discarded.

```
fitlineardrop[data_,tf_]:=
   Block[{result,ag=N@Mean@data,fd=Drop[{tf,data}^T],5],model},
      model=LinearModelFit[fd,x,x,VarianceEstimatorFunction->Automatic];

      result={model["BestFitParameters"],model["ParameterErrors"],
             model["RSquared"]};

      Print@Show[ListPlot[fd,PlotRange->{{0,3200},{0,12}},
         PlotLabel->{model["BestFitParameters"]},PlotMarkers->{?},
         PlotRange->Automatic,Frame->True,
         FrameLabel->{"Time (s)","Uptake (kBq/cc)"},GridLines->Automatic,
         LabelStyle->Directive[14]],
         Plot[model["BestFit"],{x,tf[[6]],tf[[-1]]},PlotStyle->{Thick,Red},
         ImageSize->800]];
result]

fit131lin=fitlineardrop[meanLG131,timeLG131]
```

Appendix III - Source code for calculating parametric images

The functions used to calculate the parametric images are presented below. The first, `fitdropimg`, is used to calculate the parametric images of the small, manually selected volumes containing the tumour. The model featured in the function below is the simple exponentially damped linear model. The functions that apply the fitting with the other models are identical to this one, with just the model expression changing. The same applies to how the function is called, and how it runs over all the voxels in the selected volume: the procedure is identical for all de nonlinear regression models, and for all the images. The only difference regarding the images is the coordinates of the volume selected for fitting. It is important to note that this program was written with Mathematica 7, and some functions that are not available in newer Mathematica versions were used.

```
fitdropimg[data_,tf_]:=
  Block[{result,ag=N@Mean@data,fd=Drop[{tf,data}^T,2],model},
   model=NonlinearModelFit[fd,Abs[A] t k Exp[-k t],{{A,ag},{k,0.0006}},
    t,VarianceEstimatorFunction->Automatic];
   result={{A,k}/.model["BestFitParameters"],model["ParameterErrors"],
    model["RSquared"]};
result]

fitLG131img=Map[fitdropimg[#,timeLG131]&,
  Transpose[imageLG131[[All,52;;84,95;;140,123;;160]],{4,1,2,3}],{3}];
```

The procedure for calculating whole-head parametric images is more complex. First, it requires extracting the head from the dynamic PET data. The function below allows for head segmentation, thus excluding the background from the analysis.

```
segmentHead2D[image_,t_: 0.02,c_: 10]:=
   Block[{ss=Total[image,{1}],dims=Dimensions@image,tss,ms,mask,mc,
      segmentation,includes,fmc},tss=Total[ss,{1}];
    ms=Max@Flatten@tss;
    mask=Binarize[ImageAdjust@Image[tss/ms],0.02];
    mc=MorphologicalComponents[mask,CornerNeighbors->True];
    segmentation=
      Take[Select[Sort[Tally@Flatten@mc,#1[[2]]>#2[[2]]&],#[[1]]!=0&],1][[1,1]];
    includes=Position[mc,_?(#==segmentation&)];
    fmc=Normal@SparseArray[includes->1,Dimensions@mc,0];
    Table[fmc,{dims[[2]]}]
];
```

As performing a nonlinear regression model fit on each voxel of the whole head is a very demanding task, an auxiliary function was created to distribute the different image slices between Mathematica kernels. The goal of this strategy was to decrease computation times.

```
splitTask[img_]:=Block[{nslices=Take[Dimensions@img,1][[1]],result},
   If[EvenQ@nslices,result=Table[{i,i+1},{i,1,nslices,2}],
    result=Prepend[Table[{i,i+1},{i,4,nslices,2}],{1,3}]];
result];
```

The two functions below apply the fit to the head volume:

```
FETKineticNonlinearSingleFit[tac_,mask_,tf_,df_: 5,m_: "Gradient"]:=
   Block[{aguess,fitdata,kguess,nlm,result=Table[-1,{5}]},
```

```
    If[mask==1,aguess=Mean@Drop[tac,df];
       fitdata=Drop[Transpose@{tf,tac},df];
       kguess=ProductLog[Mean@Take[tac,-3]/aguess]/tf[[-1]];
       kguess=0.0001;
       nlm=NonlinearModelFit[fitdata,A Sqrt[t] Exp[-k Sqrt[t]],{{A,aguess},
        {k,kguess}},t,VarianceEstimatorFunction->Automatic,Method->m];
       result=
        Chop@Flatten@{{A,k}/.nlm["BestFitParameters"],nlm["ParameterErrors"],
          nlm["AdjustedRSquared"]};
];
result]

FETKineticNonlinearFit[image_,mask_,tf_,df_: 5,m_: "Gradient"]:=
   Block[{timage=Transpose[image,{4,1,2,3}]},Print@"computing";
    MapThread[FETKineticNonlinearSingleFit[#1,#2,tf,df,m]&,{timage,mask},3]]
```

To further decrease computation times, only a set of z slices was fitted. This required creating a new variable (ex: `subimg131`) containing just the "slices of interest". As with the previous volume selection, the location of these areas changed from image to image according to the location of the tumour in the brain.

```
subimg131=ecat7131[[2,All,Range[52,84,1]]];
mask131=segmentHead2D[subimg131,0.02,10];
ArrayPlot/@Take[mask131,1];
splittasks131=splitTask@mask131;
```

The voxel-wise fit was distributed between 10 kernels. After the procedure, fitting information was saved and exported.

```
LaunchKernels[10]
DistributeDefinitions[FETKineticNonlinearSingleFit,FETKineticNonlinearFit,
 splittasks020,subimg020,mask020,time020]
AbsoluteTiming[
 pimage020=
   Parallelize@
    Table[FETKineticNonlinearFit[
       subimg020[[All,splittasks020[[i,1]];;splittasks020[[i,2]]]],
       mask020[[splittasks020[[i,1]];;splittasks020[[i,2]]]],time020,2,"Gradient"],
    {i,Length@splittasks020}];]
CloseKernels[]

fitimage131=Flatten[pimage131,1];
```